AERODYNAMIC MODELLING AND FURTHER OPTIMISATION OF A SOLAR POWERED VEHICLE

by

Christopher Jon Lawrence

Submitted in fulfilment of the academic requirements for Master of Science in Mechanical Engineering, College of Agriculture, Engineering and Science,
University of KwaZulu-Natal
Durban
South Africa

Supervisor: Dr Clinton Bemont
Co-Supervisor: Miss Kirsty Veale

January 2016

PREFACE

The research contained in this thesis was completed by the candidate while based in the Discipline of Mechanical Engineering of the College of Agriculture, Engineering and Science, University of KwaZulu-Natal, Howard College, South Africa. The research was financially supported by the National Research Foundation (NRF) and Renewable and Sustainable Energy Scholarship Program (RSES).

The contents of this work have not been submitted in any form to another university and, except where the work of others is acknowledged in the text, the results reported are due to investigations by the candidate.

_____

Signed: Dr. Clinton Bemont

Date: 14 November 2016

_____

Signed: Miss Kirsty Veale

Date: 14 November 2016

DECLARATION 1: PLAGIARISM

I, Christopher Lawrence, declare that

(i) the research reported in this thesis, except where otherwise indicated, is my original research.

(ii) this thesis has not been submitted for any degree or examination at any other university.

(iii) this thesis does not contain other persons' data, pictures, graphs or other information, unless specifically acknowledged as being sourced from other persons.

(iv) this thesis does not contain other persons' writing, unless specifically acknowledged as being sourced from other researchers. Where other written sources have been quoted, then:

a. their words have been re-written but the general information attributed to them has been referenced

b. where their exact words have been used, then their writing has been placed in italics and inside quotation marks, and referenced.

(v) this thesis does not contain text, graphics or tables copied and pasted from the Internet, unless specifically acknowledged, and the source being detailed in the thesis and in the References sections.

Signed _____ Date _____

Mr Christopher Jon Lawrence

DECLARATION 2: PUBLICATIONS

Lawrence, C. J., Bemont, C. P., Veale, K. L. Optimisation via "De-turbulating" Spoked Wheels of a Solar Car. *13th International Energy Conversion Engineering Conference, AIAA. Hilton Hotel, Orlando, Florida,* United States of America, 27-30th July 2015.

Signed _____ Date _____

Mr. Christopher Lawrence

ACKNOWLEDGEMENTS

I would like to express my thanks and appreciation to my supervisor, Dr Clinton Bemont and my co-supervisor, Miss Kirsty Veale for their outstanding supervision, motivation and support during my Master's degree studies.

I would like to express my appreciation towards my fellow solar car team members for the constant support and understanding throughout the project itself as well as in the race participations.

I would like to thank Jason Wepener for his guidance and support through my MSc studies.

Finally, to my family and friends, especially my mother, Christina Lynne Lawrence, for their gracious support, guidance, and patience throughout my undergraduate and MSc studies.

ABSTRACT

Computational fluid dynamics was used to optimise the aerodynamics of a solar powered vehicle via the addition of airflow alteration devices that interact with the boundary layer airflow. These features were designed, manufactured and applied to the vehicle while ensuring that the bulk geometry remained unmodified. The modifications had to be added to the vehicle non-invasively, and had to allow for removal during race conditions. The solar vehicle raced in both the Sasol Solar Challenge (SASC) which took place in September 2014 and the Bridgestone World Solar Challenge (WSC) which took place in September 2015. Aerodynamic drag is the single largest energy loss experienced by a solar vehicle; it is therefore essential that the aerodynamics of these vehicles be highly refined if they are to be competitive. The UKZN solar vehicle placed first in South Africa in the SASC and 13th in the WSC - indisputably outstanding results.

The features to be refined were chosen to reduce aerodynamic drag caused by the wheel spokes as well as the canopy due to these being high turbulence zones and having high curvatures respectively. The principles applied were to reduce turbulence caused by the wheel spokes by adding to the wheel geometry, and adding turbulence to the canopy airflow through the use of a technique commonly known as flow tripping. While turbulence caused by the wheels is undesirable, the turbulence added by flow tripping is desirable as it reduces the size of the separated region of airflow behind the canopy, allowing for a net reduction in aerodynamic drag.

Wheel geometry alteration was done via the addition of smooth and dimpled covers, so as to mitigate the turbulence caused by the wheel spokes. Many techniques were considered to trip the airflow on the canopy, it was found that vortex generators of specific geometry and dimensions would reduce drag more effectively. Another airflow altering device, a NACA duct, was designed and manufactured. This duct was placed on the canopy to allow airflow into the driver compartment which enabled adherence to race rules and allowed for driver cooling and ventilation. Each wheel cover was manufactured from two layers of carbon fibre to allow a net gain in efficiency with regards to rolling resistance and drag reduction when considering weight added by the wheel covers. The vortex generators and NACA duct were 3-D printed using ABS plastic. The wheel covers and NACA duct were applied to the car for the World Solar Challenge while only the wheel covers were applied for the Sasol Solar Challenge. The vortex generators were not applied due to the efficiency gain from the application being uncertain at the time of the race. A gain in aerodynamic efficiency with the addition of wheel covers to a front wheel was shown through CFD testing. The drag was reduced by approximately 0.5 Newtons (5 %) relating to translational forces and 0.02 Newtons per meter (44 %) percent with regards to rotational forces. The addition of vortex generators resulted in a drag reduction ranging from approximately zero to three percent when considering straight airflow and crosswinds respectively.

Table of Contents

LIST OF FIGURES

Chapter One

Chapter Two

Chapter Three

Chapter Four

LIST OF TABLES

NOMENCLATURE

Symbols

A:	Area (Surface area or cross-sectional area for fluid flow) [m^2]
A_f:	Frontal area [m^2]
a:	First layer thickness/near wall thickness [mm]
b:	Spacing between dimples [m]
C_f:	Skin friction coefficient [-]
c:	Dimple diameter [m]
$c_{rolling}$:	Rolling resistance coefficient [-]
d:	Ball diameter [m]
e:	Length of vortex generator [m]
F:	Force [N]
$F_{rolling}$:	Rolling resistance [N]
F_p:	Force from pressure difference [N]
F_v:	Viscous force/viscous drag [N]
h:	Height of vortex generator or inlet of NACA duct [m]
k:	Dimple depth [m]
N:	Rotational speed, [rpm]
n:	Layer number, layer one is taken as the near wall layer [-]
P:	Pressure [$Pascals, PA$]
R:	Radius of wheel [m]
r:	Stretching factor [-]
U:	Velocity [m/s]

u: Total Prism layer thickness [mm]

u^*: Dimensionless velocity [-]

v: Fluid velocity [m/s]

W_{car}: Weight of car [N]

w: NACA duct inlet width [m]

x: Length from leading edge (Chord length if aerofoil) [m]

y: First prism layer mid cell height [m]

y^+: Wall coordinate [-]

z: Distance between vortex generators [m]

β: Angle of vortex generators [degrees]

δ: Boundary layer thickness at length "x" [m]

υ: Kinematic viscosity [N-s]

ρ: Density [kg/m^3]

τ_w: Wall shear stress [N]

ω: Angular velocity of wheel to be assigned [rad/s]

Abbreviations

CFD: Computational fluid dynamics

DERA: Defence Evaluation and Research Agency

LE: Leading Edge

FCSD: Flexible composite surface deturbulator

Kph: Kilometres per hour

RANS: Reynolds Averaged Navier Stokes

Re: Reynolds number

SASC: Sasol Solar Challenge

Sta.:	Station Point/Reference Point
TKE:	Turbulent Kinetic Energy
TVR:	Turbulent Viscosity Ratio
VG:	Vortex generator
WSC:	Bridgestone World Solar Challenge

CHAPTER ONE: INTRODUCTION

1.1. Hypothesis

It is proposed that the aerodynamics of a solar vehicle may be improved without modifying the bulk geometry thereof.

1.2. Overview

Solar car racing vehicles are powered only by the sun; the solar energy gathered is stored in a battery which has size limitations set out by the rules for the particular class in which the vehicle is participating, and thus imposes limits on the total energy resource that may be stored. The need to increase the efficiency at which this energy is used is paramount to having a successful solar vehicle for the current application of solar vehicle racing. Since aerodynamic drag accounts for most of the energy loss of a vehicle in highway conditions, improving aerodynamic efficiency significantly reduces energy expenditure in propelling the vehicle. Other losses include, but are not limited to, rolling resistance and mechanical and electrical inefficiencies. Reducing any of these elements results in significant improvement in distance or alternatively, the average speed for a given energy input. This will enable a solar car to travel further while using less energy; the most vital aspect in the design of a successful solar vehicle. Improvements in the aerodynamics of a solar vehicle, while specific to solar vehicle design as in this case, may be also be applied to improve the efficiency of other applications such as wind turbine blades or even aircraft wing design.

The main objective of designing an aerodynamic vehicle is to reduce, as far as possible, skin friction and adverse pressure gradients over the vehicle. This can be achieved by simply reducing the length of the body in contact with air and reducing the frontal area, respectively, by giving the body a more streamlined shape. The spatial constraints placed on any design by the need for certain internal components limited the amount by which the shell size, made up of the frontal and wetted area, could be reduced. This means that when shortening the length of the aerofoil surface, in order to fit spatial constraints, the aerofoil becomes less streamlined and hence more susceptible to turbulence which raises skin friction while also resulting in adverse pressure gradients increasing the chance of separation. An effective way to achieve optimisation in solar vehicle aerodynamics is to apply computational fluid dynamic modelling to analyse and iteratively optimise aerodynamic features such as cowlings, trip wires, surface relief and/or minor geometric modifications.

Some well-known applications of surface relief optimisation are mentioned here as an introduction to the work reviewed, and several more are listed in Section 2.3.

Many applications of turbulators are used in nature, such as the ribs on the leading and trailing edges of whale fins (Blain, 2008) and the roughened skin of sharks (Bennett, 2013). Many great inventions have stemmed from inspiration by nature, and the research in this field is highly applicable to aerodynamic modelling principles.

Louis Garneau, an extremely successful cyclist as well as aerodynamic helmet designer, applied computational fluid dynamic (CFD) analysis to design dimples and vortex generators to "create turbulent airflow across the back half of the helmet, forcing the boundary layer to remain attached for longer and thereby minimising drag" (Dutil & Sgro, 2014). After the Vorttice helmet was designed, a new helmet, the P-09, with improved aerodynamics had no vortex generators as such, just dimples (Garneau, 2014).

Several applications were reviewed to gain a broad understanding of ways in which to reduce aerodynamic drag by altering the boundary layer airflow over aerofoil surfaces and shapes similar to that of the solar vehicle. Similar application areas such as aeroplane wings (aerofoils) as well as dissimilar application areas such as golf balls were analysed. Speed (Mach number) of application with regards to bluff or streamlined bodies plus methods of application were investigated. Results from testing similar devices applied to the solar vehicle may be verified via wind-tunnel testing although comparison of the designs via CFD is sufficient; well-designed models are likely to approximate real aerodynamic improvements. For the purposes of the current work, the solar vehicle was split into the main bulk geometry sections shown in Figure 1-1. These sections are given the nomenclature set out here for reference.

Figure 1-1: 2014 Sasol Solar Challenge – Car discretisation.

1.3. Previous Work

The UKZN solar car project was started in 2012 by UKZN lecturers and continued through to 2015. The first car was designed and built in 2012 and competed in the 2012 Sasol Solar Challenge (SASC) in South Africa. After that, the 2013 car was designed and built for the 2014 SASC in South Africa and later modified for the 2015 World Solar Challenge in Australia. The second solar vehicle was partially designed in 2013 and the design completed in 2014. The vehicle was built early in 2014 which placed constraints on aerodynamic modifications, namely that the bulk shell geometry of the vehicle would have to remain unaltered due it being built already. Design and optimisation of the 2013/2014 bulk solar car shell aerodynamics (utilising computational fluid dynamics, (CFD)) and computer-aided design (CAD) modelling of the internal monocoque chassis was completed by the author (Lawrence, et al., 2013).

A steady state (time-independent) approach in CFD modelling was used when convergence was reached with no need for a transient (time-dependent) CFD modelling approach. Transient CFD models analyse models that incorporate acceleration where steady state models consider constant speed. Transient models tend to be more time consuming than steady state CFD models. Time and complexity constraints placed on the CFD models and design thus only allowed for steady state modelling to be conducted. The computational resources available placed constraints on the size of the models.

Incorporated CAD detail of the CFD models was thus simplified to enable comparable results in sufficient time. This was due to implementation considerations when manufacturing for the aforementioned races. Several concepts were tested and the most aerodynamically efficient chosen for further optimisation.

The author assisted in utilising finite element analysis to model the vehicle chassis. The solar vehicle design of 2013 was updated early in 2014 to meet the requirements of updated internal components that had not been finalised in 2013, for example, suspension, steering and battery pack. This made it imperative for entirely new and more accurate CFD models to be constructed for the purpose of improving boundary layer airflow over the current vehicle shell.

1.4. Aims and Objectives

The general aims are outlined first with more detailed objectives thereafter.

1.4.1. Aims

In order to allow for effective reduction of the losses due to aerodynamic drag, the following aims were to be met:

- To ensure that the CFD models would account for, as far as possible, the airflow effects over the entire assembled solar vehicle taking into account the rotation of wheels, simplified interior and detailed exterior of the vehicle (depending on the testing objectives).
- To apply analytical methods should be used in order to accurately set model boundary conditions. Note: Suspension and unnecessary interior detail were not incorporated so that computational resource use was reduced.
- To utilise CFD models to locate areas available for aerodynamic improvement on the existing solar vehicle body.
- To investigate the possibility of using trip wires, cowlings, vortex generators, and/or dimpling to optimise the vehicle aerodynamics.
- To optimise the solar car aerodynamics without modifying the bulk geometry of the car while remaining within the regulations of the race/s and within the bounds of resources available to the project.
- To apply manufactured devices to the solar vehicle for the Sasol Solar Challenge (SASC) and Bridgestone World Solar Challenge (WSC).

1.4.2. Objectives

Specifically, the following objectives were to be met in order for the solar vehicle aerodynamics to be optimised:

- The drag due to skin friction should be reduced over the wheel spoke region through the use of smooth or dimpled wheel covers.
- The drag due to adverse pressure gradient over the solar vehicle should be reduced over the solar vehicle as a whole through the use of airflow tripping devices described in the literature review.
- The overall drag due to aerodynamic effects must be reduced through optimisation of the airflow over the vehicle.

CHAPTER TWO: LITERATURE REVIEW

2.1. Aerodynamics Overview

Fundamental aerodynamic principles were first reviewed so that insight was gained in order to allow greater understanding of the airflow and alteration devices used.

2.1.1. Boundary Layer

Fluid affected by a body to which it is attached forms a layer on the body known as the boundary layer, which is defined by a velocity profile as discussed in Section 2.1.3 (Fox, et al., 2012). In a moving fluid that is moving relative to a stationary object, the molecules of that fluid that are in contact with the object's surface are moving at the same velocity as the object, which means that those molecules are stationary. The interaction of these molecules with the object surface is similar to an object moving relative to a stationary fluid. The molecules further from the object surface are decreasingly affected by interaction with the object's surface but are still affected due to the interaction of the fluid molecules which are in contact with each other. The molecules are therefore moving increasingly faster when at a greater distance from the surface of the object until the maximum free stream velocity is met. This phenomenon is illustrated and explained in Section 2.1.3. The thickness of a boundary layer when considering flow over a flat plate may be estimated by equation 2-1:

$$\delta = \frac{0.382x}{Re^{\frac{1}{5}}} \qquad \text{Equation 2-1}$$

2.1.2. Laminar & Turbulent Flow

Laminar flow occurs when fluid particles are arranged in smooth layers or laminas. These layers are usually parallel to each other and thus do not obstruct one another to cause fluctuations (Fox, et al., 2012). Laminar flow has regular and predictable behaviour but may be steady or unsteady. Steady flow is when the flow characteristics are the same at any instant in time as at any other instant in time (Cimbala, 2014).

Turbulent flow is when fluid particles rapidly mix due to random three-dimensional velocity fluctuations (Fox, et al., 2012). This eddying and random fluctuation causes more drag in unaltered, natural progression fluid flow (Fox, et al., 2012). Turbulent flow is always unsteady due to the random swirling present (Cimbala, 2014). It is characterised by irregular, chaotic behaviour (Cimbala, 2014).

In order to visualise this fluid flow, Figure 2-1 shows the laminar, parallel predictable behaviour on the lower part while the turbulent, swirling, chaotic behaviour is shown in the upper part.

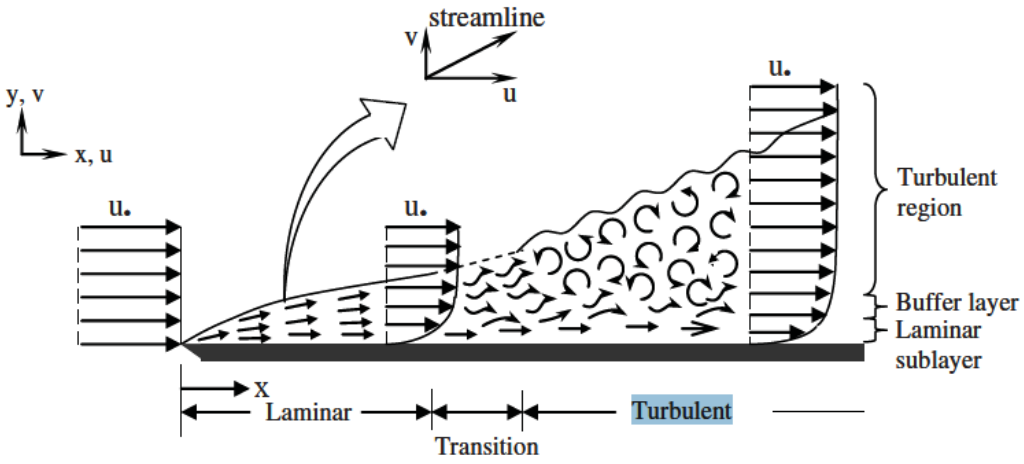

Figure 2-1: Laminar and turbulent flow (Sayma, 2009).

2.1.3. Visualising the Boundary Layer

Figure 2-2 shows how the velocity profile changes within the boundary layer when fluid flow is shown as it would appear on a flat plate while illustrating flow progression from laminar flow near the leading edge (origin) to turbulent flow at the trailing edge (some non-zero distance in the x direction).

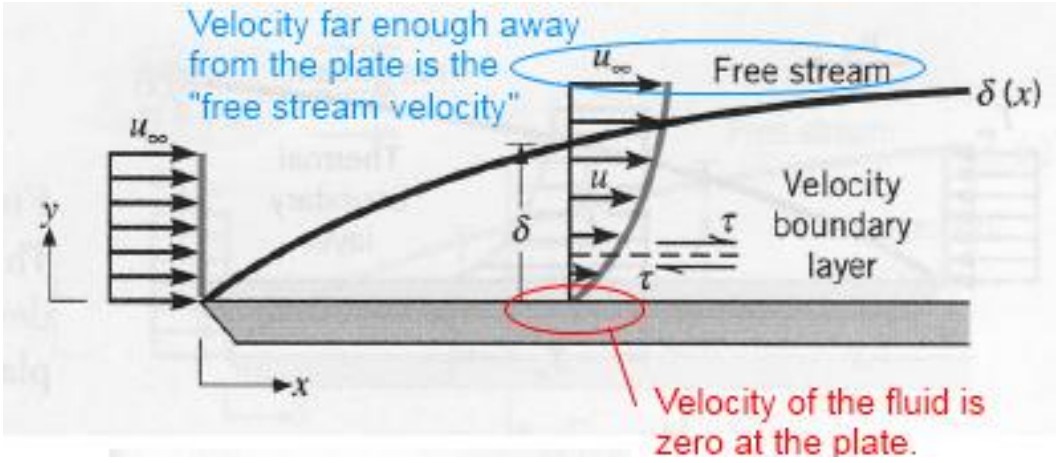

Figure 2-2: Velocity development in the boundary layer on a flat plate (Incopera, et al., 2007).

Specifically, the characteristics show that the fluid progresses from laminar to the (purely mathematical) transition region and thereafter turbulent. The velocity vector with a magnitude of zero shown at the object surface occurs as a result of shear forces causing the fluid molecules to become stuck to the body surface, thus affecting the molecules further from the body's surface, resulting in the velocity profile shown in Figure 2-2 (Incopera, et al., 2007).

2.1.4. Skin Friction

Skin friction is friction caused by shear forces between the fluid and body in contact (Fox, et al., 2012). It is dependent on and sensitive to Reynolds number. Viscous drag is hence the drag caused by skin friction applying a force, thus slowing down the body in contact with the fluid (Fox, et al., 2012).

The skin friction coefficient is given by equation 2-2:

$$C_f = \frac{\tau_w}{\left(\frac{1}{2}\right)\rho U^2} \qquad \text{Equation 2-2}$$

Using the skin friction coefficient, viscous drag may be calculated via equation 2-3:

$$F_v = \frac{1}{2}\rho U^2 A C_f \qquad \text{Equation 2-3}$$

These quantities are calculated once the unknown variables are found after analysing the fluid domain characteristics such as pressure distribution, velocity fluctuations and boundary layer characteristics.

2.1.5. Adverse Pressure Gradient

When static pressure increases in the direction of flow, it is known as an adverse pressure gradient. When this reaches a threshold value, it causes flow back towards the leading edge of the object in question (Chklovski, 1985). Figure 2-3 shows a velocity profile along the wall of an object; the near wall pressure builds along this profile. When at point "S_3", the adverse pressure causes a "back-flow" where vortices and hence increased drag results. This point is also known as the separation point (Chklovski, 1985).

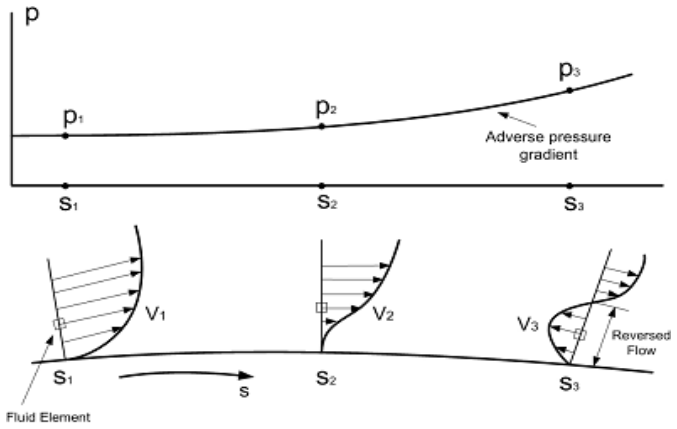

Figure 2-3: Adverse pressure gradient (Chklovski, 1985).

2.1.6. Flow Separation

Separation occurs when an adverse pressure gradient occurs in the boundary layer, which is a necessary condition for flow separation to occur but does not mean that it will always occur. Separation causes a wake or back-flow. Low-pressure results from this, and consequently a difference in pressure between the leading and trailing edges of the body; thus drag (Fox, et al., 2012). Flow separation is shown in Figure 2-4 as it occurs due to the adverse pressure gradient. The diagram illustrates the progression from (a) free stream airflow to (b) where the flow is naturally transitioning from laminar to turbulent and thereafter to point (c) where the adverse pressure gradient occurs, i.e. $dp/dx < 0$ (pressure gradient is in the opposite direction to the flow direction): and the flow thus separates toward points (d) and (e) where there is a low pressure occurring as a result (Fletcher, et al., 2014).

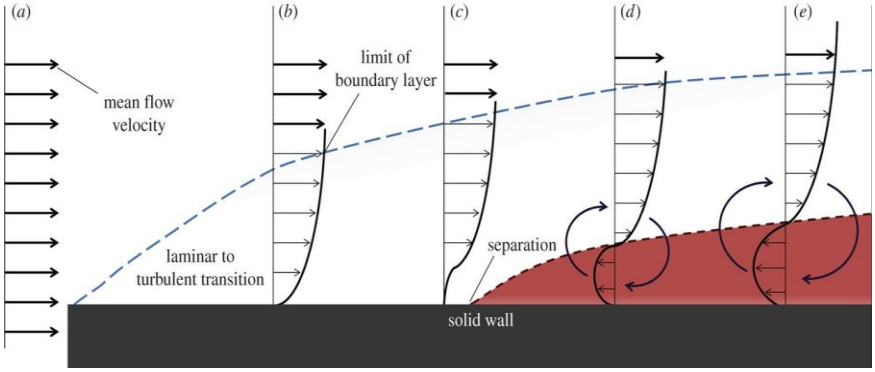

Figure 2-4: Flow separation (Fletcher, et al., 2014).

Separation therefore usually occurs after the turbulent flow has formed. If applied to an aerofoil, this occurs when the shear forces between the flow and boundary of the object become too high. These forces cause a vortex or low-pressure region to form and hence causes the negative pressure gradient between the leading and trailing edges, causing drag (Fletcher, et al., 2014), (Fox, et al., 2012). Linear stability analysis in CFD modelling allows for the prediction of where the flow turns from laminar to turbulent and thereafter where separation occurs. Estimating the separation point is vitally important in order to know where to place flow alteration devices such as trip wires and dimples. Altering the fluid flow over a surface in order to delay separation, by using devices as discussed by Groth et al. (2014), and thus reduce aerodynamic drag, is referred to as controlled turbulence (Groth, 2014).

2.1.7. Pressure Drag

Drag due to an adverse pressure gradient causing a sucking effect from the wake which is formed is known as pressure drag. This force equates to the difference or reduction in pressure between the leading and trailing edges of the body the fluid is interacting with, multiplied by the frontal area of the body.

Pressure drag is somewhat dependent on Reynolds number but not highly sensitive to it, while it is highly sensitive to the shape of the body in question (Fox, et al., 2012). Streamlined bodies have been designed to combat this negative effect (Fox, et al., 2012). Pressure drag is described by:

$$F_p = A_f \times (P_{leading} - P_{trailing})$$ Equation 2-4

2.1.8. "Controlled" Turbulence

Controlled turbulence may cause less drag than laminar fluid flow due to a turbulent boundary layer having higher momentum transported by the free stream flow to the flow near the wall flow (Bakker, 2006). This means that, for example, a laminar boundary layer cannot accommodate the increasing pressure or adverse pressure as effectively, and thus insufficient momentum exchange takes place allowing for the flow to separate more easily (Bakker, 2006). Turbulence increases skin friction as it is characterised by a larger/thicker boundary layer and thus has a larger amount of mass flow and fluid interaction. This allows for separation at a point further from the leading edge of the body in question. Separation at a point further from the leading edge allows for a reduction in the pressure difference between the leading and trailing edges of the object in question. The reduction in pressure difference results in a greater drag reduction than what is added by increased skin friction. Thus, a net gain in aerodynamic efficiency is achieved.

2.2. Computational Fluid Dynamics

The use of computer systems to simulate the fluid flow interaction with objects for, as one use among several, aerodynamic optimisation purposes, is widely used as a modern technique to mitigate the costs of developing wind tunnel models while also reducing lead time to having the final components manufactured and put to use. Computational fluid dynamics makes use of partial differential equations that represent conservation laws for the mass, momentum and energy of the fluid domain in question. Computer systems are thus employed to carry out calculations in order to give the desired quantities and thus provide a qualitative and quantitative prediction of the fluid flow. Mathematical modelling in the form of partial differential equations plus numerical methods and software tools are used and thus, as with most computer systems and software, there is uncertainty involved which is accounted for when post processing results (Celik, et al., n.d.).

Uncertainty in CFD is error throughout the CFD simulation process which may comprise of many factors with only some mentioned here. This error may be unavoidable due to unknown factors such as turbulence modelling not yet being fully understood (Hosder, et al., 2003). Uncertainty may occur through physical modelling errors, discretisation and solution error, programming error and computational round-offs (Hosder, et al., 2003).

As yet not all details, but approximations, are understood about turbulent flow which adds uncertainty to the calculation and modelling process used in CFD calculations (Hosder, et al., 2003). Further error estimating and convergence criteria are described in Section 2.2.7. Numerical methods comprise discretisation and several solution techniques depending on the desired values to be analysed (Kuzman, 2016). A tool widely used for discretisation, pre-processing, solving and post-processing of desired fluid domain and fluid interactions, is commonly known as STAR-CCM+. The methods used to employ this tool describing mesh (discretisation) and physics (fluid domain properties) detail specifications may be described by equations 2-5 to equation 2-17 in Sections 2.2.1 to 2.2.6. A fluid domain therefore requires discretisation and this discretised domain needs interpolation techniques applied in order to solve partial differential equations so that flow quantities may be known. The method is known as the finite volume method and the subcategories mentioned here are explained in the subsections to follow.

2.2.1. CFD Solvers and Meshing

An overview of the methods used by CFD methods is outlined briefly below. The use of these principles is employed by a majority of CFD simulation packages in some form.

Discretisation

This is the process of breaking up a large continuous domain into smaller sub-domains so that differential equations may be solved for these sub-domains and thereafter used to view the fluid domain characteristics for the entire domain (Cimbala, 2014), (Sayma, 2009). This is done in a similar manner to conducting lab experiments where flow quantities are taken at several points, the information thereafter combined, and differential equations solved for the overall domain fluid quantities desired (Cimbala, 2014), (Sayma, 2009). Differential equations are solved in order to combine the measured data and result in desired quantities which depend on the design objectives.

Interpolation

When quantities between the points chosen are desired, interpolation techniques are used. The number of points used directly influences the accuracy of the results (CD-Adapco, 2014), (Cimbala, 2014), (Fox, et al., 2012), (Sayma, 2009). In order for continuous differential equations to be solved for the discretised domain, a grid otherwise known as a mesh is constructed and explained later in this section. Differential equations are solved iteratively for the mesh points until an acceptable error is reached according to the convergence criteria stipulated in Section 2.2.7. STAR-CCM+ and several other CFD software packages involve the use of interpolation between nodes in a mesh to find values at all areas in the fluid domain not directly defined by an actual node in the mesh. The mesh defines part of the actual fluid domain being tested. This is done to reduce the size of the CFD model to usable sizes for computational systems to analyse.

Finite Volume Discretisation

Finite volume discretisation is a method of producing weighted residual equations by dividing the solution domain or fluid domain into sub-domains which are often referred to as control volumes (Sayma, 2009). The weighting function is then set to the value of one over each control volume while being set at zero over the other control volumes, as an approximation, which results in each residual to become near zero (Sayma, 2009). Finite volume discretisation may also be achieved by beginning with the integral form of the flow equations, such as Navier-Stokes equations, which equate the rate of matter accumulations to the rate of the flux passing through the boundaries, in this case when discretising fluid domains. Velocity, momentum or several other equations needed may be solved for each direction (x, y and z) in order to calculate the predicted fluid flow characteristics (Sayma, 2009). This means that the fluid domain is subdivided into non-overlapping smaller cells and the flux calculated through each (Sayma, 2009). The flow variables are then found through calculating the flux values through the volume boundaries, either on cell edges or at the centres. This may be manipulated to find a system of algebraic equations that may be used to solve for the unknown field variables (Sayma, 2009), (Cimbala, 2014), (Fox, et al., 2012).

Finite Volume Mesh Types

In order to make use of the differential equations for the finite volume method to be applied, a continuous fluid domain must be, as stated, discretised into a discrete fluid domain as may be intuitively realised. This is done by employing a meshing programme as described here. A mesh or grid is constructed and forms the discrete fluid domain so that the approximate solutions for the differential equations may be found at the grid/mesh points (Sayma, 2009), (Cimbala, 2014). Two main types of meshes exist; those that are structured and those that are not. Structured meshes are comprised of points, each point neighbouring another, and are therefore regularly structured (Sayma, 2009). Structured meshes comprise of elements that are orthogonal in the i, j and k (x, y and z) directions in 3-dimensional domains. Structured meshes have many advantages in coding as the coding is usually simpler and thus more efficient for solving purposes. Unstructured meshes comprise points that have a differing number of neighbours and thus have irregular connectivity. Unstructured meshes do not allow for a uniform pattern. These meshes are comprised of node numbers and a connectivity table and thus lack the i, j and k structure. STAR-CCM+ has the ability to make use of meshes that are structured, unstructured, or a combination of the two, by having a structured prism layer mesh with a polyhedral mesh grown from the prism mesh. A common method of meshing fluid domains is to use prism layer meshing to discretise the near-wall fluid flow which thus allows for accurate capturing of the boundary layer characteristics while polyhedral meshing may be used for discretising the free stream flow (CD-Adapco, 2014), (Sayma, 2009).

The algorithms that make use of structured grids are not able to use unstructured grids while the algorithms that use unstructured grids may be used on structured grids (Sayma, 2009). Structured grids are used on regularly shaped boundaries while unstructured grids should be used for irregularly shaped boundaries, such as curved boundaries. Algebraic equations may be used to interpolate a grid from the object's boundaries (Sayma, 2009). A structured mesh type used in STAR-CCM+ is known as trimming mesh, which discretises the fluid domain into rectangular and square cells that are trimmed at boundaries; the flow equations are then calculated through these cells and the trimmed grid points used (CD-Adapco, 2014). This method is used when the flow is linear and yields less accurate results, but they are solved quicker and the method is robust in capturing complex geometry (CD-Adapco, 2014), (CFD Online, 2011), (De Wet, 2013).

Meshes may be polyhedral, hexahedral, triangular, tetrahedral, prisms and bricks (Sayma, 2009). The meshing of the fluid domain must always: be closed and manifold (no holes); have no self-intersections; have no overlapping faces; have no duplicate joints between faces; conform to the boundary of the domain; and have smooth grid density variation, in order for the finite volume method to be applied. The mesh must be scalable to ensure that the computational resources available allow for accuracy in the solution (Sayma, 2009). A commonly used mesh type in STAR-CCM+, due to its robust nature in capturing complex fluid domain shapes as well as allowing for solution accuracy and mesh scalability, is the polyhedral mesh type. Prism layer meshing is then applied to the objects wall in order to allow accurate discretisation of the boundary layer flow characteristics (CD-Adapco, 2014), (De Wet, 2013). Many mesh types are available for meshing fluid domains while the study of all is not applicable here and thus only a brief explanation is given.

Boundary and Prism Layers

A prism layer is a layer of cells (mesh) used in most CFD software, also known as inflation layers, to allow for the capture of boundary layer flow characteristics (Fox, et al., 2012). An example of prism layer meshing is seen in Figure 2-5.

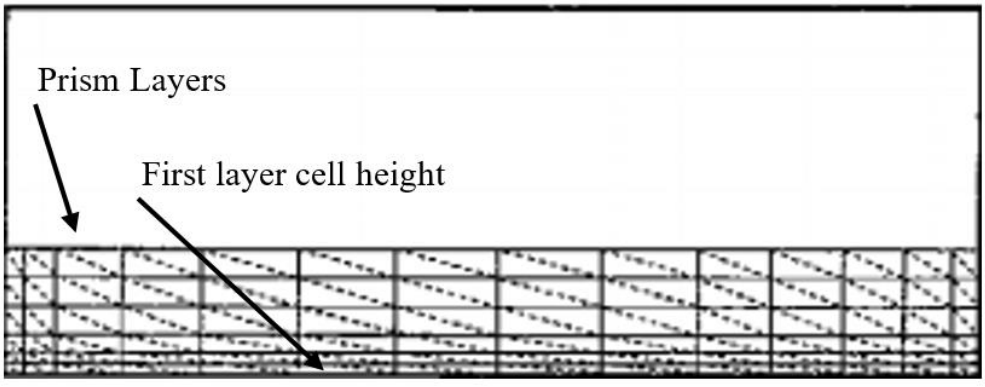

Figure 2-5: Prism layers (Garimella & Shephard, 2000).

In order to accurately capture boundary layer fluid flow, it is vitally important to define the mid-cell height of the first prism cell and the total prism layer thickness (boundary layer thickness) at the trailing edge which is the thickest zone (De Wet, 2013). The analytical methods used to define the prism layer specifications for the discretization of a fluid domain to be captured accurately is shown from equation 2-5 to equation 2-12.

Firstly the Reynolds number is calculated to describe the turbulence characteristics of the fluid using approximations for specific Reynolds number values:

$$Re = \frac{Ux}{\upsilon}$$ Equation 2-5

The skin friction coefficient describes the friction against the object surface caused by the fluid being attached to the surface causing shear stresses and thus causing a component of the total drag:

$$C_f = \frac{2 \times 0.036}{Re^{0.2}}$$ Equation 2-6

The wall shear stress is calculated so that the total stress caused by the skin friction imparted from the fluid on the object surface may be defined in order to calculate the dimensionless velocity and thereafter the wall coordinate so that the boundary layer thickness may be approximated:

$$\tau_w = C_f \times \rho \times \frac{U^2}{2}$$ Equation 2-7

Dimensionless velocity, used so that the wall coordinate may be calculated in order to approximate the total boundary layer thickness (De Wet, 2013), (Fox, et al., 2012):

$$u^* = \sqrt{\frac{\tau_w}{\rho}}$$ Equation 2-8

The wall coordinate used for estimating flow characteristics, whether laminar or turbulent (De Wet, 2013), (CD-Adapco, 2013):

$$y^+ = \frac{u^* \times y}{\upsilon}$$ Equation 2-9

First prism layer "mid-cell" height (Assume y^+ = 1 as used for low Reynolds number flow, ranges from 0 to 300 for well-resolved boundary layer flows in CFD testing (De Wet, 2013), (Fox, et al., 2012), (CD-Adapco, 2014)):

$$y = \frac{\upsilon}{u^*}$$ Equation 2-10

First prism layer cell height = $2y$

Stretching factor

A stretching factor is a ratio by which each prism layer's size is increased or grown when progressing from the object's surface on which the boundary layer is formed. This growth rate adopts a simple geometric series as the size progression rate which enables accurate prism layer definition in order to accurately capture the boundary layer flow (CD-Adapco, 2014).

When specifying the first prism layer height, the stretching factor may be calculated using equation 2-11. This ensures that the number of prism layers within the total calculated boundary layer height allows for the correct spacing and growth rate (ranging from 1.3 to 1.5) - see equation 2-13. This allows the velocity profile, as it progresses from the object's surface to the free stream flow, to be accurately captured. Equation 2-13 takes into account the first layer cell height and allows for the correct stretching to occur so that the correct velocity profile may be attained (Fox, et al., 2012), (CD-Adapco, 2014).

Geometric progression (Roberts, 1998-2012):

$$u = a \times r^{n-1} \qquad \text{Equation 2-11}$$

Rearranging equation 2-11:

$$r = \sqrt[n-1]{\frac{U}{a}} \qquad \text{Equation 2-12}$$

The condition is imposed so that the stretching factor falls within the following constraints (CD-Adapco, 2014).

$$1.3 \leq r \leq 1.5 \qquad \text{Equation 2-13}$$

2.2.2. Physics Models & Solvers

Physics models and solvers used and their use is explained, and which to use is outlined in Chapter 3, Section 3.5.4. Airflow with a Mach number less than one may aid the assumption of which model or solver to use when describing the fluid flow characteristics.

Dimension of the Fluid Domain

CFD programmes may be able to use a two-dimensional approach to solving fluid domain characteristics. This is only applicable to simple cases where the geometry has a two-dimensional shape and may, therefore, be modelled as such for reduction of computational resource use. Most CFD models involving solar vehicles, electric vehicles, motor vehicles and other aerodynamic models are three dimensional and even sometimes asymmetrical (CFD Online, 2011), (Cimbala, 2014).

Steady State or Transient CFD Modelling

Steady state modelling involves the iterative solving of the flow equations while not accounting for acceleration, while transient modelling accounts for acceleration (Dumas, 2008), (Kuzman, 2016). Thus, steady flow does not depend on time while transient flow does. When solving the differential equations describing the fluid flow in the domain, the time and higher order terms are ignored when the steady state solver is used as the time-dependent variables go to zero. Transient simulations are this usually more accurate as the solver incorporates these time-dependent variables. Transient solvers are not always needed as the simulation fluid domain and flow characteristics may provide an accurate even when the time dependent variables are ignored.

Flow Solver Methods

When running the solver, two methods may be employed for the solver to follow, namely segregated or coupled. The segregated flow solver is commonly used for low-speed subsonic flow.

The coupled solver is commonly used for supersonic flows (De Wet, 2013), (Bakker, 2006), (CD-Adapco, 2014). The segregated flow solver should be used for flows with a Mach number lower than 0.3, and the coupled flow solver for speeds higher than Mach 0.3 (CD-Adapco, 2014), (De Wet, 2013).

The segregated solver splits the overall set of flow equations into smaller more manageable equations which are solved in a segregated iterative manner after which the total result can be computed (Bakker, 2006). This procedure is shown in Figure 2-6. The flow characteristics are for vehicle aerodynamics and thus the airflow is characteristics by a Mach number less than 0.3. The coupled flow solver is not reviewed as it is not necessary for this type of flow.

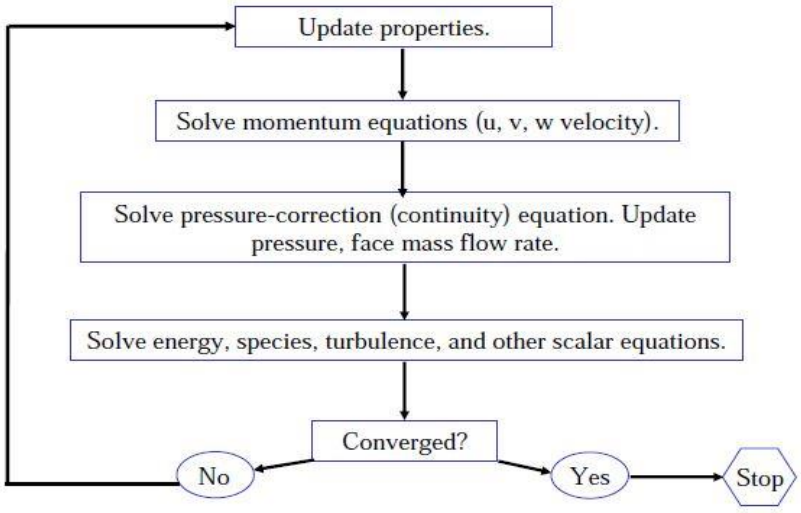

Figure 2-6: Segregated Flow Solver (Bakker, 2006).

Compressibility

The compressibility of a fluid must be considered according to flow speed. When analysing a fluid which has a flow speed of less than Mach 0.3, the fluid, if gaseous, is assumed to be incompressible and thus assumed to have a constant density (De Wet, 2013), (CFD Online, 2011), (Cimbala, 2014).

Turbulence Modelling

Turbulence modelling is the procedure used by CFD tools such as STAR-CCM+ to capture the turbulence induced by fluid flow when interacting with an object. It is implemented by having the computational analysis close a system of mean flow equations.

The main methods which allow calculation of the necessary turbulence models that may be used to describe flow characteristics of external aerodynamics analyses are, namely, Reynolds averaged Navier-Stokes (RANS), large eddy simulation (LES), direct numerical simulation and detached eddy simulations (DES). For the application at hand, a common methodology incorporates the use of the RANS type, as well as the K-Omega SST turbulence model as the airflow and fluid domain are used to describe turbulence characteristics of an external aerodynamic airflow (Bakker, 2006), (Sayma, 2009). This is a reasonably accurate and efficient way to describe the airflow for such a case. Mathematical modelling of the turbulence involves decomposing the Navier-Stokes equations using Reynolds averaging and closure of the resulting equations (Sodja, 2007).

2.2.3. Gamma Re-Theta Transition Model

The Gamma Re-Theta transition model is applied when accurately modelling transitional flow characteristics which is vitally important for the positioning of flow alteration devices and predicting drag accurately. Gamma Re-Theta transition modelling may be used via two customisable settings (CD-Adapco, 2014):

- An optimised “Suluksna-Juntasaro” algorithm.
- User field function.

The user field function is more applicable to the case at hand due to the accurate boundary layer specification, defining the boundary layer flow characteristics by using the distance from the boundary in question to the free stream flow, i.e. the boundary layer thickness. The Suluksna-Juntsaro algorithm, however, would predict the transition characteristics using the specified mesh (De Wet, 2013), (CD-Adapco, 2014). In order to implement the model in its simplest form, the model is selected as a physics solver and the Suluksna-Juntsaro method is selected. This allows for transition modelling to predict the transition of fluid flow by making the CFD software implement another set of turbulence equations (De Wet, 2013).

2.2.4. Advanced User Settings

Advanced settings available in the STAR-CCM+ interface allow the user to further customise the mesh and physics details to a higher degree to capture more intricate details of the models. This requires a greater understanding of CFD principles and STAR-CCM+, often improving the accuracy of the CFD simulations. The three terms explained below are programme specific settings for STAR CCM+ but are applied in many other CFD programmes in equivalent ways.

Gap fill percentage

Gap fill percentage allows the user to modify prism layer thickness wherever two surfaces are close to each other. This allows the degree of which certain voids are filled in the prism layer mesh to be set, resulting in more accurate boundary layer flow calculations in gaps or corners created by boundaries that meet each other, are perpendicular to each other, or meet at curves (CD-Adapco, 2014).

Each prism layer's thickness is calculated by multiplying the gap fill percentage default value of 25% by the intersection distance. Intersection distance is the normal distance between the two intersecting boundaries. However, in the case where a boundary has no prism layer activated as in the case of a symmetry plane, the maximum prism layer that will be formed is double the gap fill percentage multiplied by the intersection distance (CD-Adapco, 2014). This setting is increased to minimise the effect of having the prism layer subsurface thickness reduced near the intersection point of the two boundaries (CD-Adapco, 2014).

Minimum thickness

The minimum thickness setting constrains the subsurface prism layer thickness to a percentage of the global prism layer thickness. This constraint is set so that if reached, the subsurface prism layer thickness is forced to zero. The purpose of this technique is to reduce the number of poor quality cells arising in the mesh due to attempting to fit many layers in a thin section. This happens when surfaces are close together and thus the intersection of the prism layers on either may intersect and are thereby squeezed into a thin section (CD-Adapco, 2014).

Layer reduction

As mentioned above, when prism layers are on corners, intersections, curved surfaces and similar geometry, the need to reduce the thickness of the prism layer/s is essential to allow for accuracy.

This percentage thickness reduction is applied locally on a specified boundary or using a specific control volume, and allows for local mesh control. When a volume refinement is used, the prism layers within the volume shape are subject to the layer reduction in the same way. When changing the layer reduction property, it changes the point at which the number of layers in a contracting prism layer is reduced and its percentage is set as a percentage of the overall prism layer thickness.

This technique acts to reduce the thickness and number of prism layers wherever the thickness of the total prism layer falls below the specified percentage, with a default setting of 50%. Thus, when the actual prism layer thickness falls to half of the required thickness, layers begin to be removed so that the aspect ratio and stretching factor are kept low and within the tolerance for a reduced amount of error (CD-Adapco, 2014).

Layer reduction does not have any effect when there is only one prism layer present. Using 100% as the layer reduction setting would cause the entire boundary layer mesh to be reduced by a complete layer at a time. It is recommended that 25% to 75% be used (CD-Adapco, 2014).

2.2.5. Best Practices in Volume Meshing

One must ensure that the values obtained through CFD testing are checked via various scalar and vector scenes as well as relevant reports so that the results may be verified and compared to anticipated results. In some cases, the model might have arbitrary areas of unpredicted or outlier results, such as high wall y+. These areas will need mesh refinement applied for error reduction.

Mesh Quality Checks

In order to ensure that the mesh used is accurate enough to allow the solution accuracy not to be degraded, there are guidelines to be followed to ensure that the mesh skewness, density and settings are correct. The following general rules were prescribed by Memon (2012):

- Cell angle > 18 degree
- Mesh quality > 0.3 – determined by the solver's robustness, as the solver will diverge if it is not robust enough to account for bad quality cells.
- Cell expansion rate (change of cell volume with respect to neighbouring cells) < 10 or as prescribed by the programme/solver used.
- Skewness: 0.8 – 0.95.
- Aspect ratio < 100 for single precision and 1000 for double precision though studies show that up to 8000 in the boundary layer allows for accurate results unaffected by the change of aspect ratio. This method is not suitable for transition prediction and was thus not used in this study.

2.2.6. Motion characteristics for CFD (Wheels):

When modelling the motion of the solar car, simply assigning a flow velocity to the virtual wind tunnel inlet would have been insufficient for the required accuracy. Therefore in order to assign motion to the wheels, the wheel rotational velocity was calculated using equation 2-14 to 2-17 (Fox, et al., 2012), (CD-Adapco, 2014), (Fox, et al., 2012).

$$v = R \times \omega \qquad \text{Equation 2-14}$$

Rearranging equation 2-14:

$$\omega = \frac{v}{R} \qquad \text{Equation 2-15}$$

To get RPM (revolutions per minute):

$$\omega = \frac{2\pi N}{60} \qquad \text{Equation 2-16}$$

Rearranging equation 2-16:

$$N = \frac{60\omega}{2\pi} \qquad \text{Equation 2-17}$$

2.2.7. Convergence

When conducting CFD simulations using the steady state approach, the CFD analyst must ensure that the simulation has reached a point where the results are no longer fluctuating while ensuring that the simulation has resulted in the least estimated error possible (LEAP Australia, 2012), (Pointwise, Inc., 2012). The convergence of steady state CFD simulations requires certain criteria to be met for confidence that the converged simulation results do not fluctuate beyond specified tolerances; the process is known as iterative convergence. The values used to quantify associated error are known as the residuals and are defined below (Slater, 2008).

Residual Convergence

The fluctuation in the results of the flow definition equations such as turbulence models and Navier-Stokes equations, as they approach convergence over the iterative process, are known as the residuals (Sayma, 2009). They can be scaled or normalised and are usually seen as converged when they level off at a certain set of values to indicate iterative convergence. The residuals commonly seen as converged, are seen as such when reaching 3 to 4 orders of magnitude lower than when the simulation has been commenced. This also illustrates the error in the simulations (Slater, 2008), (LEAP Australia, 2012), (CFD Online, 2011).

Result Convergence

When conducting CFD simulations the objective is to obtain the characteristics and values of quantities such as drag forces, lift forces and force coefficients. Several other quantities may be required depending on the design objectives. These values may be plotted according to the iterations of calculations undergone throughout the simulations and thus certain tolerances and acceptable error may be accepted. This process ensures a high degree of repeatability when comparing models. Using a steady state approach, as is done in this work, when iterative convergence is reached, final values should stabilise (Slater, 2008), (Bakker, 2006), (CFD Online, 2011), (LEAP Australia, 2012).

Many students and engineers hold the false belief that if the residual error is below 1×10^{-4}, that the solution has converged. The assumption is false because there may be cases where although the error (and thus residuals) is low, the results may not have stabilised within an acceptable range. Residuals are the first indication of the amount of error in the solution of a simulation (CFD Online, 2011). The convergence of residuals is illustrated in Figure 2-7 and are shown to reach a steady solution.

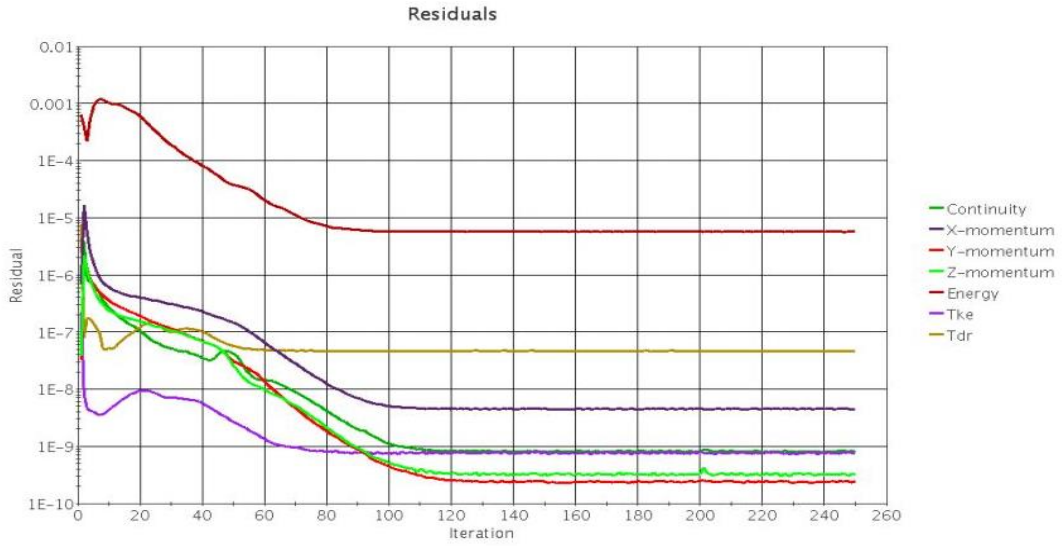

Figure 2-7: Residual Convergence (CD-Adapco, 2013).

The solution domain must have imbalances (fluctuations) or results with each subsequent result value within 1% of the previous iteration value, which has a different mesh count and/or modelling technique. The stabilised result iteration plot is shown in Figure 2-8 where the force coefficient has converged (LEAP Australia, 2012), (CD-Adapco, 2013).

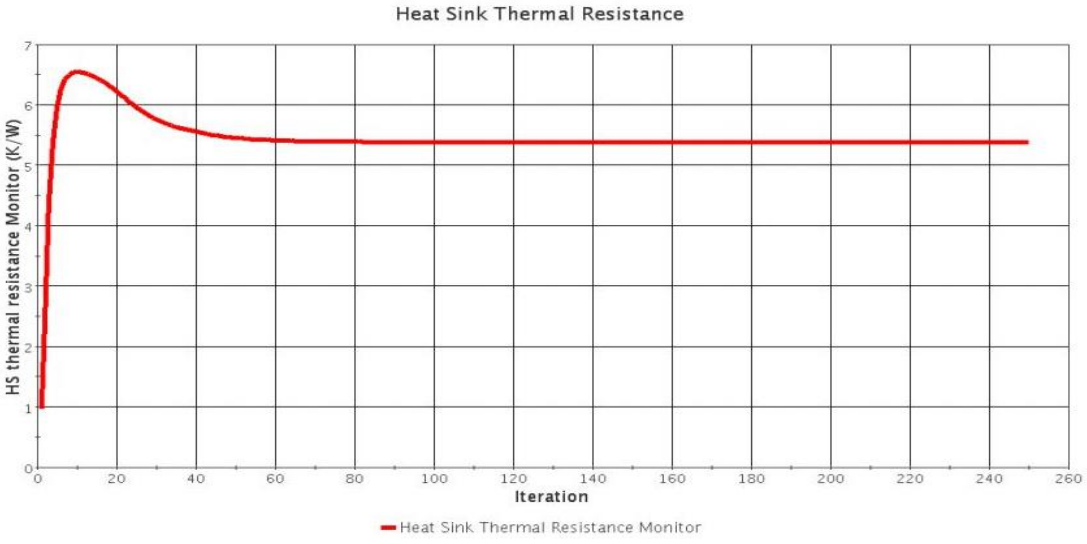

Figure 2-8: Result Convergence (CD-Adapco, 2013).

These criteria allow converged as well as repeatable results. If these criteria are not met, the results would change if the simulation was to run, for example, a hundred more iterations (LEAP Australia, 2012), (CD-Adapco, 2013).

Mesh Independence

When performing a simulation, the need for mesh independence is essential. When an increasing mesh count is used such that it results in similar values to the previous, lower mesh count results, it is said to have reached mesh independence. Mesh independence would, therefore, have tolerances applied by choosing a certain order of magnitude error as acceptable when investigating residual convergence. One may also accept results with a fluctuation of 1% when compared to the previous iteration result value (LEAP Australia, 2012), (Pointwise, Inc., 2012).

Once the solution has converged according to the specified criteria, the user must still ensure that the results are mesh independent. Mesh independence is reached by ensuring that results do not fluctuate as a result of increased mesh count. Mesh independence is found by refining the mesh details and obtaining progressively higher mesh count until the results are within the user specified tolerance of the previous model (CD-Adapco, 2013), (De Wet, 2013), (Cimbala, 2014).

A simple mesh count versus results plot may be used to illustrate mesh independence in Figure 2-9.

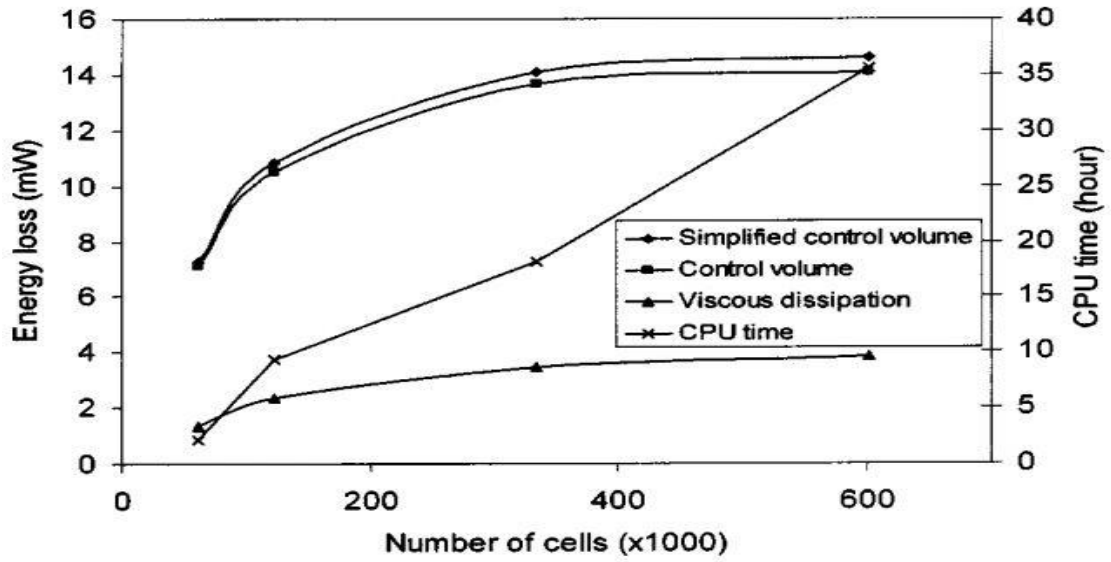

Figure 2-9: Mesh Independence and CPU time against no. cells (Liu, et al., 2004).

A common error when conducting computational fluid dynamic simulations is that mesh independence is not reached when the final results are acquired.

Mesh independence is not always needed when comparing flow alteration techniques, although it is essential to keep the mesh details the same as this allows for accurate comparison (LEAP Australia, 2012), (CFD Online, 2011), (Sayma, 2009).

To establish and achieve mesh independence it is common to apply the following methods iteratively.

- Ensure that the initial mesh results in values which concur with the convergence criteria and if not, that the mesh details be refined until the simulation reaches convergence (Sayma, 2009).
- When convergence is reached, increase the mesh size by a generally accepted 1.5 times. This would be achieved by adjusting global mesh details until the mesh element count reaches 1.5 times the previous number of mesh elements. Reducing the actual mesh sizing by halving the values used would increase the number of mesh elements. Mesh sizing greater than or less than these mesh independent values may be used to find the lowest total number of mesh elements mesh possible. However, if mesh independence is reached, the lowest amount of mesh elements of these is sufficient (Sayma, 2009).

2.2.8. Simulation Comparison Techniques

Several techniques may be used for CFD model comparison while only the following were used. These were chosen as they were sufficient for analysis purposes in order for accurate comparisons to be made. Scalar and vector scenes may be used in CFD analyses to determine the transition and separation points of the fluid flow along the surface of the object in question, more easily. Quantities of the highest importance for determining the placement of flow alteration techniques are discussed in Section 2.3.

Turbulent Kinetic Energy (TKE)

TKE is associated with eddies or vortices that occur due to high amounts of turbulence resulting from separation, i.e. in the wake region. Turbulent kinetic energy is a measure of the intensity of turbulence. It is the degree of kinetic energy possessed by the fluid that is considered turbulent (Šavli, 2012), (Cimbala, 2014), (Fox, et al., 2012).

When a scalar plot is set to show only the parts of the fluid domain in question that have a TKE higher than 0.1 J/kg, a common method used to show the turbulent transition and separation regions (De Wet, 2013). This being dependent on the inlet flow conditions, the aforementioned condition would apply to an external flow analysis (De Wet, 2013), (Fox, et al., 2012), (Cimbala, 2014).

Turbulent Viscosity Ratio (TVR)

The turbulent viscosity ratio is the ratio of the turbulent viscosity to laminar viscosity, which gives insight into how turbulent the flow is (Bakker, 2006), (Fox, et al., 2012), (Cimbala, 2014), (De Wet, 2013), (CD-Adapco, 2014).

Vorticity

Vorticity describes the curl of the velocity field. This gives insight into the swirling characteristics of a fluid (Shapro, 1969), (Fox, et al., 2012), (Cimbala, 2014).

Turbulence Intensity

Turbulence intensity is defined as the ratio of the root-mean-square of the velocity fluctuations to the mean flow velocity (CFD Online, 2011), (Sayma, 2009). It is used as an illustration of the amount of turbulence in a system (De Wet, 2013), (Fox, et al., 2012), (CD-Adapco, 2014), (Cimbala, 2014).

Pressure

The pressures characteristics that result from applying flow conditions and conducting the CFD simulation, may be plotted on the desired geometry regions. This may then allow insight into why the required results are accurate and show certain global flow characteristics.

Required results may include forces, swirling, turbulence characteristics and several others (De Wet, 2013), (Fox, et al., 2012), (CD-Adapco, 2014), (Cimbala, 2014).

Wall Shear Stress

The wall shear stress in the sense of CFD is the shear stress applied to the wall of the body in question by the fluid flowing over it. Thus, it is intuitive that when a high shear stress is present, the fluid is attached to the surface. When the shear stress is then extremely low (in comparison to the shear stress nearer the leading edge) near the objects trailing edge, the flow is taken as detached (De Wet, 2013), (Fox, et al., 2012), (CD-Adapco, 2014), (Cimbala, 2014).

Wall Y+

A Wall Y+ scalar plot is used to verify the integrity of the boundary layer resolution so that the desired flow characteristics may be considered acceptable for certain desired flow conditions (De Wet, 2013). For example, the wall y+ scalar plot may be set to have a maximum of 1, meaning that the flow characteristics correspond to a boundary layer that has been fully captured with the turbulence characteristics anticipated when applying low wall y+ treatment. The k-Omega turbulence model requires low, high or all y+ treatment for accurate turbulence modelling with ranges of 0 to 1 or 30 to 300 for low and high wall y+ treatment respectively.

All y+ treatment allows for accurate resolving of flows with wall y+ values in the 0 to 300 range. (CD-Adapco, 2014), (De Wet, 2013), (Cimbala, 2014), (Fox, et al., 2012).

Streamlines

Streamlines are used purely for visualisation of the flow field with various quantities applied to them such as absolute pressure, viscosity, TKE, TVR, and several others, are discussed in the results analysis sections.

Streamlines do not give a complete representation of the flow field and hence scalar and vector scenes are used in conjunction with these (CD-Adapco, 2014), (De Wet, 2013), (CD-Adapco, 2014).

Drag Forces and Coefficients

An efficient and accurate way of comparing results is to analyse the drag forces and coefficients applied to the parts in question once mesh independence has been achieved (CFD Online, 2011), (CD-Adapco, 2014). These are often the results most important for the system and often used for direct comparison between designs tested (De Wet, 2013), (Fox, et al., 2012), (CD-Adapco, 2014), (Cimbala, 2014).

Comparison Technique Conditions

The above methods may be applied if and only if the models are accurate enough and the following conditions are met (as mentioned earlier and shown in results):

- y^+ value below 1 and low y^+ wall treatment (Fox, et al., 2012).
- At least 10 prism layers or use as calculated for an accurate mesh (De Wet, 2013).

2.2.9. CFD Applied to Vehicle Aerodynamics Optimisation

The optimisation of drag and lift coefficients applied to a simple vehicle geometry by the incident airflow was investigated by Ahmed & Chacko (2012), and the findings show blockage effect mitigation methods as well as results analysis techniques similar to those mentioned in Section 2.2.8 (Ahmed & Chacko, 2012). The effectiveness of applying airflow alteration devices, such as vortex generators, was analysed and proven to reduce drag and increase downforce. These devices are similar to those mentioned in Section 2.3 (Ahmed & Chacko, 2012). The application of CFD to analyse the effects of airflow on vehicle aerodynamics is essential for design lead time reduction as well as improving overall resulting efficiency gain from applied devices (Othmer, 2014), (Ekman, et al., 2016). CFD is used to analyse the duct effectiveness as well as the optimisation of topology such as surface shape modification with vortex generators (Othmer, 2014), (Ahmed & Chacko, 2012), (Patil, 2012).

Scalar plots may be used to analyse the effectiveness of airflow manipulation of external aerodynamic flows; these show that separated regions may require alteration of the surface topology in certain areas to keep airflow attached, if unable to do so through other methods (Othmer, 2014), (Ahmed & Chacko, 2012). Methods of flow alteration such as blowing and suction are also analysed and shown to have applicability in certain regions only (Othmer, 2014).

The analysis of incident air and crosswinds on vehicle aerodynamics may be investigated through the use of CFD in order to predict flow characteristics resulting from applied fluid conditions applied to vehicles and other objects (Carbonne, et al., 2016), (Ahmed & Chacko, 2012), (Dumas, 2008), (Cimbala, 2014).

2.3. Flow Control/Alteration Devices

An overview of flow alteration devices to be investigated is shown in this Section. Tripping of air flow along an entire surface is first defined. The application of this principle in the form of flow alteration devices strategically placed to trip the flow from laminar to turbulent is discussed thereafter. Strategically causing turbulence should in turn cause separation to occur at a point further from the leading edge of an object. In some cases, contrary to popular belief, inducing turbulence in strategically placed zones can decrease total drag by reducing viscous drag (due to the air being at zero velocity on the car's surface when laminar, and non-zero when turbulent) (Salaverry, 2012). The turbulent flow may have increased kinetic energy by accelerating the air flow near the surface of the body in question (Salaverry, 2012). The previous statement may seem doubtful, although when the resulting separation region is considered, the overall aerodynamic drag induced may be reduced as a result. The reduction in the size of the separation region through the use of turbulence addition devices is usually only used in cases where there is a large amount of separation occurring, such as bluff bodies. The application of these devices to streamlined surfaces is slightly more challenging due to the surface bulk shape being previously optimised prior to boundary layer alteration via external devices outlined in this Section.

Separation may occur in a similar fashion to an aeroplane wing at an angle of attack or when the solar car, or another streamlined body, is subject to crosswinds. Investigations into reducing the separation region size and hence aerodynamic drag induced will therefore be investigated.

2.3.1. Dimples

Golf ball aerodynamics or dimpling of golf balls for favourable aerodynamic effects is investigated here. Dimpling originated from golf balls becoming scratched and dented through continuous use, it was observed that a scratched and dented golf ball flew further and more accurately than a smooth one (Butt & Egbers, 2013).

Golf balls are however bluff bodies and not streamlined as is the solar car. The same principles may be applied to bluff and streamlined bodies. An analysis was performed in search of the best application techniques to streamlined bodies since dimple geometry affects aerodynamics significantly and is thus extremely important in this study (Dol, 2013). The most important aspect when applying dimples is to find the optimal dimple specifications:

- Depth
- Diameter
- Meniscus shaped or flat bottomed (Shape)
- The density of fluid over the surface of application – air in this case.

Through research, the best specifications were to be found. If this proved inconclusive, yielding no improvement in aerodynamics, the best specifications would be found through testing and analysis of several configurations. Testing and analysis were most likely, due to the dimple effect not yet being applied to such streamlined bodies with substantial evidence to be used as an accurate reference for aerodynamic drag reduction to be apparent. Substantial evidence would have allowed for more specific dimple sizing and thus more drag reduction would be apparent. Flow control over aerofoils using differently shaped dimples investigated by Srivastav (2012), yielded the following findings (Srivastav, 2012):

- Dimples have a more positive effect on bluff bodies than streamlined bodies due to the fact that streamlined bodies are shaped in such a way that pressure drag is reduced at zero angle of attack, while bluff bodies suffer predominantly from pressure drag.
- It was found that dimples allow for the separation point to be delayed further down the aerofoil, causing less of a pressure gradient and thus less drag, though the majority of the testing has been done on aerofoils at an angle of attack.
- It was found that outward protruding dimples, similar to vortex generators, may yield greater performance enhancement than recessed dimples. However, further testing of the concept to find a definitive result would be required while using more applicable methods for the streamlined body application at hand. Though vortex generators may yield even larger performance enhancement than outward protruding dimples would.
- Results pointed towards dimpling having a positive drag reducing effect at zero angle of attack although the effectiveness on streamlined bodies may be less than when applied to bluff bodies. Aerodynamic drag may be reduced when applied to streamlined bodies.

Aerodynamic characteristics of flow over simple circular cylinders with patterned surfaces were investigated by Butt and Edgers (2013), this investigation discusses bluff bodies.

It was found that hexagonal protrusions alter the flow over simple cylinders achieving as little as 65 % percent of the original drag on a body with a smooth surface. It was believed that outward protruding hexagonal bumps of 156 mm diameter were optimal having a depth to diameter ratio of 1.98×10^{-2} (Butt & Egbers, 2013). Dimples of different sizes and shapes were analysed by Aoki et al (2009), the results of which would substantially aid the research topic at hand although it was an investigation into bluff bodies. This analysis investigated air flow over a sphere while taking into account the effect of varied dimple geometry. Figure 2-10 shows the results (Aoki et al., 2009).

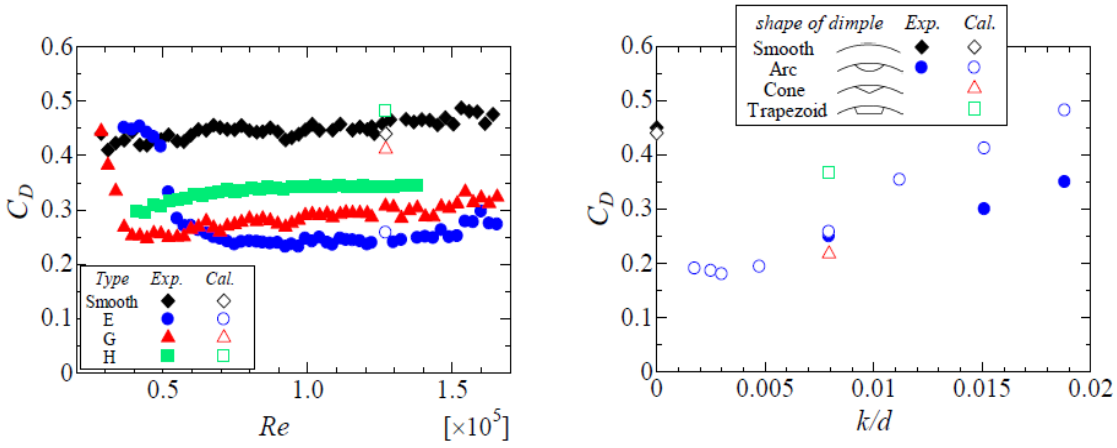

Figure 2-10: Dimple shape and sizing (Aoki, et al., 2009).

Figure 2-10 shows that arc shaped dimples prevailed at an optimal dimple depth to ball diameter ratio of 0.003 when applied to cylinders. The nomenclature for the application at hand is given in Figure 2-11.

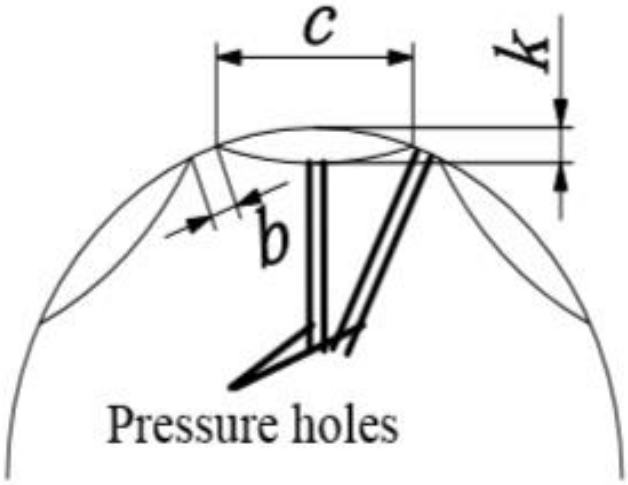

Figure 2-11: Dimple nomenclature (Aoki, et al., 2009).

The optimal dimensions to be used for incorporation in the design of dimples were found to be as follows:

- k/c = 0.0362
- c/d = 0.0828
- b/d = 0.0152
- k/d = 0.003

Different golf ball manufacturers and dimple specifications were compared showing that shallow circular dimples with a large angle between the edge of the dimples and the outer shell circumference, as shown in Figure 2-12, were most effective at the relevant Reynolds numbers (Aoki, et al., 2009).

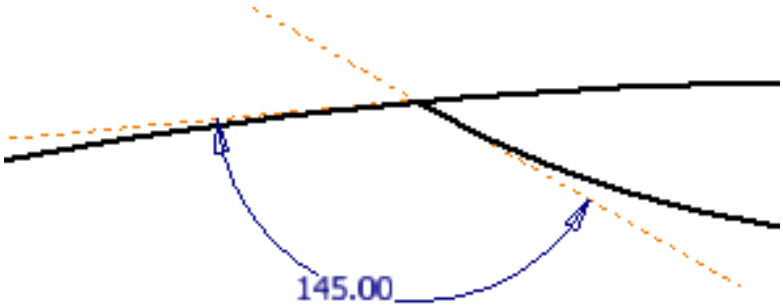

Figure 2-12: Dimple angle (Aoki, et al., 2009).

2.3.2. Wheels

Wheels may be optimised by removing or reducing the excessive separation caused by the rotating spokes of the wheels. The aerodynamic drag caused by the excessive separation and vortices has been mitigated by covering said spokes with smooth or dimpled wheel covers. Here, excessive separation is apparent if there are no covers present. Slight separation may still occur and this may be reduced by the addition of dimples or similar apparatus to the smooth wheel covers.

Dimpled disc wheels were developed by ZIPP Cycles engineers to improve aerodynamic efficiency in cycling. These modified wheels provided significant improvement: in some cases providing slight negative drag at approximately 50 kilometres per hour (kph) when at an incident wind angle of 15%. This was observed when testing the ZIPP 900C Model 3 wheel (Cyclery, 2007). A similar concept was to be considered for application to the wheels used on “Iklwa,” unless the team decided to buy optimised wheel coverings from ZIPP Cycles.

ZIPP wheels were tested in a slightly different way to conventional testing methods for cars, by spinning them while measuring the total energy needed to spin the wheel, and also testing for aerodynamic drag, lift and crosswind drag (Cyclery, 2007). When investigating dimple sizing as a percentage of length on ZIPP wheels, as can be seen in Figure 2-13, the percentage dimple diameter to wheel diameter may be considered. Two dimple sizes were applied to the low curvature surface of the cover. Percentage dimple to wheel diameter is seen to be approximately 0, 85 % and 1, 4 %.

Figure 2-13: ZIPP wheel (Cyclery, 2007).

The design of Garneau helmets by Louise Garneau (2014), allowed for further insight into dimple sizing as these helmets were designed to be streamlined like the canopy (Garneau, et al., 2009). Figure 2-14 shows dimple sizing on a Garneau helmet and, using the same percentage diameter approach as used for ZIPP wheels, here the percentages are for dimples applied to high curvature surfaces. The dimples range from approximately 1.38 % to 3.04 % dimple diameter to body length.

Figure 2-14: Garneau helmet (Garneau, et al., 2009).

Figure 2-15 shows the application of dimples to the Hexa solar car (Bez, 2012). Dimple sizing was investigated to be approximately 1, 25 % when investigating the percentage of dimple size to car length; this percentage was found in a similar manner to the method used when investigating ZIPP wheels and the Garneau helmet.

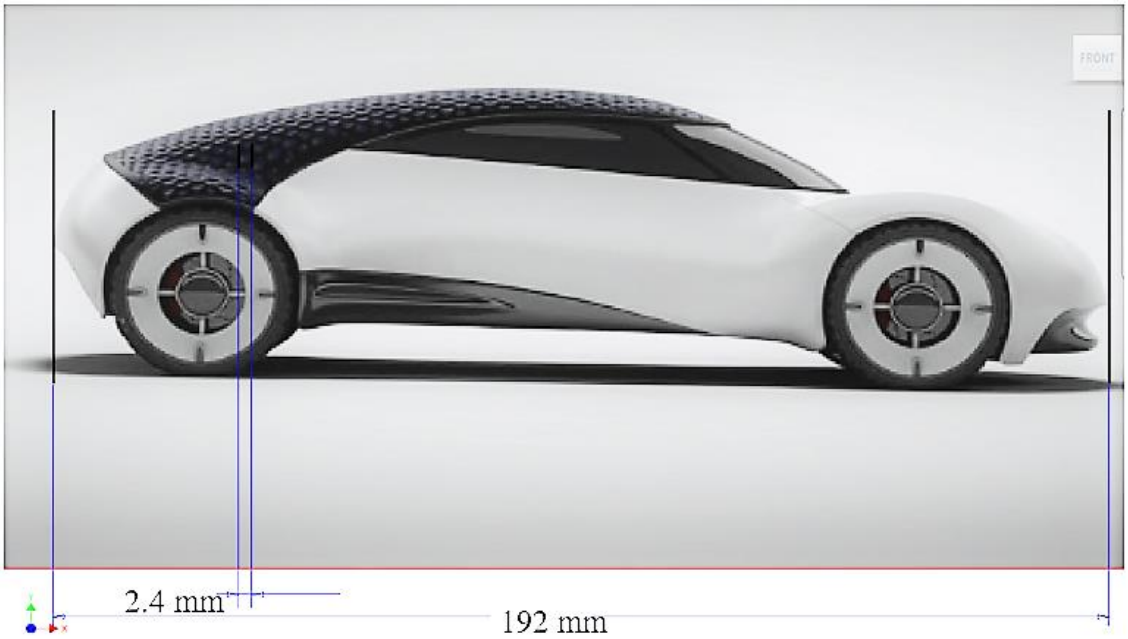

Figure 2-15: Hexa solar car (Bez, 2012).

The dimple to reference length percentages were analysed for sizing trends to allow for a starting point for dimple sizing on high and low curvature surfaces. The results are shown in Appendix A1: Table A-1, with mean diameters of 5.5 mm for low curvature surfaces and 11 mm for high curvature surfaces. This analysis shows the most appropriate sizing that should be used as a guide when designing dimples for application to high curvature and low curvature surfaces. The application of dimples to commercial devices shows a trend in reducing net aerodynamic drag and thus justified the investigation and application to other devices.

2.3.3. Tripwire/s

Two simple definitions may be derived from the term “Tripwire/s.” It is used:

- As a term to define the concept of tripping the airflow from laminar to turbulent earlier than would naturally occur (De Wet, 2013).
- As an actual trip wire utilised in the form of a simple wire placed across a boundary perpendicular to the incoming airflow, and usually placed only near the point of separation or transition, nearer the leading edge than the separation or transition point (De Wet, 2013).

Another form of tripwire known as a vortex generator will be discussed later.

Nieto et al (2008) analysed the airflow over the Messina Strait bridge that was to be optimised via the use of trip wires and/or winglets. The trip wire concerned was a circular tube of 0.4 m diameter which was proposed to fix the separation point of the flow attached to the lower side of the road boxes. The addition of the trip wire did indeed optimise the airflow and reduce separation while increasing the vortex-induced vibrations. The lift coefficient did not suffer important changes while reducing moment coefficient to near zero, which shows that the drag was reduced and thus the separation region also. In order to visualise the trip wires applied, the original design image can be seen in Figure 2-16.

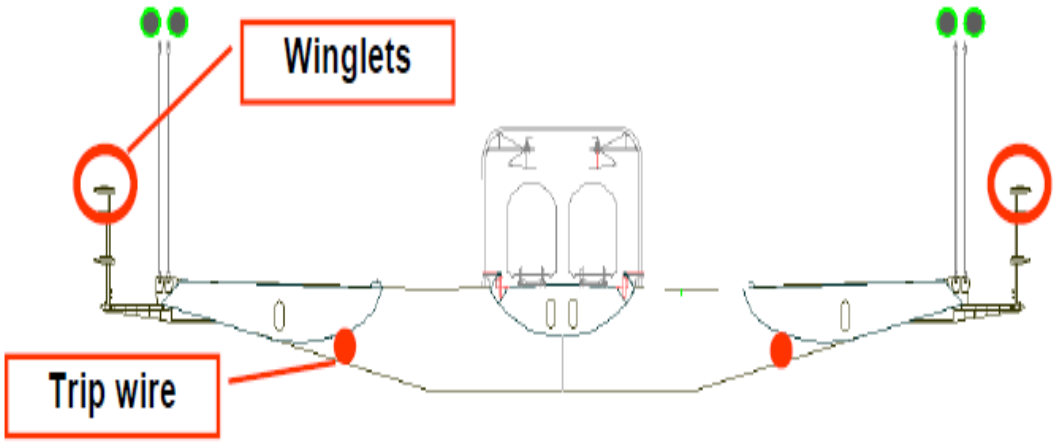

Figure 2-16: Messina Strait Bridge design (Nieto, et al., 2008).

2.3.4. Riblets

Riblets to be used on aerofoils were investigated by Sareen et al (2011), and shown to allow for airflow tripping so that the near wall airflow may be altered. The overall reduction in drag was achieved by decreasing the size of the separation region that results from an adverse pressure gradient. Flow control was attempted by applying V-shaped riblets in the form of tape to reduce drag in wind turbine blade applications. Riblets applied to supercritical aerofoils were investigated by Viswanath (2002), similar to the riblets investigated by Sareen (2011), are shown in Figure 2-17 (Sareen, et al., 2011), (Viswanath, 2002).

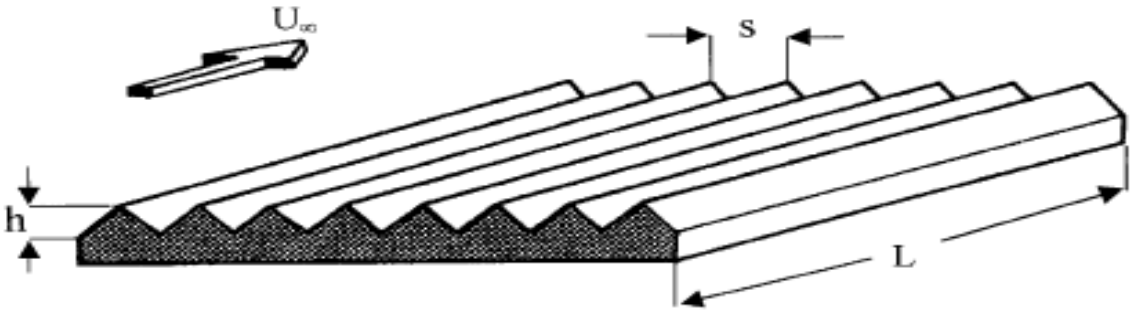

Figure 2-17: Riblets viewed under an electron microscope (Viswanath, 2002).

Sareen et al (2011), conducted tests using chosen aerofoils at angles of attack as well as at different locations of application along with the aerofoil chord length. The results showed that the drag reduction depended on the angle of attack, Reynolds number, riblet size, and location.

An optimal riblet size with its point of application being in the turbulent region was indeed found to reduce drag by up to 5 %. This reduction was achieved by using 152 µm riblets and an aerofoil angle of attack of six degrees. Other configurations proved to increase drag by up to twelve percent (Sareen, et al., 2011).

It was found that riblet effectiveness increases with a decreasing Reynolds number and increasing riblet size. Investigations found that riblet sizing is dependent on the aerofoil used, therefore the only way to find optimal riblet sizing and position would be through testing and analysis. Different riblet shapes could also affect improvement in efficiency in different ways.

Sareen et al (2011), designed riblets to have equal "peak to valley" and "peak to peak" spacing while it was found that a riblet size of 62µm was optimal. Riblet tape was made with "V-shaped riblets" on one side while the other side consisted of an adhesive. The optimal size of riblet would only work to reduce drag at its optimal Reynolds number range, while if not optimal, would increase drag by almost double (Sareen, et al., 2011).

2.3.5. Vortex generators

Vortex generators act as trip wires. They are mainly applied to aerofoils at angles of attack or where separation would have occurred if natural flow progression was allowed. Vortex generators as explained here, are small singular triangular protrusions.

Riblets, as discussed before, are tiny protruding lines of spikes applied in a staggered fashion starting from the optimal point near the aerofoil's leading edge, ahead of separation. Vortex generators are instead applied in a single line at the respective optimal point, investigated in this section.

Aero-Service (2013), found that vortex generators should be placed as recommended for aeroplane use, at 7 % - 9 % of the chord from the leading edge of the aerofoil, as the distance measured to the front of the vortex generator (Skopinski, 2010). The optimal position would need to be determined for the speed range in which the solar car would operate through further research, testing, analysis and verification. Passive and active flow separation control over an NACA0012 aerofoil was investigated by Hua et al (2007). An aerofoil similar to that used for the canopy design applied to the solar vehicle was analysed. An investigation into passive and active vortex generators placed at the point of separation was conducted.

It was discovered that the vortex generators, operating on similar principles as the dimples and trip wires, increased the efficiency (decreased overall drag) of the aerofoil, resulting in an improvement of 80 % when using passive vortex generators, and further increased efficiency with active vortex generators (Skopinski, 2010).

A passive vortex generator is a generator that has its size, position and orientation fixed on the applied surface. This means that there must be an optimal range found for the application, which is limited (Skopinski, 2010).

An active vortex generator is a vortex generator which has its size, position and orientation altered according to different flow conditions. The specifications for the vortex generators used on the NACA 0012 aerofoil of chord length, C, are that it has a radius equivalent to 0.01675 C and a thickness equivalent to 0.001 C. Figure 2-18 shows the placement and sizing of the vortex generators used by Hua et al (2007).

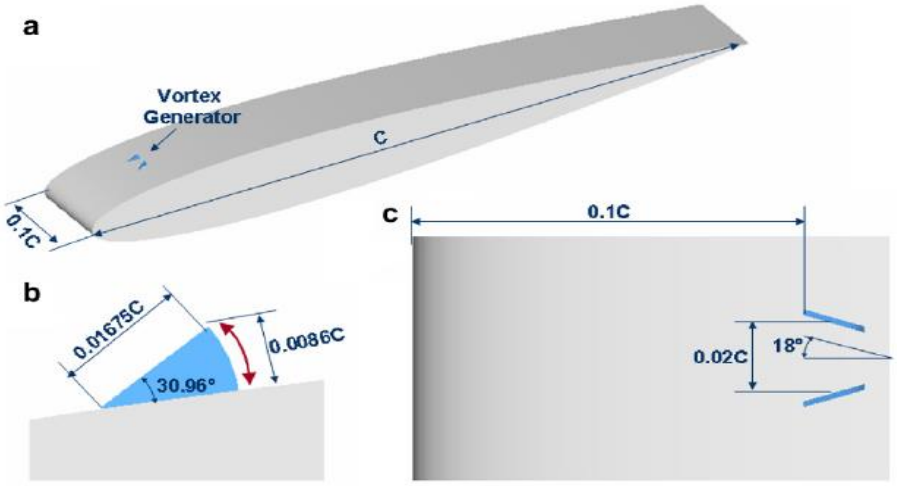

Figure 2-18: Vortex generator specifications by Hua et al (2007).

Investigations into the best type of trip wire or vortex generators used for general application to aerofoils at an angle of attack, were done by Lin (2002). It was realised that normal vortex generators have a height larger than the boundary layer thickness, while low profile vortex generators have a height less than the boundary layer thickness. Low profile vortex generators have an optimal height, h, of 0.1-0.2 multiplied by boundary layer height, δ, and are mostly non-equilaterally triangular shaped. Wishbone vortex generators with a spacing (z) to height (z/h) ratio equivalent to 64.6 provided the best drag reduction of 38% when applied to an aerofoil with an angle of attack. The graph in Figure 2-19 shows that vane type vortex generators with $h/\delta \sim 0.2$ are best at reducing separation over the aerofoil and thus at reducing drag.

Figure 2-19 also shows that riblets do not reduce drag significantly when analysing previous designs (Lin, 2002).

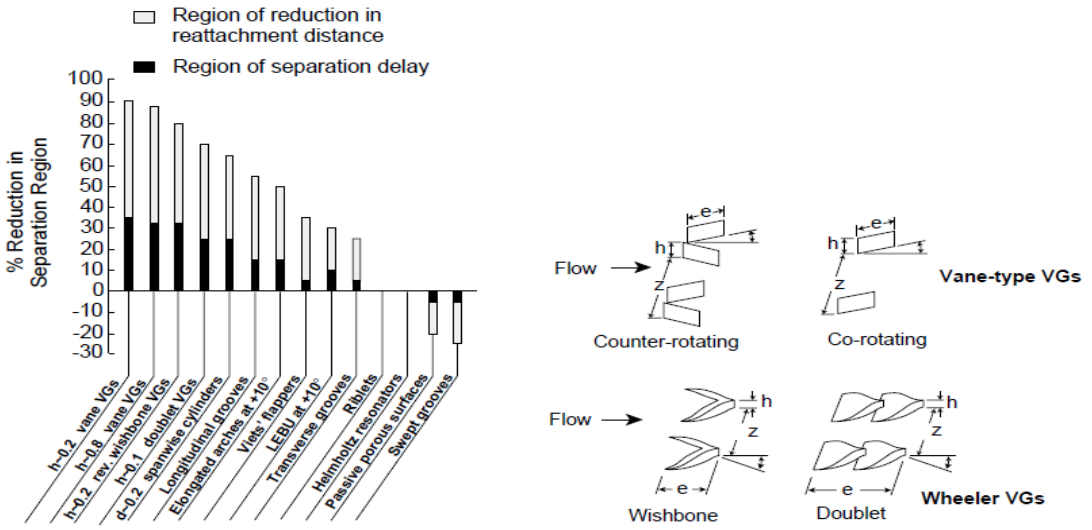

Figure 2-19: Vortex generator types (Lin, 2002).

Lin (2002) stated that tests done by the Defence Evaluation and Research Agency (DERA) showed counter-rotating vortex generators to be the most efficient when used with the following dimensions applied (Lin, 2002):

- h/δ ~ 0.3 with "δ ~ 33 mm."
- e/h ~ 10.
- z/h ~12.
- β ~ 14° - Angle of vortex generators as shown in Figure 2-19.
- Locate vortex generators at 52 h "upstream" from the separation on the un-altered aerofoil and the gap between counter-rotating vortex generators most efficient at 1 h.

As one of the design improvements made to the Boeing 777 series aircraft to save fuel costs, and thereby improve the aerodynamics by decreasing drag, vortex generators were used and thereafter improved. The vortex generators used to reduce drag further are shown in Figure 2-20 (Thomson & Schuize, 2009). Placement of these was not made clear, the methodology for placement was mentioned to be nearer the leading edge than separation point and dependent on the application at hand.

Figure 2-20: Vortex Generator for the Boeing 777 aircraft (Thomson & Schuize, 2009).

2.3.6. Suction

Suction is a technique used to reattach airflow by applying holes to the correct region or flaps that open when needed to create a pressure difference, causing suction of the boundary layer into the aerofoil and keeping the airflow attached. Suction using these techniques is usually used for when an aerofoil is at an angle of attack. In the case of the solar car, crosswinds would mimic an angle of attack. This technique is applied to a portion of the aerofoil just before or after separation occurs, be it at the leading edge or further down the chord (Bakker, 2006). Suction is more effective where there is a higher velocity near an edge where the geometric gradient of that surface is going to change drastically and cause the flow to tend to separate (Othmer, 2014).

2.3.7. Blowing

Blowing is applied through introducing a flow of high momentum near the separation point by adding an airflow device near the wall of the aerofoil. This speeds up the near boundary airflow and in theory re-attaches the fluid to the boundary surface (Bakker, 2006). Blowing is more effective in regions of lower velocity where the air may have separated already after a sharp edge or high geometric gradient change has occurred (Othmer, 2014).

"Overall, the best results are obtained with the single suction jet cases, intermediate results are obtained with the multi jets and the worst results are obtained with the blowing jets" (Gença, et al., 2011). These findings explain how suction was the best technique of the three mentioned, due to its superior performance when applied to a similar application as in the present investigation of a streamlined aerofoil or similarly shaped bodies.

2.3.8. Flow Alteration Surface Deturbulator

Sinha & Ravande (2008), developed a so-called deturbulator which is a flexible composite film developed to stabilise the turbulent or separated flow near the boundary of an object. The device was only effective in a passive manner on surfaces which had a pressure gradient, i.e. separation and/or a cambered aerofoil. A flexible composite surface deturbulator (FCSD), acts to accelerate the flow due to skin friction being reduced by reducing or dissipating the turbulence in the flow in the separated flow area. Figure 2-21 shows the FCSD applied to an aerofoil. The improvements noted for this technique when applied to the NLF-0414F aerofoil, were (Sinha & Ravande, 2006):

- Profile drag (skin friction drag) reduction of up to 60-80 %.
- Pressure drag (frontal area & separation characteristic drag) reduction of up to 45 %.
- Lift coefficient increase of 12 %.

An FCSD device works by creating a virtual wing profile characterised by having a thin region of “dead air” which has a low level of turbulence throughout the chord of the laminar flow aerofoil. This altered flow seems to have a thicker turbulent boundary layer with a thin marginally separated flow region (Sinha & Ravande, 2006).

The developers of the FCSD claim that even with higher levels of turbulence and separation along a longer portion of the chord, having an FCSD stabilises the air flow, and causes less fluid to be attached to the aerofoil surface while mitigating the effects of swirling and unstable flow (Sinha & Ravande, 2006). As a result, the flow on the upper surface is sped up, all of which increases lift and decreases drag on laminar flow aerofoils. Sinha & Ravande (2008), noted that the significant wake region resulting from separation may induce less drag as it acts as a “virtual boat tail extension.” They claimed and have validated their claim, that the FCSD method may thus be applied to bluff bodies. The application of an FCSD to an aircraft wing may allow a fuel saving of up to 10%, while increasing the lift may also yield the possibility of decreasing the complexity of flap structures. An example of the patented design is shown in Figure 2-21.

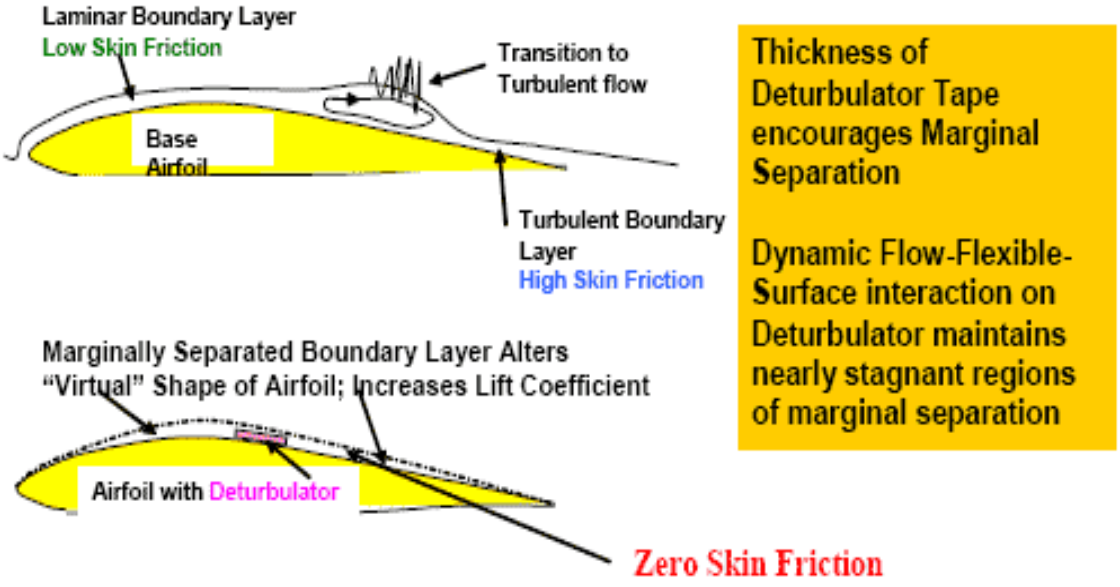

Figure 2-21: FCSD (Sinha & Ravande, 2006).

2.3.9. Acoustic Emission

Yang (2013) developed a mechanism that uses acoustic emission to reduce drag, the principle applied involves the application of internal or external sound waves to an aerofoil surface. These sound waves cause the fluid in contact to become optimised and thus cause the boundary layer to be reattached after separation.

The application frequency for successful flow alteration changes with the angle of attack. The natural frequency for successful acoustic emission application is also affected by Reynolds number. This means that the acoustic emission system/technique would have to be altered according to changes in speed as well as constantly changing crosswind incident angles (angles of attack) (Yang, 2013).

2.3.10. NACA Duct – Ventilation

A NACA duct was proposed for use to ventilate the interior of the solar vehicle as per WSC race regulations. Sizing and position were not of utmost importance due to the time and other constraints placed on the design of the NACA duct, rather the guarantee of sufficient airflow, the amount of which also not specified by the race rules for the WSC (Frick, et al., 1945), (Hall, 1948), (Vale & Ringrow, 2011). This duct allows air flow from the external surface of an object to be redirected into the internals of the object without causing as high a drag addition as would a simple hole or another device.

NACA ducts are commonly used on sports cars and aeroplanes so that cooling air may be redirected into the necessary internals. It was found that the duct inlet sizing should be matched to the required mass flow rate for the application to which the duct is applied (Frick, et al., 1945).

If incorrectly designed, the duct would increase drag without causing air intake as needed. Generally, for most applications, optimal sizing specifications were as follows (Vale & Ringrow, 2011), (Pignier, et al., 2015):

- Width to Depth ratio, (w/d) of 3 – 5.
- Ramp angle, α, of 7 degrees.

Duct length may be chosen according to the following recommendations. The optimum ratio between the flight speed and the flow speed at the inlet is known as the velocity or mass flow ratio. This was found to be optimum at 0.7, meaning that the duct flow speed should be 70 % of the external flow speed/object speed (NASA, 1945), (Owen, 1991). In order to construct an NACA duct accurately for the specific aerofoil shape to which it is applied on the solar vehicle, the duct was modelled from first principles.

2.4. Rolling Resistance in Relation to Aerodynamics

The largest losses inefficient electric vehicle design in highway conditions are rolling resistance and aerodynamic efficiency. Increased mass will increase the rolling resistance.

This increase must be compared with the potential aerodynamic drag reduction to determine whether the application of such a device or flow alteration technique allows for any net increase in vehicle efficiency.

Rolling resistance is calculated via equation 2-25 (CFD Online, 2011), (Fox, et al., 2012).

$$F_{rolling} = W_{car} \times c_{rolling} \quad \text{Equation 2-25}$$

The net gain (positive) or loss (negative) in vehicle efficiency is represented indirectly by equation 2-26 adapted from summing the forces in the direction of motion (Fox, et al., 2012).

$$F_{resultant\ reduction\ in\ total\ drag} = F_{Aerodynamic\ drag\ reduciton} - F_{rolling} \quad \text{Equation 2-26}$$

2.5. Overview of Flow Alteration Devices

In order to analyse the devices mentioned with regards to the application on the solar vehicle the following was noted in Table 2-2:

Table 2-2: Flow alteration devices and application.

TECHNIQUE	SHAPE	PLACEMENT	PLACEMENT AREA ON VEHICLE	IMPORTANT FACTORS
DIMPLE	Rounded Concave	Nearer the leading edge than natural transition	Shrouds; Top shell; Canopy; Entire car surface and/or Wheels (Cyclery, 2007)	Use if separation near trailing edge depending on application type
	Rounded Convex	Nearer the leading edge than natural transition	Shrouds; Top shell; Canopy; Entire car surface and/or Wheels (Cyclery, 2007)	Use if separation near trailing edge depending on application type
	Hexagonal Convex	Nearer the leading edge than natural transition	Shrouds; Top shell; Canopy; Entire car surface and/or Wheels (Cyclery, 2007)	Use if separation near trailing edge depending on application type
	Shallow flat bottomed	Certain patterns over the entire surface	Shrouds; Top shell; Canopy; Entire car surface and/or Wheels (Cyclery, 2007)	Sizing from previous application
		Nearer the leading edge than natural transition		Use if separation near trailing edge depending on application type

TECHNIQUE	SHAPE	PLACEMENT	PLACEMENT AREA ON VEHICLE	IMPORTANT FACTORS
TRIPWIRES	Concave indent	Placed nearer the leading edge than natural transition	Shrouds Top shell Canopy Use if large amount of separation due to crosswinds	Use if separation near trailing edge depending on application type
	Convex protrusion	Nearer the leading edge than natural transition	Shrouds; Top shell; Canopy; Use if large amount of separation due to crosswinds	Use if separation near trailing edge depending on application type
	Dimple shape	Nearer the leading edge than natural transition	Shrouds; Top shell; Canopy; Use if large amount of separation due to crosswinds	Use if separation near trailing edge depending on application type
RIBLETS	V-Shaped	Near separation point	Shrouds; Top shell; Canopy	Use if separation near trailing edge depending on application type
	Surface Roughening	Entire surface; Nearer the leading edge than natural transition	Shrouds; Top shell; Canopy	Use if separation near trailing edge depending on application type
VORTEX GENERATORS	Retractable V-Shaped	Nearer the leading edge than natural transition	Shrouds; Top shell; Canopy	Use if separation near trailing edge depending on application type

TECHNIQUE	SHAPE	PLACEMENT	PLACEMENT AREA ON VEHICLE	IMPORTANT FACTORS
	Low Profile V-shaped	Nearer the leading edge than natural transition	Shrouds; Top shell; Canopy	Preferably use Counter-rotating vane type vortex generators placed at 52h upstream from the separation point and use the given illustrations in the text to allow for $h/\delta = 0.2$. Crosswinds of major concern for placement.
SUCTION	Holes	After separation; further from leading edge than natural transition	Shrouds; Canopy	
	Slit	After separation; further from leading edge than natural transition	Shrouds; Top shell; Canopy	Suction devices will have to be applied, not all able to be tested via computational methods. In CFD modelling a velocity inlet boundary would be used to mimic suction, be it holes or flaps
BLOWING	Nozzles	Just after separation	Shrouds; Top shell; Canopy	
		Further from the leading edge than natural transition	Shrouds; Top shell; Canopy	Similar to suction
FCSD		Entire surface	Top shell; Shrouds	Applied and tested, not designed by the author
ACOUSTIC EMISSION	Sound emitting device	Entire surface internally	Shrouds; Top shell; Canopy	Spatial constraints internally would also hamper the ability to apply this technique

2.6. Summary of Literature Review

When altering the boundary layer airflow, transition and separation characteristics are usually changed as a result. If done using the correct methods as investigated, a turbulent boundary layer may delay separation from occurring as close to the leading edge as would naturally occur. This theoretically reduces drag drastically in many cases, though a now more turbulent boundary layer increases viscous drag when compared to the laminar boundary layer. The overall drag reduction may result from separation causing negative (opposite direction to object movement) pressure forces, which in most cases is greater than viscous forces, therefore less drag results if the separation region is reduced even though viscous drag is increased. Overall drag reduction in this manner is applicable for direct airflow or airflow at an angle to the object (crosswinds).

It was determined that dimples may be adapted in several ways to be used in similar ways to the applications of trip wires and vortex generators, though their effectiveness as such may be questionable. Dimples potentially allow for drag reduction if applied to the wheels and the canopy due to high curvature.

Riblets as a concept would not have been as effective as vortex generators and were discarded as a potential flow alteration device for use on the solar vehicle. Investigation of the aerodynamic performance gain from riblet application was found to be less than with vortex generators applied to similar shapes such as aerofoils.

Vortex generators were found to be effective at useful (a wide range) angles of attack which is similar to when crosswinds are in effect, which is usually the case with a solar vehicle. The best vortex generators were found to be the wishbone type placed 5-30h forward from separation point and with a spacing to height ratio of 64.6: 1.

The greatest problem with using suction would be having to apply a suction device; a pump of some sort if applied in the same way as many of the other devices previously discussed. This technique may have been implemented by adding holes in certain places on an aerofoil so that the pressure difference would cause suction of the air into the aerofoil and thus force the boundary layer to stay attached. This, however, may have had an adverse effect on the structural rigidity of the car through stress concentrations caused by the holes. Suction has the potential for more substantial drag reduction than blowing, or both combined. However, the method of application would not be efficient if drawing vitally important power from the batteries. The only application in the form of holes working via pressure differentials could be considered.

An FCSD would allow for a high amount of drag reduction, however, testing, manufacturing and time limitations did not allow for the application of this technique. The purchase of this device would be the best option if other devices did not work.

Acoustic emission would require a power source which is likely to be undesirable due to the power being needed for propulsion. It would be considered if and only if it caused significant drag reduction on the aerofoil resulting in a net gain in efficiency when considering the power input from the power source to the acoustic emission device. This would be a complicated task and only attempted if absolutely necessary, in other words, if other methods did not succeed. The technique would also have been far too complex to use and because of the power needed to run the acoustic emission devices, it may have yielded a negative net efficiency though yielding similar aerodynamic drag reduction to other methods.

In order to allow for an accurate modelling of the airflow, simulations incorporating the standard head-on airflow as well as simulations with crosswinds applied would be conducted while including airflow alteration device. Real geographical and seasonal average wind speed and direction data were to be used. For the SASC, data available from Sauran.net (2013), for regions near the race route from Pretoria to Cape Town, would be used (Sauran, 2013). This data applies inlet conditions for CFD analysis and can be found in Appendix A6: Table A-12. Crosswind characteristics may be applied through knowing average crosswind data so that the testing would not be region specific. The crosswind data from Darwin to Adelaide for the month of October was found for analysis of winds during the WSC (Coppin, et al., 2003). Inlet conditions would then be modified to accommodate for this if any real efficiency gain was found.

2.7. Literature Review Conclusion

Various mechanisms are capable of improving aerodynamics by tripping airflow from laminar to turbulent before transition naturally occurs. Further investigation of flow characteristics, specifically transition and separation characteristics, was essential in order to select the most viable flow alteration technique. Testing and analysis match flow characteristics to the characteristics of the flow altering device, and thereafter one was chosen and used for further study. Previous knowledge of testing and analysis using CFD testing of the solar vehicle aided investigations in this selection process.

A preliminary investigation into the most viable technique to be used showed that only the use of dimples and vortex generators was possible within the manufacturing and time constraints. The most viable application areas chosen were therefore the canopy and wheels.

Many potentially applicable devices were considered aside from the original idea of using the same concept used on golf balls and/or wings to delay the separation region.

The techniques considered are shown in Table 2-3, highlighted in green:

Table 2-3: Alteration technique selection.

Flow Alteration Technique	Past Application Success (Bluff Bodies) [Weighting: 25%]	Past Application Success (Streamlined Bodies) [Weighting: 100%]	Predicted Usefullness [Weighting: 20%]	Feasibility
Dimple	10	7	10	11.5
Trip Wire	6	7	10	10.5
Riblet	8	8	7	11.4
Vortex Generator	9	9	9	13.05
Suction	0	8	9	9.8
Blowing	0	7	7	8.4
FCSD	7	9	10	*12.75*
Acoustic Emission	0	8	10	10

Through considerations pertaining to curvature and feasibility analysis, the most viable areas for successful application of flow alteration devices are the:

- Wheels: highly turbulent zone due to spokes.
- Canopy: high curvature.

Finally, vortex generators and dimples were only considered for application to the UKZN solar vehicle and covering areas of high turbulence such as the area of wheel protruding beneath the shroud.

CHAPTER THREE: ANALYSIS AND DESIGN

3.1. Overview

The process used for selecting the most viable airflow alteration device/s for the solar vehicle in question is described here followed by the details of the design and testing thereof.

The process began with the hypothesis that the aerodynamics of the solar vehicle may be improved without modifying its bulk geometry. The car was geometrically analysed for high curvature regions and potential high turbulence zones, aided by knowledge gained from investigating the relevant literature. Testing done on the solar vehicle itself aided in the analysis of the vehicle while allowing for insight to be gained into which devices are applicable for aerodynamic optimisations to be realised. The effects of curvature and speed on flow characteristics were analysed in Section 2.1. Race data pertaining to wind conditions was analysed for the SASC and WSC so that the CFD models were set-up accurately. The most applicable devices were selected based on the literature and previous applications thereof, and application areas were decided upon. The selected devices were dimples and vortex generators. In order to accurately capture the fine CAD details to be used in the designs, it would be preferable to use a polyhedral mesh type in all volume meshed CFD models (CD-Adapco, 2014), (Fox, et al., 2012).

Using the literature outlined in Chapter 2 as reference points, as well as the CFD analysis outlined in Chapters 3 and 4, dimples and vortex generators were then designed. Manufacturing and time considerations did not, however, allow for dimple testing on the canopy. Multiple iterations of flow alteration devices were tested, and if any proved to increase the aerodynamic efficiency of the solar vehicle, further investigation and optimisation of the device was performed. If efficiency was shown to increase, the device was manufactured and implemented.

An efficient way to design the most optimised airflow alteration devices for use on the solar vehicle was to have a detailed design process as illustrated in Figure 3-1 and explained in Chapter 3. This process allowed for a reduction in the lead time for which designs were passed or failed and allowed effective and efficient selection of which devices were finally manufactured for use on the solar vehicle. The design process shown illustrates processes applied to wheel optimisation on the left and canopy optimisation on the right with common links between the two. When stating that literature review sources were used in Figure 3-1, the sources used for dimple testing were taken from Section 2.3.1 while for the vortex generator design and canopy testing, Section 2.3.5 was used for reference. The methodology used to test the devices was adapted from methods used previously by the authors cited in Chapter 2. Figure 3-1 may be seen on the page to follow.

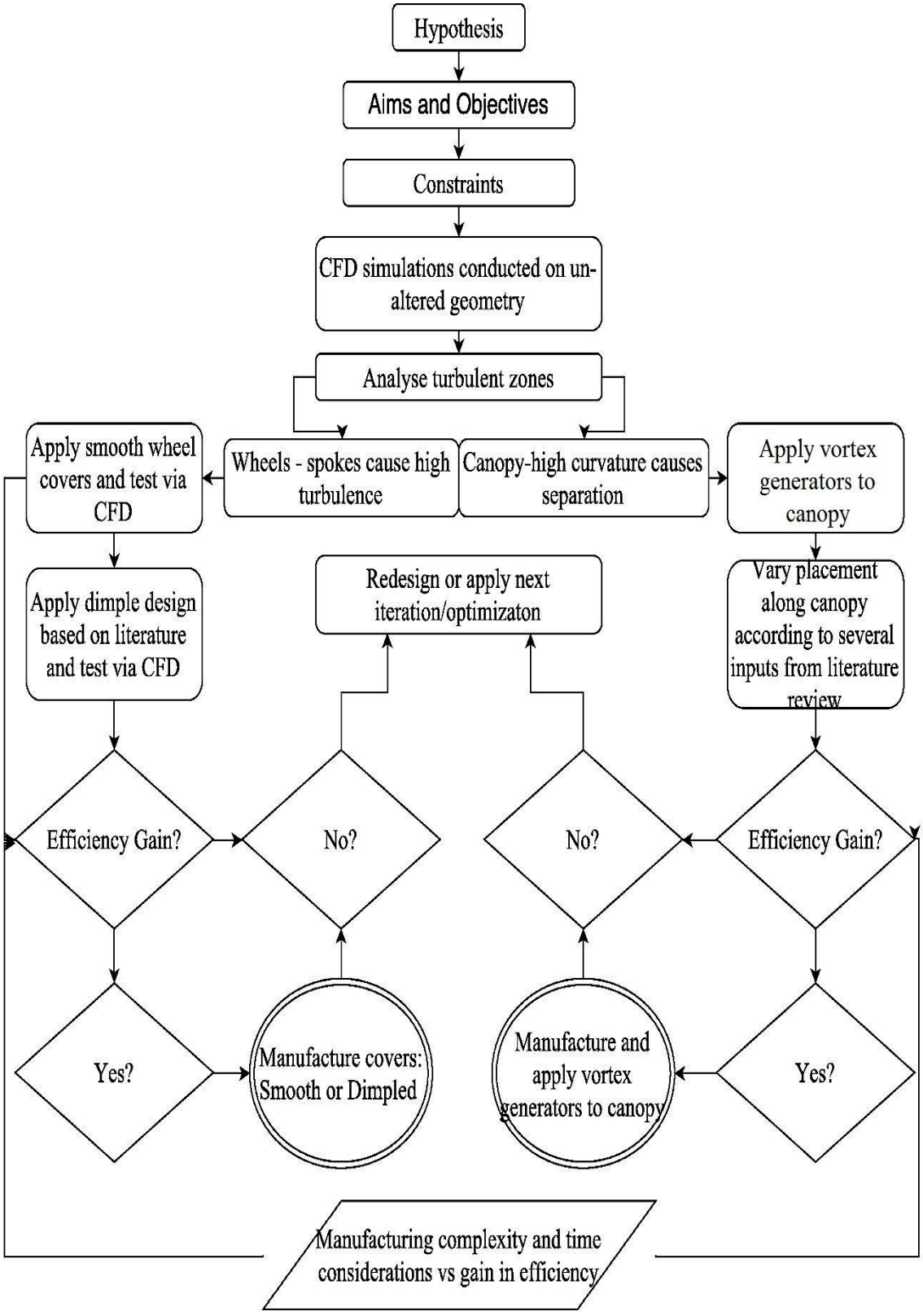

Figure 3-1: Design methodology.

3.2. Wheel Optimisation Devices

This section describes flow alteration devices as applied to the wheels, the geometry preparation thereof, and the CFD concepts used for computational testing. Preparation of the geometry tested is essential when conducting CFD.

Sizing of dimple geometry was found through inspection of ZIPP wheels (Cyclery, 2007), Garneau helmets (Garneau, et al., 2009), and the HEXA solar car project (Bez, 2012). This was done by comparing the dimple diameters as a percentage of the length of the body in question which gave an initial value for the sizing according to the chord length of the potential surface of application. This method was used for preliminary dimple sizing and was only used as the surfaces used for comparison were assumed to have effective application of the dimples, namely Zipp Wheels, Hexa Solar Car and Garneau helmets. Table A-1 in Appendix A outlines the investigation and suggests that the approximate optimal dimple diameter was 5.5 mm for low curvature surfaces and 11 mm for high curvature surfaces similar to that of the outer and inner wheel covers respectively.

The geometry was modelled and altered, and then analysed for errors in meshing and unnecessary complexity so that a STAR-CCM+ built in meshing tool could accurately discretise the fluid volume tested through accurate meshing. The following basic geometry preparation steps were essential (CD-Adapco, 2014), (De Wet, 2013), (Bakker, 2006):

- Check for unnecessary sharp edges and small gaps between surfaces.
- Prepare the fluid volume box to serve as the virtual wind tunnel as follows (Ahmed & Chacko, 2012):
    - Five times the length of the object in question, behind the objects trailing edge,
    - Three times its length in front of its leading edge,
    - Three times its width next to it.

If larger, the results would become more accurate for external aerodynamic testing. The blockage effect would be avoided using the dimensions mentioned here.

3.2.1. Dimples as Aerodynamic Wheel Optimisation Devices

This Section describes the CAD models that were used for patterning dimples onto the surface of the wheel covers. The dimple shape was drawn to the determined dimensions derived from the methods and sizing discussed in Section 2.3.1; the detailed dimple measurements may be found in Appendix A-1: Table A-1. The spacing along the circumference and number of dimples applied is shown in Appendix A-1: Table A-2. The high curvature surface is the surface on the lower section (inner part of the wheel) of Figure 3-2 while the low curvature surface is seen on the upper section (outer part of the wheel).

Figure 3-2 shows the sketch used for revolution of the base of the CAD model for the wheel geometry:

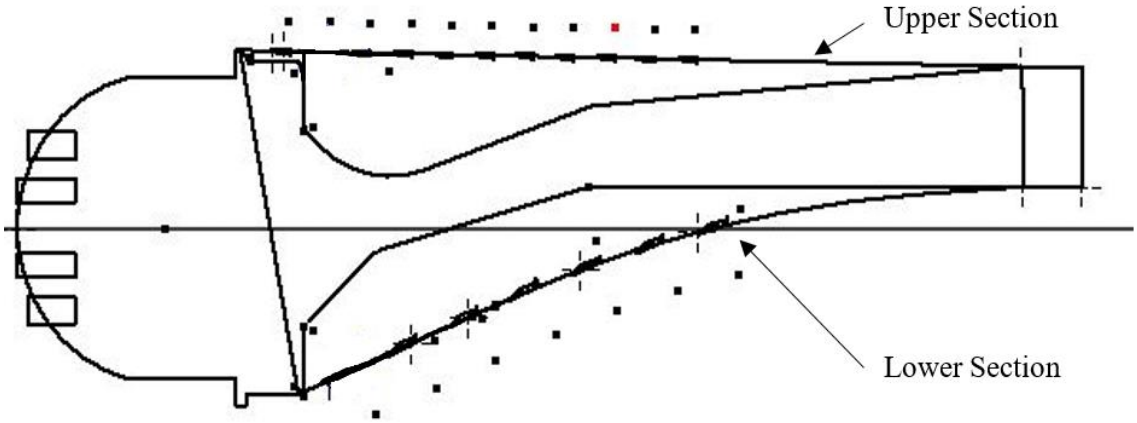

Figure 3-2: Low curvature dimple on the wheel.

Dimple geometry as applied to the low curvature surfaces such as the outer surface of the wheel is shown in Figure 3-3:

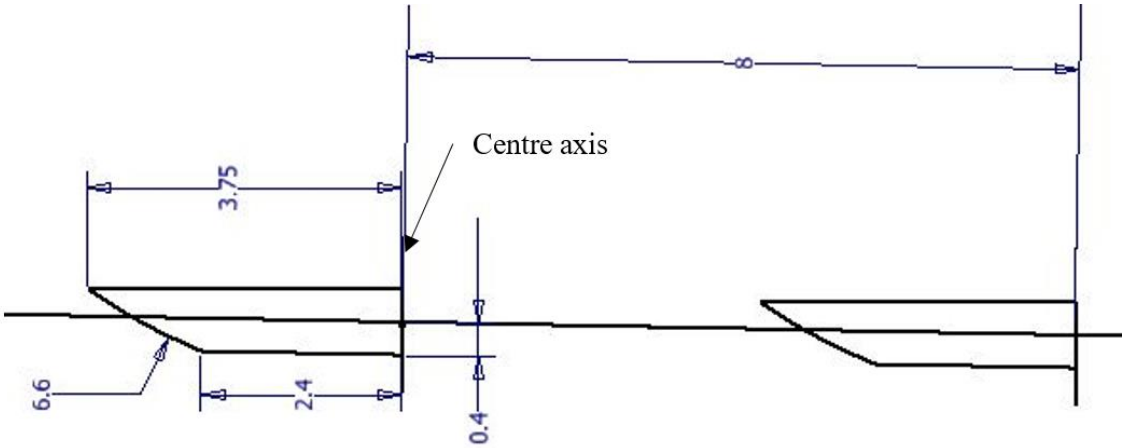

Figure 3-3: Low curvature dimple.

Each half-dimple was revolved about its centre axis, cutting away at the smooth wheel cover resulting in flat-bottomed dimples.

This shape was then patterned across the surface using a circular pattern along a straight line from the inner dimple towards the outer circumference of the wheel cover itself. This was to allow for patterning of the required number of dimples along each different circumference as shown in Appendix A1: Table A-1 and A-2.

Dimple geometry as applied to a high curvature surface is shown in Figure 3-4:

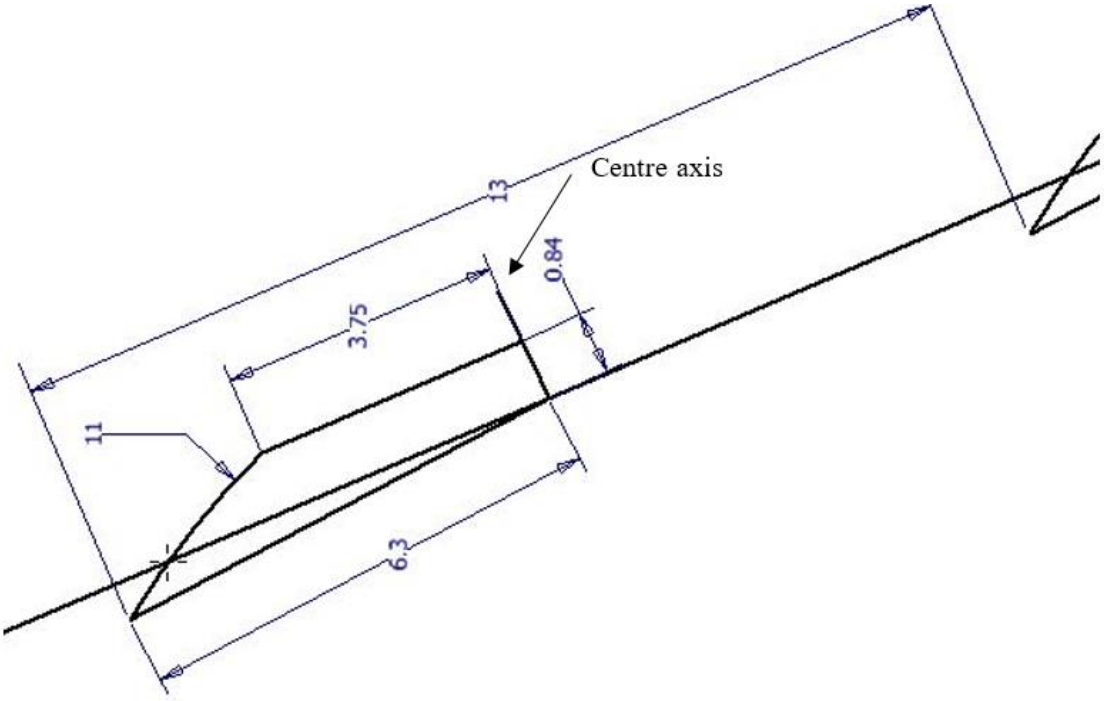

Figure 3-4: High curvature dimple geometry.

The sketch was copied along the wheel cover sketch profile keeping the correct spacing and allowing for each individual dimple to be cut from the inner smooth cover surface. Thereafter they were patterned along each circumference as mentioned, for low curvature dimples. All the dimples were modelled in a similar fashion.

Conceptual Designs

Conceptual designs were chosen with a view to allow for maximum mitigation of turbulence caused by the wheel spokes. Assumptions based on wake formation under the shroud as well as sweeping of air into the shroud were made here, but only verified once basic CFD was conducted. Turbulence and several other negative characteristics result from this slight wake region under the shroud as well as sweeping of air into the interior of the shroud. Concepts allowed for ease of manufacture while keeping removability for race conditions if needed. Wheel covers were tested and investigated for mitigation of bulk turbulence and sweeping of air into the shroud interior caused by the spokes.

Concept 1 – No dimples (i.e. smooth)

Concept one is the application of smooth wheel covers that only mitigate the turbulence caused by the wheel spokes.

Concept 2 – Coarse dimples

Conceptual design two incorporates dimples a factor of 5 larger than the finest dimples tested, based on those found in the literature. This is the coarse geometry model in order to optimise meshing and modelling prior to testing fine dimple details, hence resulting in accurate final models.

Concept 3 – Researched/Refined dimples

Conceptual design three consists of the dimples sized according to golf ball dimple sizes as well as optimal sizing as described in Section 2.3.1.

Concept 4 – Deeper researched dimples

Conceptual design four incorporates dimples 75% deeper than concept three as an outlier test of the data to investigate the importance of the sizing of the dimples set out in the literature. Deeper dimples may alter the airflow more substantially and further reduce drag.

Concept 5 – Shallower researched dimples

Conceptual design five incorporates dimples 25% shallower than concept three, chosen because a depth of half the original would cause unnecessary inaccuracy in the models requiring substantially more cells and resources than are justified, rather than only using 25% shallower size dimples. Computational resources did not allow for shallower dimples to be tested as accurately as desired because a large number of cells would be required to capture the fine geometry details in CFD testing. Shallower dimples may alter the airflow less substantially and further reduce drag.

Concept 6 – Convex outer cover

Conceptual design six incorporates the outer cover having a slightly convex shape which would essentially emulate the wheel having a shroud type shape attached to mitigate the effects resulting from the small area protruding beneath the bottom of the shroud. A truly convex outer cover would hinder mechanical systems such as steering and suspension. For this reason, it was not tested but merely included here as a concept.

Concept 7 – Outer side covered only

Conceptual design seven incorporates having only the outer side covered as the inner side has spokes recessed, meaning that the frontal area of the wheel covers the inner part of the wheel. The spokes frontal area would be covered and thus the spokes on the outer side, which protrude slightly, may alter the airflow more significantly. Concepts were selected for use by considering ease of manufacture, manufacturing time, manufacturing cost, ease of application, aerodynamic efficiency gain (drag reduction), and computational resource use. Preliminary testing conducted allowed for assumptions made to be verified so that further testing could commence.

3.2.2. Wheel Model Set-Up for CFD

In order to accurately conduct a comparison between different wheel cover geometries, a basic control model for wheel testing simulations was set-up to capture the required detail only. This enabled geometric modification effects to be assessed on the wheel as well as the effect on the overall car aerodynamics. Simplification comprised using only one wheel and the associated relevant portion of the solar car wheel shroud. Simulation time and thus the design process was reduced while not significantly compromising accuracy where needed. The boundary conditions used are described in this section while meshing and physics details are described in Section 3.5.

Wheel Testing Fluid Domain

The fluid domain was constructed such that a somewhat simplified version of the interior of the shroud was captured while allowing for the external interaction of the air on the shroud to be modelled. The simplified fluid domain comprises the front section of one wheel shroud with the front right wheel within. This allowed for analyses of airflow around the rotating wheel, the manner in which air is swept into the shroud, and pressure fluctuations. The fluid domain was thus kept optimal for comparison while iterating the design with reduced geometric complexity. This simplified wheel cover testing fluid domain is shown in Figure 3-5.

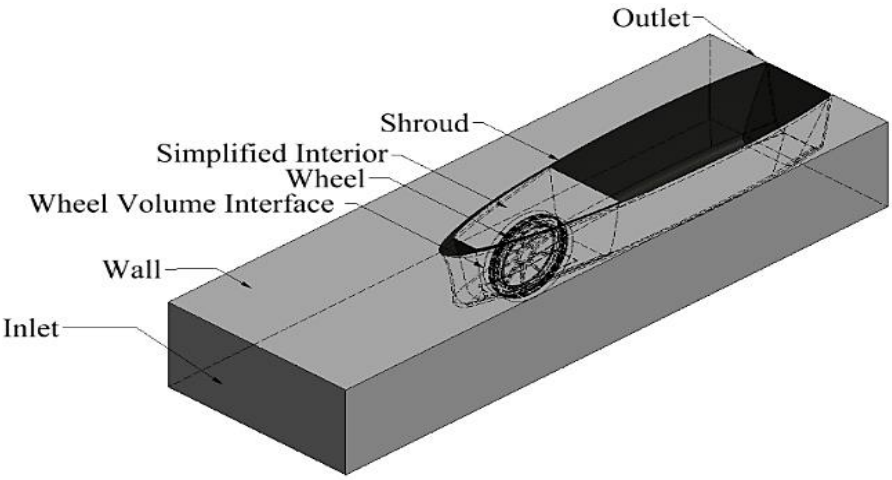

Figure 3-5: Wheel testing fluid domain.

Preliminary tests regarding swirling and turbulence testing were conducted using the smaller fluid domains. Time constraints for manufacture due to the aforementioned races (SASC & WSC) made it imperative that the design verification was completed quickly. The smooth wheel covers were manufactured as they were found to be suitable to allow for at least a slight reduction in overall vehicle drag based on the preliminary testing. Testing of dimples was, for the most part, only investigated as a first research step on their potential; the manufacturing thereof was constrained by factors such as time and cost.

Fluid domain boundaries mentioned for the smaller fluid domain are shown in Figure 3-6.

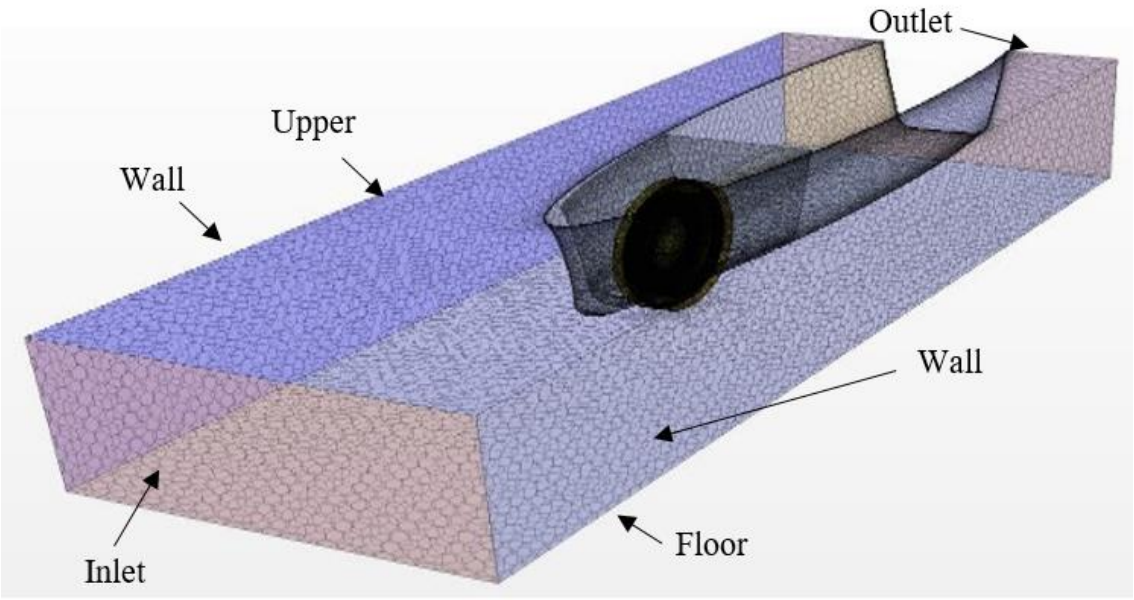

Figure 3-6: Wheel testing fluid domain – Boundaries.

The volume encapsulating the wheel and the cylindrical void was set as an interface with a separate coordinate system assigned at the centre of the wheel allowing for rotational speed to be set accordingly using a rotating reference frame. The inlet was set as a velocity inlet while a pressure outlet was used. The inlet velocity was set to emulate a forward speed of, initially, 70 kph, and later other speeds used for testing. The walls were set as symmetry planes as well as having their prism layers disabled which emulate there being essentially no wall present with respect to skin friction (De Wet, 2013), (Kuzman, 2016).

The height of the fluid domain was kept at the same height as the lower side of the top shell to capture the effects. The upper surface was not shaped similarly to the underside of the top shell due to being only on one side of the shroud. This would also cause inaccuracy if the entire top surface of the fluid domain was kept curved as is the top shell. Uncertainties in the results may have resulted from this methodology but having the refined wheel testing model conducted would allow further comparison. The effects of the wheel beneath the shroud were assumed to be similar with a lower upper surface or a higher upper surface for comparison of the wheel turbulence and separation effects.

The floor, shroud, upper surface, wheel, wheel cover and interior were kept as walls with boundary layer formation enabled, each with its own prism layer and surface cell size definition to mitigate the effects of such a small fluid domain as in the preliminary testing of the application of the wheel covers. The refined fluid domain used is shown in Figure 3-7.

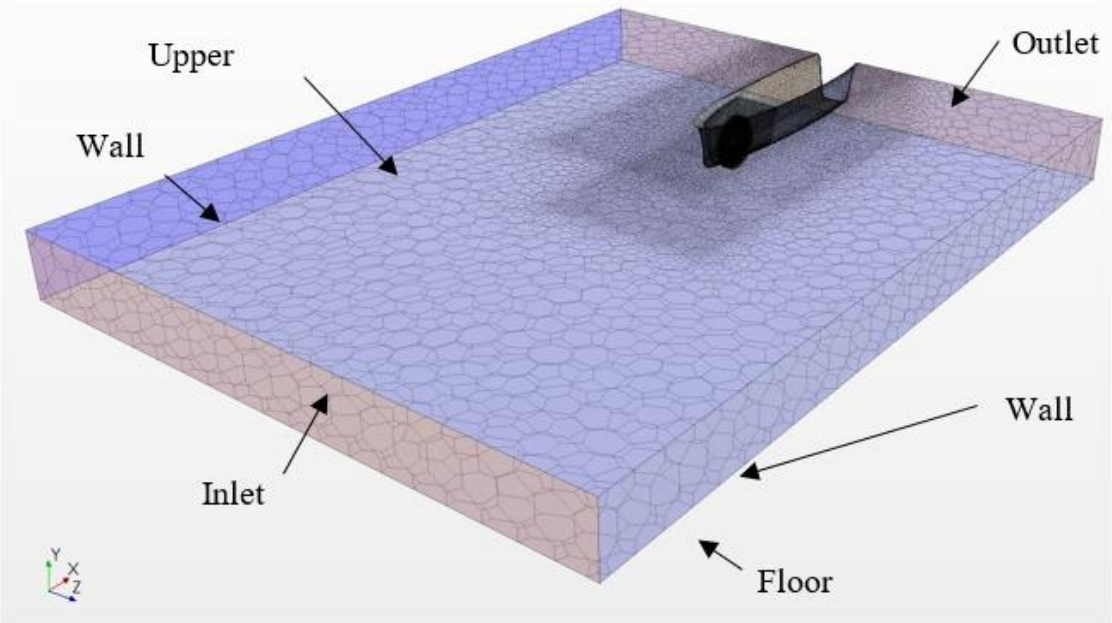

Figure 3-7: Wheel testing refined fluid domain – Boundaries.

Rotating regions were set up in the following manner when analysing the CFD models taking the wheel rotating region into account. The wheels were set to rotate, of several methods available, according to the method used is explained in Figures 3-8. The preparation of the fluid domain using CAD for input into STAR-CCM+ is described.

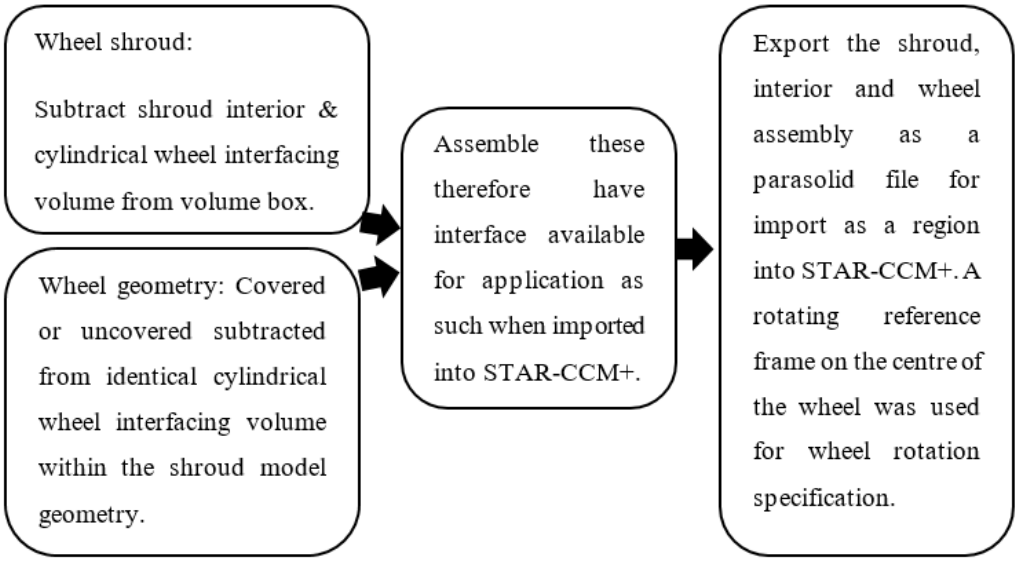

Figure 3-8: Wheel geometry preparation and CFD testing methodology.

Wheel Testing with and without Covers

The CFD testing of the wheels with the applied covers being smooth or dimpled is shown in Figure 3-9.

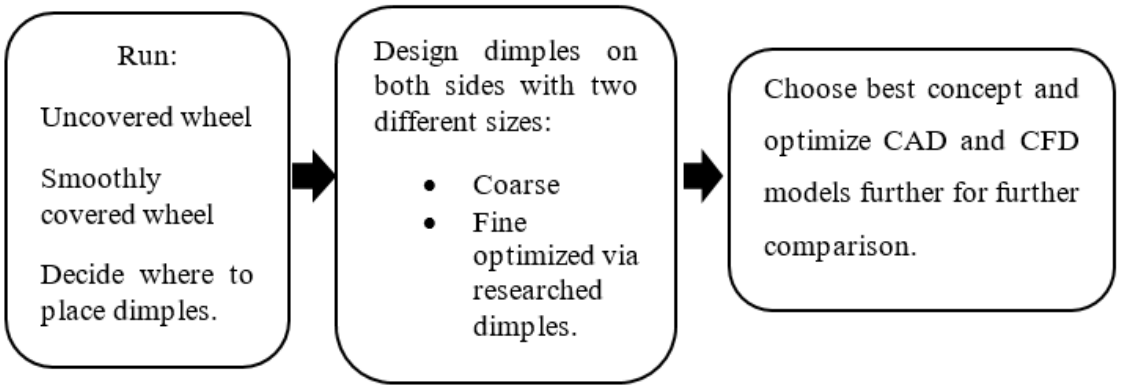

Figure 3-9: Dimple testing.

When deciding where to place dimples, the testing of smooth wheel covers would give insight into placement areas and based on literature in Section 2.3.1 the placement area would be investigated and the dimples applied accordingly.

3.3. Canopy Optimisation Devices

Chapter 2 outlined the possible devices which may be used for boundary layer flow alteration to reduce drag. It was decided based on findings reviewed in Section 2.7 that the most appropriate choice for optimising the canopy aerodynamics would be vortex generators. Vortex generators were chosen because of the high curvature of the canopy, ease of manufacture and ease of application to the outer surface of the canopy. Manufacturing dimples or other devices were considered in terms of time as well as resources. The ability to manufacture devices such as dimples or other devices discussed in Chapter 2, required the canopy itself to be manufactured with dimples imprinted in the mould which was not feasible because of the costs and time involved in the procedure at the time. Several shapes could have been investigated but the ones analysed here were considered sufficient for testing and analysis.

3.3.1. Vortex Generators

Three application method concepts for vortex generators were followed by the placement and modelling of the chosen designs. The placement depends on the point of separation found through further iterations of the design incorporating standard vortex generator placement according to optimal dimensions outlined in Chapter 2, Section 2.3.5.

The triangular vortex generator is shown in Figure 3-10, drawn by simply having two 3-D triangular protrusions assembled on the canopy for a flush fit on the curvature; thereafter the geometry would be extracted for manufacturing if proved effective.

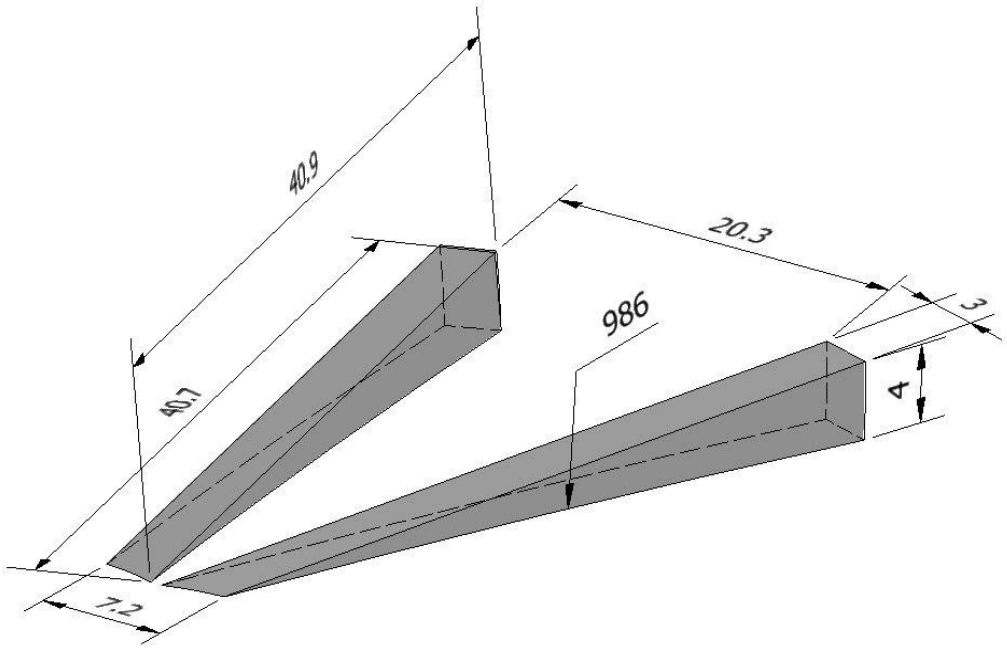

Figure 3-10: Vortex generator geometry.

3.3.2. Vortex Generator Geometry

The vortex generators were modelled according to standards commonly used on aerofoils. A combination of the vortex generator modelling dimensional details may be found in Chapter 2, Section 2.3.5.

Concept one - Straight in-flow

Conceptual design one incorporates the vortex generators having a zero angle of attack with regards to the flow direction - which was discarded as it has already been found that in general, vortex generator design is more efficient when V-shaped generators of specific dimensions are used.

Concept two – Further from canopy leading edge

The placement of the vortex generators is essential for any efficiency gain to be achieved. This design has vortex generators placed at a further distance from the leading edge (when compared to concept three) taking into account basic rules when applied to aerofoils, for example, placing the vortex generator 50 h forward from separation point, where h is described in Section 2.3.5. This placement shows the vortex generators quite far back which does not agree with common views of vortex generator placement in the literature as discussed in Chapter 2.

Concept three – Closer to canopy leading edge

The vortex generators were placed at the section nearer the leading edge of the canopy where the curvature of the canopy increases dramatically. Figure 3-11 illustrates vortex generator concept three positioning on the canopy as well as the nomenclature for all three concepts.

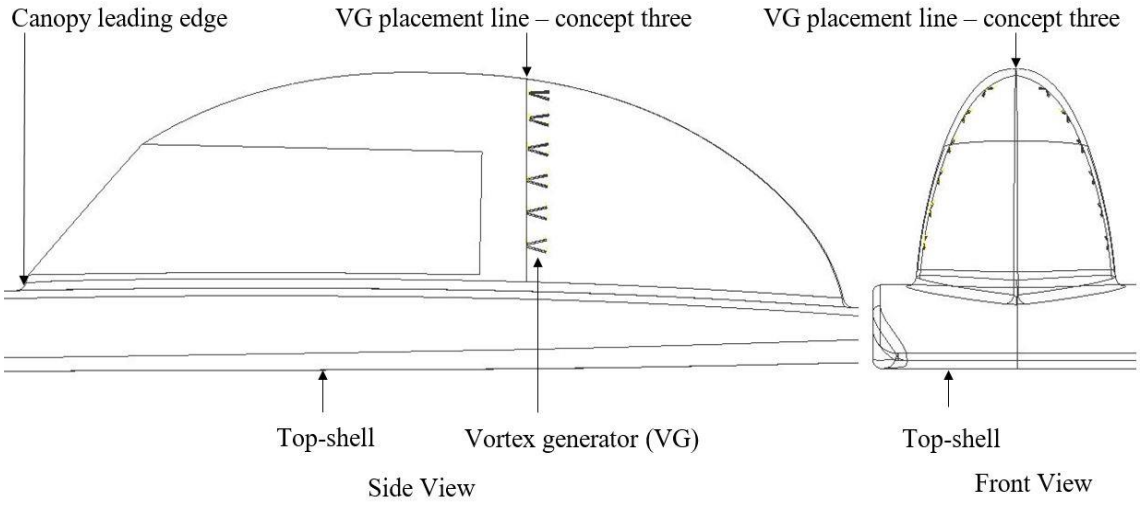

Figure 3-11: Canopy and vortex generator placement views.

Figure 3-12 illustrates the third conceptual design applied to the canopy. The grey area does not indicate a split in the canopy but is merely used to illustrate the area affected by the vortex generators.

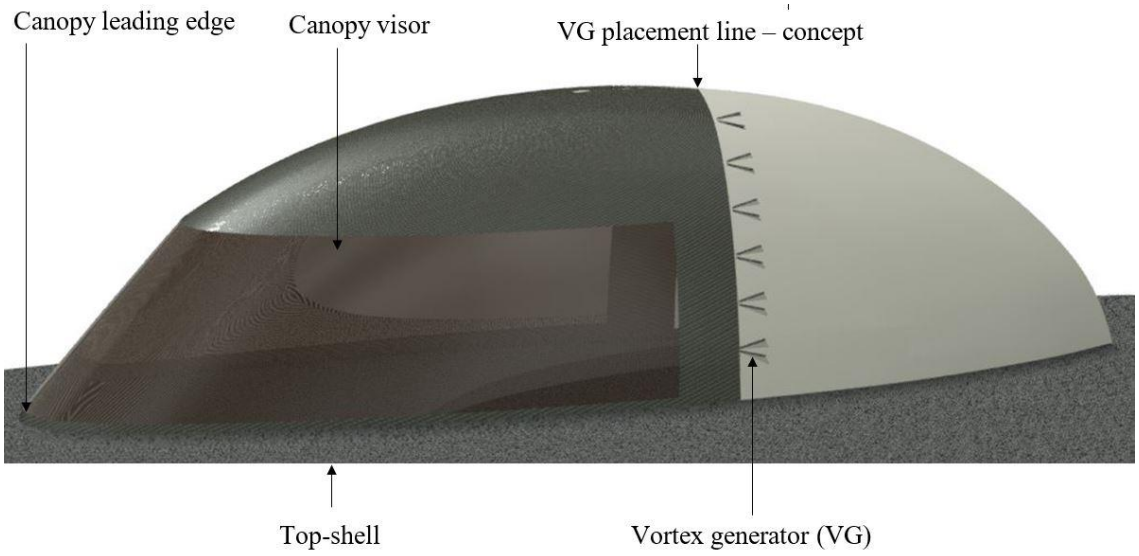

Figure 3-12: Canopy and vortex generator placement.

3.3.3. Canopy Model Set-up

In order to test the effects of adding vortex generators to the canopy, two CFD models were used; one which encompasses the entire car, and the other only the canopy and top shell.

These CFD models were to be compared and it was determined whether similar observations were made. The entire car model would undoubtedly prove to be demanding on computing resources readily available. This meant that two canopy models were used, one for comparing these initial concepts, and the simplified version for comparison of further refined conceptual designs. Front and side views of the full car model can be seen in Figure 3-13 incorporating the entire solar vehicle with simplified interior and rotating wheels. The walls and roof were set as symmetry planes with no prism layers applied while the floor and solar vehicle were set as walls with individual prism and base mesh details applied.

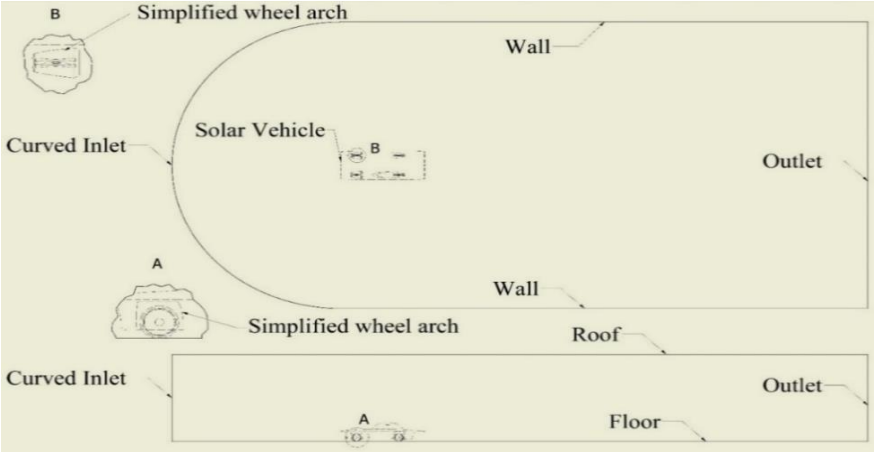

Figure 3-13: Full canopy model.

A simplified version of the fluid domain tested is shown in Figure 3-14 which incorporates only the top shell and canopy showing top and side views of the fluid domain tested. This was used for testing further conceptual designs after it was verified that results did not substantially diverge from those of the full model.

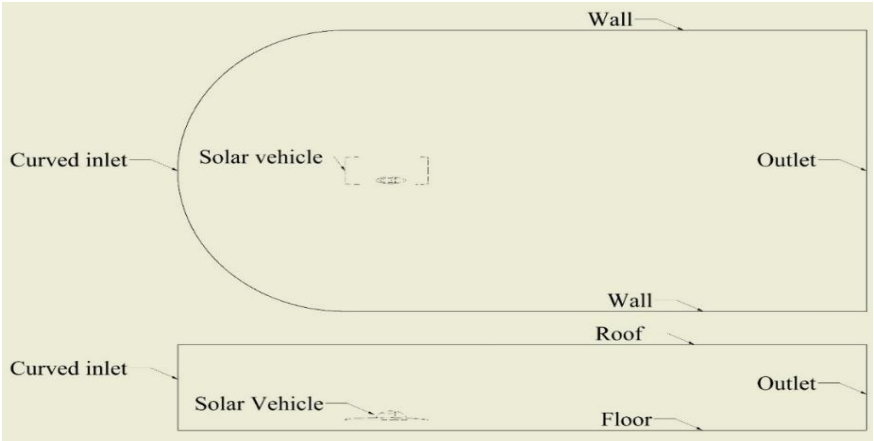

Figure 3-14: Simplified canopy model.

Canopy Model Testing and Comparison

Figure 3-15 shows the testing process for the canopy with/out vortex generators. The wheel interface and fluid domain were set up with boundary conditions similar to that of the wheel cover simulations where, instead of subtracting the wheel shroud from the fluid domain, the entire car is subtracted from a larger fluid domain.

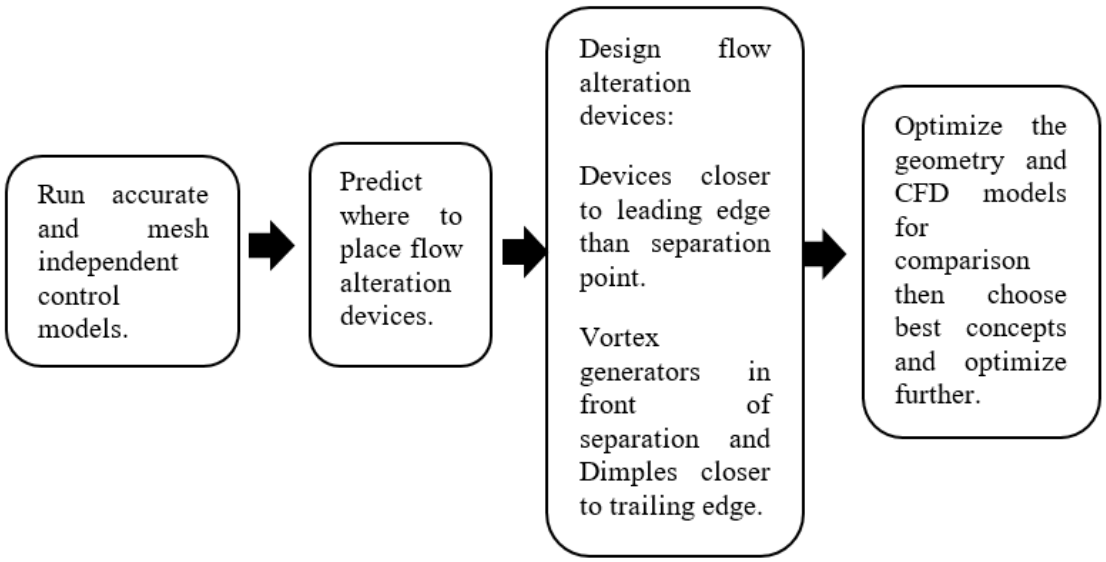

Figure 3-15: Canopy testing method.

3.4. NACA Duct

As discussed in Chapter 2, Section 2.3.10, an NACA duct was CAD modelled but not computationally tested.

3.4.1. NACA Duct Design and Testing

The methods used to design a NACA duct are explained and thereafter the actual geometry shown. Starting from the base aerofoil in Figure 2-22, the duct may be constructed using optimum ratios, w/d chosen at 4 and an α value of 7 degrees.

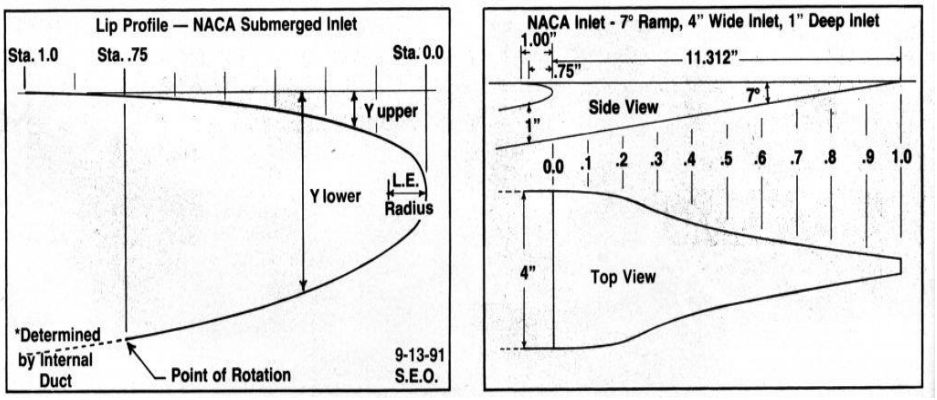

Figure 2-22: NACA duct aerofoil (Owen, 1991), (Frick, et al., 1945).

Using the step by step process outlined by Whitehouse (2015), which was found through consulting the original NACA duct design documents (NASA, 1945), an optimal NACA duct was modelled.

Firstly, an acceptable mass flow rate was determined by research into how much air the human body needs to breathe. This would be two hundred and fifty millilitres per minute of oxygen alone meaning a good estimate of air intake would be 1000 millilitres per minute.

$$Area\ of\ inlet\ (A) = \ width\ of\ inlet \times height\ of\ inlet \quad \text{Equation 2-18}$$

Mass flow rate is calculated via equation 2-19:

$$Mass\ flow\ rate\ = \ \rho \times A \times v \quad \text{Equation 2-19}$$

Using the mass flow rate it was ensured that the duct flow speed would be 70% of the vehicle velocity, hence equation 2-20:

$$Duct\ velocity = 0.7 \times Object\ velocity \quad \text{Equation 2-20}$$

Once the duct velocity is found, the area of the required inlet on the NACA duct may be found by rearranging equation 2-18 to find equation 2-21:

$$A = mass\ flow\ rate/(\ \rho \times v) \quad \text{Equation 2-21}$$

Using the optimal parameters given as having the duct inlet width as four times the height, the width is:

$$w = 4h \quad \text{Equation 2-22}$$

The above formulae may be synthesised into the following:

$$A = w \times h = 4h \times h = 4h \quad \text{Equation 2-23}$$

Rearranging:

$$h = \frac{A}{4} \quad \text{Equation 2-24}$$

The data in Table 2-1 is then multiplied by the required duct entrance height to scale the original parameters accordingly.

Table 2-1: NACA duct dimensions (Owen, 1991).

STA.	Y_U	Y_L
0.0	.197	.197
.125	.087	.325
.250	.056	.375
.375	.056	.412
.500	.021	.440
.625	.012	.462
.750	.006	.481
.875	.002	*
1.000	.000	*
L.E. RADIUS = .094		
* DETERMINED BY THE INTERNAL DUCT		

CURVED	DIVERG.
X/L	Y/W
0	.500
.10	.497
.20	.457
.30	.362
.40	.307
.50	.233
.60	.195
.70	.157
.80	.118
.90	.080
1.00	.042

Aerofoil coordinates for the side view of the duct inlet shape were simply imported using Excel and thereafter the NACA duct model built. As seen in Figure 3-16, the aerofoil coordinates for the side of the main design aerofoil is shown as imported into Inventor and then extruded and formed into the correct shape. Optimal dimensions may be found in Appendix A2; Tables A-3, A-4 and A-5.

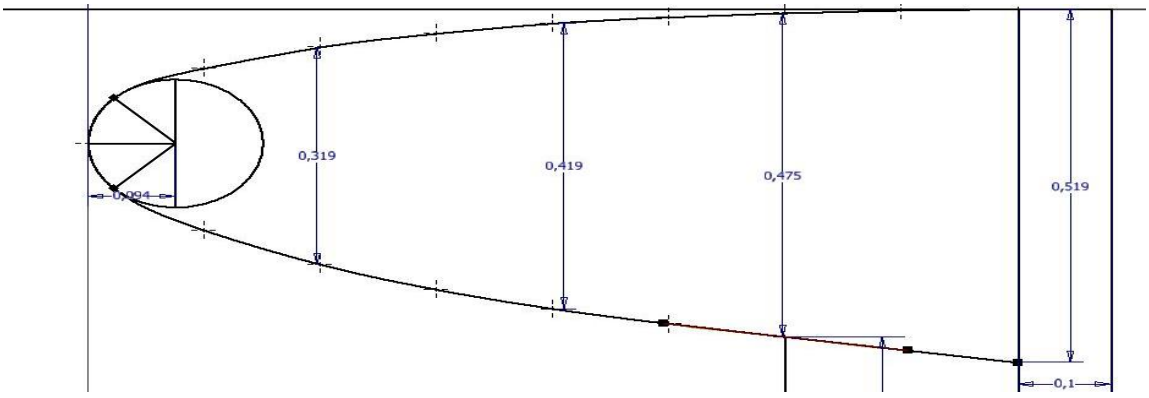

Figure 3-16: NACA duct aerofoil inlet side view.

Half of the duct top-view may be seen in Figure 3-17.

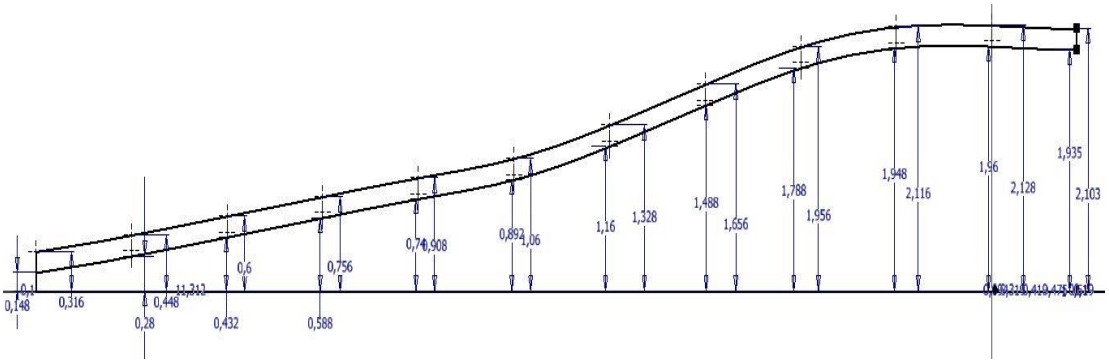

Figure 3-17: NACA duct top-view aerofoil/s.

CAD modelling of the NACA duct as un-optimised, with respect the weight, design is shown in Figure 3-18 with both side and front view.

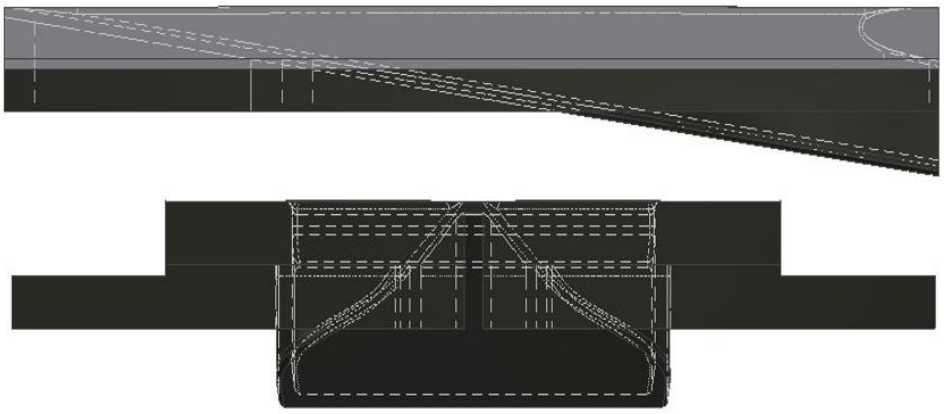

Figure 3-18: Heavy NACA duct.

The designs' weight was then reduced leaving only what was needed for the duct geometry and mounting point availability as shown in Figure 3-19, again showing side and front views.

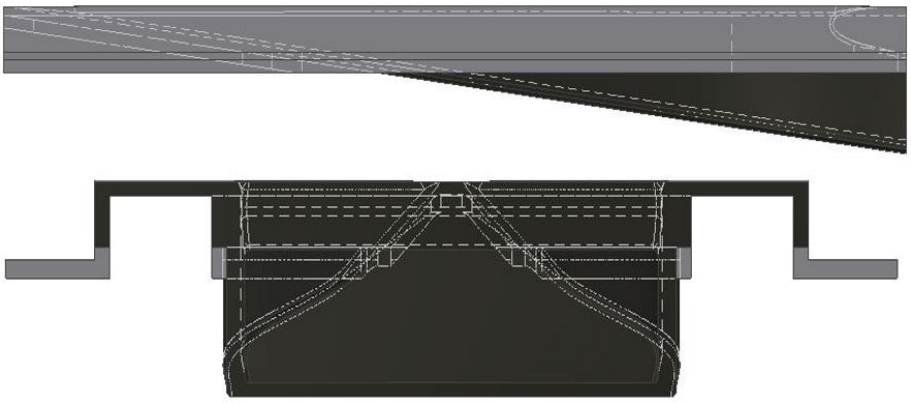

Figure 3-19: Weight Optimised NACA duct.

Figure 3-20 shows the comparison between the heavy and weight optimised NACA duct designs.

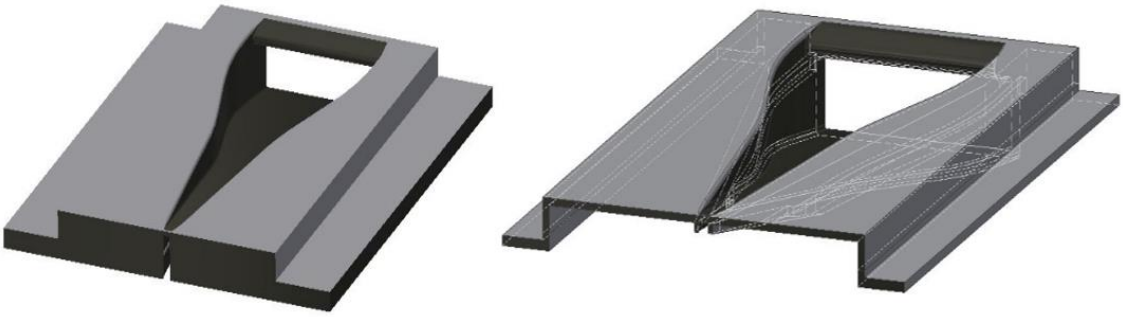

Figure 3-20: NACA duct comparison.

In order to visualise the NACA duct as applied to the canopy, Figure 3-21 shows the CAD model used for placement of the duct itself.

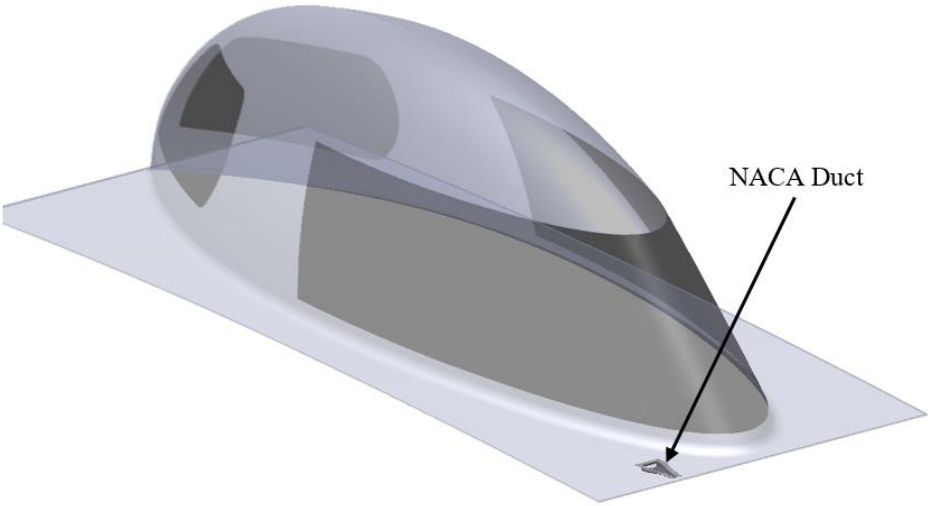

Figure 3-21: NACA duct on the canopy.

The NACA duct as placed on the canopy is shown in Figure 3-22 and illustrates how the duct was designed to smoothly take the shape of the canopy at the placement specified.

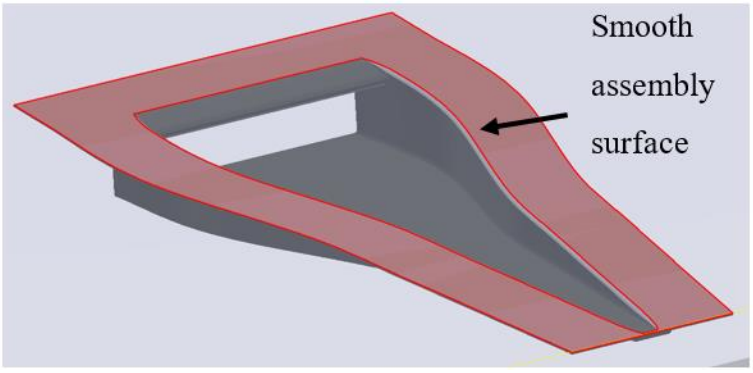

Figure 3-22: NACA duct.

The placement of the NACA duct was assigned via knowledge gained through reviewing previous placements as well as spatial constraints applied by the solar vehicle design (Hall, 1948), (Vale & Ringrow, 2011).

Volumetric wake refinement

The fluid volume wake area must be fine enough to accurately capture the wake. This alleviates the effects of a high mesh gradient from the car to the wake refinement region thereafter the outer boundary walls/symmetry planes. Wake refinement as used is shown in Figure 3-23.

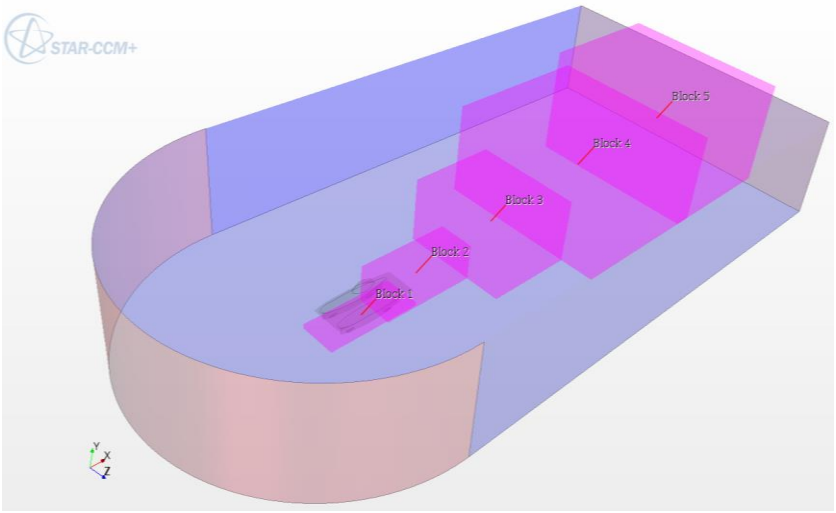

Figure 3-23: Wake refinement.

3.5. Computational Fluid Dynamics

The methods and details for meshing are described in more detail here for the canopy and wheel fluid domains. Boundary conditions are described in Sections 3.2. and 3.3. Boundary layer characteristics were analysed via CFD testing and thereafter the airflow optimised via the devices mentioned in Sections 3.2 and 3.3. The values for various mesh definitions may be analytically calculated for insertion into the CFD software. The most important factor in applying flow alteration is to find the accurate position of transition from laminar to turbulent and thereafter, the separation region as a distance along the chord length of each aerofoil taken from its leading edge. Due to the accuracy needed to resolve the boundary layer fully to pinpoint transition, a more analytical and calculated method was used to assign accurate CFD model mesh and physics boundary conditions. CFD models used previously on the solar vehicle project were larger than needed for comparison purposes due to having unoptimised meshing, lacking refinement in certain required areas and having refinement in incorrect areas. A higher degree of understanding was applied to the new specifications allowing for calculated mesh details to be used as a guide and iteratively altered to allow for accuracy to be attained while achieving mesh independence.

Mesh independence methods used for the wheel models were directly based on the methods used in Section 2.2.7. Canopy model mesh independence was to be done in a similar manner, however, the finest mesh used was then applied for the comparison models to ensure that the geometry would be accurately captured and also result in acceptable convergence.

Batches of simulations were used to allow for a final most efficient mesh to be attained. The batch mesh details can be found in Appendix A5: Tables A-9, A-10 and A-11 with explanations attached to the various mesh details used. Mesh independence was attained in these results in a similar manner to the mesh independence attained by the wheel models. The finest mesh was used, however, to ensure that that the detailed vortex generators were captured fully when discretising the fluid domain.

3.5.1. Wheel Testing Fluid Domain Meshing

The definition of the wheel testing fluid domain with regards to mesh sizing and physics boundary conditions is explained. The actual mesh sizing is mentioned as a range used for coarse and fine models. Each part of the model was assigned its own set of mesh details.

If an individual region within the model was not assigned specific mesh details, the region would use the base mesh details as a result. Table 3-1 shows the specific mesh details per region in the wheel models. Maximum target cell size and minimum allowed cell size were used. The mesh details shown were modified until the fluid domain was accurately captured, which was shown by investigating the resulting convergence, result plots and relative error values (residuals). The automated meshing used by STARCCM+ would use the mesh values and fit the mesh according to the curvature of the boundary in order to capture it as effectively as possible. The meshed boundaries would then be checked by the author using mesh quality checks, as well as checking that the convergence criteria were met.

Table 3-1: Wheel cover model mesh details.

Region, [m]	Cell Size [m]	Prism Layer Thickness [mm]	Number of prism layers	Prism layer stretching
Base mesh	1 - 0.1	10 - 40	6 - 20	1.4
Floor	1 - 0.1	10 - 40	6 - 20	1.4
Shroud	0.1 - 0.001	10 - 40	6 - 20	1.4

Region, [m]	Cell Size [m]	Prism Layer Thickness [mm]	Number of prism layers	Prism layer stretching
Wheel	0.01 - 0.0001	5 - 10	12 - 20	1.4
Interior	0.1 - 0.001	5 - 20	6 - 12	1.4
Volume refinement regions	0.3 - 0.05	-	-	-

3.5.2. Canopy Testing Fluid Domain Meshing

The fluid domain used to capture the flow characteristics over the top shell and canopy, or the entire car for analysis of canopy alteration was set up in a similar manner to that of the wheel model. Mesh details pertaining to the canopy testing models can be seen in Table 3-2.

Table 3-2: Canopy model mesh details.

Region, [m]	Cell Size	Prism Layer Thickness	Number of prism layers	Prism layer stretching
Base mesh	5 - 0.6	10 - 50	6 - 20	1.4
Top shell	0.3 -0.001	20 - 40	12 - 20	1.4
Floor	5 - 0.6	20 - 50	6 - 12	1.4
Shroud	0.3 - 0.001	20 - 40	12 - 20	1.4
Wheel	0.2 - 0.05	5 - 10	6 - 12	1.4
Interior	0.2 - 0.05	5 - 20	6 - 12	1.4
Volume refinement regions, [m]	0.3 - 0.05	-	-	-

Tables A-6 and A-7 found in Appendix A3, show detailed mesh specifications for chosen simulation speeds. These analytical results were then used to establish location-specific (shrouds, top shell, canopy, wheels, interior) boundary/prism layer specifications within the CFD models. The values were either kept at the maximum for all speeds or changed if a significant difference in results, with respect to drag coefficient and convergence, was found so that computational size could be reduced.

In order to ensure that the stretching factor was kept accurate when specifying the first prism layer details, another method that supplemented the above specifications instead of using equation 2-11 was used. This method, as recommended by Richings (2014), was to set the number of prism layers as well as stretching factor to, for example, 20 prism layers and 1.5 stretching respectively. The prism layer specifications established once the mesh had been created, were then checked by measuring the near wall prism layer and comparing it to the desired near wall layer thickness. The number of layers was then adjusted until the desired near wall thickness was achieved. The method could also have been changed to specify the near wall thickness instead of the stretching factor as well as number of prism layers, which would have resulted in a stretching factor in the correct range from 1.3 – 1.5 as desired.

3.5.3. Fluid Domain Considerations

When conducting the proposed fluid domain set-up for the wheel and canopy models, the author saw fit, as per recommendations from De Wet (2013), to separate the wheel and canopy models into each having their own set of testing criteria with regards to the fluid domain used. This was done since the computational resources as well as timing for the manufacture of the wheel covers were critical for the proposed races. In order to construct a CFD model that would simultaneously allow for testing of the wheel covers, the vehicle interior, and the canopy alteration devices such as the vortex generators, two larger more complex CFD models would be required. These two CFD models would be external flow and internal flow models. The exterior CFD model would have a boundary condition set on the opening beneath the shroud through which the wheel protrudes as a flow split. The flow split on the external flow model would be monitored for airflow characteristics and thereafter the flow split would be used as a flow inlet for the interior model and thus more complex geometry could have been tested. This was not done because the models conducted allowed for sufficient detail to be captured plus a reduction in lead time to manufacture the proposed devices (De Wet, 2013).

3.5.4. Physics Specifications

The physics specifications were assigned using previous knowledge combined with research as found in Section 2.2. These specifications define the fluid flow characteristics, the inlet and fluid property initial conditions.

Physics Models, Boundary and Initial Conditions:

The following models were selected for use when modelling the flow conditions characterised by the race conditions and solvers for the required type of CFD analysis:

- 3D – Fluid domain is kept 3-D in order to accurately capture all fluid domain geometry details.
- Steady – Flow speed is low, the aerodynamic optimisation is not time-dependent and there is no acceleration but constant velocity (Dumas, 2008), (Kuzman, 2016).
- Gas – Air density kept standard at sea level air density, 1.8 kg/m^3.
- Segregated Flow – Flow speed Mach number is less than 0.3 (De Wet, 2013).
- Constant Density – Flow speed Mach number is less than 0.3 (De Wet, 2013).
- Turbulent – K-Omega Model - Applicable for greater accuracy of external flow analysis (De Wet, 2013), (Dumas, 2008), (Sayma, 2009), (Ahmed & Chacko, 2012).
- All Y+ setting for wheel rotation models and low Wall Y+ for no wheel rotation:
    - This was due to higher amounts of turbulence occurring in the wheel rotation models as well as inaccuracies occurring within the interior wheel arch mesh but not the outer surface mesh. Low y+ setting was used due to the more accurately defined prism mesh in solid models. All y+ was used to account for inaccuracies in mesh in the wheel and wheel arch interior regions (Dumas, 2008), (Ahmed & Chacko, 2012), (Kuzman, 2016).
- Gamma Re-Theta – Modelling flow transition accurately – Usually only enabled after convergence and run until further convergence (De Wet, 2013).

In order to ensure that the Gamma Re-Theta equations result in as accurate as possible values, a user field function may be defined by defining the free stream edge (CD-Adapco, 2014):

"$WallDistance "δ" > ? 1:0"

(For boundary layer thickness, assume that the calculated value is less than "δ" metres. Where "?" refers to the boundary layer thickness for the chosen speed in the CFD analysis)

Accurate transition modelling depends on how the free stream edge is defined by the above user field function and therefore the maximum boundary layer thickness defines the free stream edge limit. It is a requirement that if the transition model was defined accurately, the field function would take the value of 1 in the free stream flow and 0 inside the boundary layer flow (CD-Adapco, 2014). This is required for the use of the Gamma-ReTheta transition model to be applied unless a set of previously used equations is applied such as the Suluksna-Juntasaro equations.

Rotating wheels

Sample Calculations for different speeds using equation 2-15 and equation 2-17 may be found in Appendix A4. Further details for chosen simulation speeds may be found in Appendix A4: Table A-8.

Crosswind analysis

An investigation into wind patterns throughout the 2014 race in SA was conducted, and the details are shown in Appendix A6: Table A-12. This data was not to be directly used in designing vortex generators for the 2015 race in Australia. The wind data for the month of October in Australia on the Stuart Highway from Darwin to Adelaide was analysed for crosswind data and used in the physics specifications on the velocity inlets specified (Coppin, et al., 2003). The data found was used to design the aerodynamic shape of the original bulk vehicle geometry as well as airflow characteristic analysis over the vehicle for flow alteration device placement.

The crosswind data acquired was unfortunately not as detailed as that found for the 2014 SASC. The direction of travel was taken as south due to travelling from Darwin to Adelaide and thus winds from the east or west were taken as crosswinds. The first crosswind simulations done would make use of assumed easterly and westerly winds of 20 kph. This resulted in a diagonal crosswind (diagonal crosswinds are not side on, but have the resultant speeds as mentioned) of approximately 72 kph being higher than used for the previous CFD modelling, though the maximum wind gust experienced in the northern territory was noted at 78 kph in October 2014 (CD-Adapco, 2014).

The crosswinds tested would thus be assumed at 10 kph and 20 kph easterly and westerly, to ascertain whether either speed resulted in a gain in efficiency when vortex generators were applied. The westerly direction was simulated first for conclusions to be drawn on whether further testing should commence.

CHAPTER FOUR: CFD RESULTS & ANALYSIS

4.1. Overview

CFD results obtained from the application of wheel covers, vortex generators and other airflow alteration devices were analysed and the findings illustrated in this chapter.

The results were ascertained from CFD simulations that were, for the most part, mesh independent and converged. Those that were not converged or mesh independent were not used for final result analysis or comparisons. Mesh independence and convergence specifications as discussed in Chapter 2, Section 2.2.7 were applied to the result sets conducted.

4.2. Wheel Optimisation Results

Concepts three, four and six as per Section 3.2.1 were not tested due to manufacturing and time constraints before the WSC; concepts one, two and five were tested. The most optimal dimensions used on investigated applications were implemented and as expected, the application of wheel covers resulted in an improvement via smooth or dimpled covers. Full result sets for the wheel testing may be found in Appendix B-1 to B-4.

The tests conducted were ensured to have reached mesh independence. Verification of mesh independence was confirmed by checking that results from finer meshes did not deviate from each other by more than 1% of the coarse mesh result value used. A general comparison between having no covers, smooth, or dimpled wheel covers yielded similar results when deciding which would be most optimal. The models were compared with different mesh details within the determined mesh specification range found for accurate testing.

Testing revealed that smooth wheel covers reduced drag on the shroud and wheel model translationally by up to 5.3 %, with the refined dimple wheel covers allowing for up to 4.9 % reduction. The reduction in rotational force on the smoothly covered wheel was approximately 43.5 % and when refined dimples were applied, the reduction was approximately 30.4 %. However, the addition of wheel covers caused the percentage downforce to increase by less than approximately 0.1 % which translates to approximately 0.0004 N rolling resistance and was expected as the airflow was head-on, not vertical. This would mean that, unlike an aerofoil, the wheels would only react to the airflow in the direction of motion, which means that translational and/or rotational effects would be noticeable. In the x-direction, the aerodynamic drag is reduced. In the y-direction, the aerodynamic downforce is negligibly increased. The force difference in the y-direction may be taken as too small to show any real comparison due to analysis uncertainties.

Residual error within the results, while usually below at least four orders of magnitude as recommended in the literature, may still yield too small a difference for any real comparison to be made. Smooth wheel covers were manufactured using polycarbonate and installed onto the solar car for the 2014 SASC. The excessive weight of the material did not allow for any significant gain in efficiency. The added weight of the covers caused rolling resistance only slightly lower than the drag reduction provided through their use. Carbon fibre wheel covers were manufactured for the WSC which allowed for a higher overall aerodynamic efficiency gain. The car proved itself to be the best in South Africa, as well as being highly competitive on the world stage and achieving an FIA international third place.

A comparison of the uncovered wheels, wheels with smooth covers, and wheels with dimpled covers, as found in the simplified geometry simulations, is shown in Table 4-1. These results indicate a significant reduction in drag as well as the torque, applied to the wheel via smooth wheel covers. Uncertainty in results does not allow for such a small reduction or increase in drag to be used as proof to validate the gain/loss in aerodynamic efficiency provided by dimpled wheel covers as shown by the preliminary and refined wheel model results. In order to allow for safety factor in the results, two orders of magnitude (result/100) error margin were used even though the residuals showed an error of fewer than four orders of magnitude. This was also done in order to exaggerate the error margin so that the results comparison showed distinct results. Residuals are a measure of the error in simulations as discussed in Section 2.2.7. A minimal gain in aerodynamic efficiency, when compounded over an entire solar car race is however significant, as may be supplied by the addition of smooth wheel covers. The values here are from medium mesh size CFD testing and so the developing of smooth and dimpled wheel covers is likely to reduce net aerodynamic drag. Preliminary models suffered from excessive flow speed acceleration near the shroud due to the narrow fluid domain. This effect was mitigated through widening the fluid domain though it did not have a substantial effect on the final comparison, wheel covering may improve aerodynamic efficiency when the wheel covers are smooth.

Table 4-1: Results - Wheel covers on a front wheel.

Wheel Covering	Preliminary Models (wheel and shroud): Force, [N]	Refined Models (wheel and shroud): Force, [N]	Refined models: Torque (wheel only), [N.m]
No cover	27.25 +/- 0.2725	9.39 +/- 0.0939	0.046 +/- 0.00046
Smooth cover	26.44 +/- 0.2644	8.89 +/- 0.0889	0.026 +/- 0.00026
Dimpled cover	26.40 +/- 0.264	8.93 +/- 0.0893	0.032 +/- 0.00032

When comparing uncovered wheels with covered wheels with error taken into account, and whether smoothly covered or dimples were applied, the covered wheels showed promise in reducing the translational and rotational forces required to propel the vehicle forward. When analysing the airflow over the uncovered wheels, the resulting translational drag and rotational drag is 9.29 Newtons and 0.046 Newton meters respectively (when subtracting the error from the original values), while having smooth covers applied, this resulted in 8.98 Newtons and 0.026 Newton Meters respectively (when adding error to the original values).

It can be noted that even with error and safety factors taken into account, smoothly covered wheels show a reduction in the energy needed to propel the vehicle forward as well as to rotate the wheels. When dimpled covers were applied the translational and rotational drag values were 9.02 Newtons and 0.32 Newton meters respectively (when adding error to the original values); it may be noted that the dimpled covers did not reduce translational drag sufficiently to justify their use when accounting for error and uncertainty in the results as the drag value is within the range of error of which applied when analysing the smooth wheel covers.

The rotational force results show a similar trend. When comparing the unrefined and refined models' result values, it shows potential error in the unrefined modelling technique, however, there is still a similar trend shown for comparisons to be made when analysing Figures 4-1 and 4-2. The unrefined model results are shown in Figure 4-1 with the error shown. The upper value indicating error added to the values shown in Table 4-1.

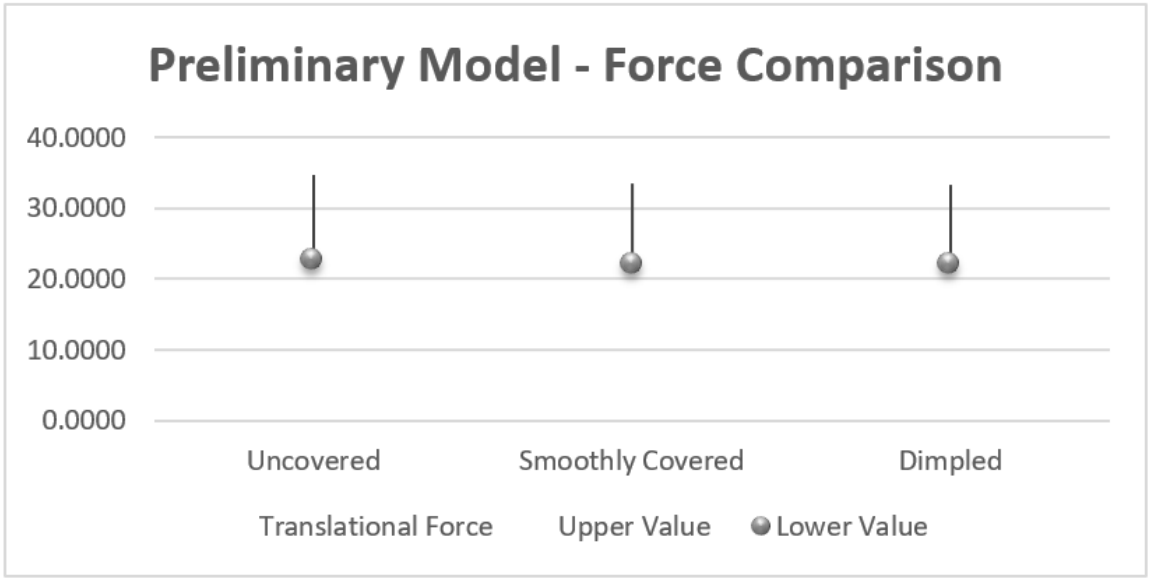

Figure 4-1: Preliminary result error comparison – Translational force.

It may be seen that there is further gain when comparing the refined model results. When analysing the potential reduction in translational forces it may be realised that when accounting for error in results, sufficiently large reduction in force is not apparent.

The unrefined model results are shown in Figure 4-2 with the error shown.

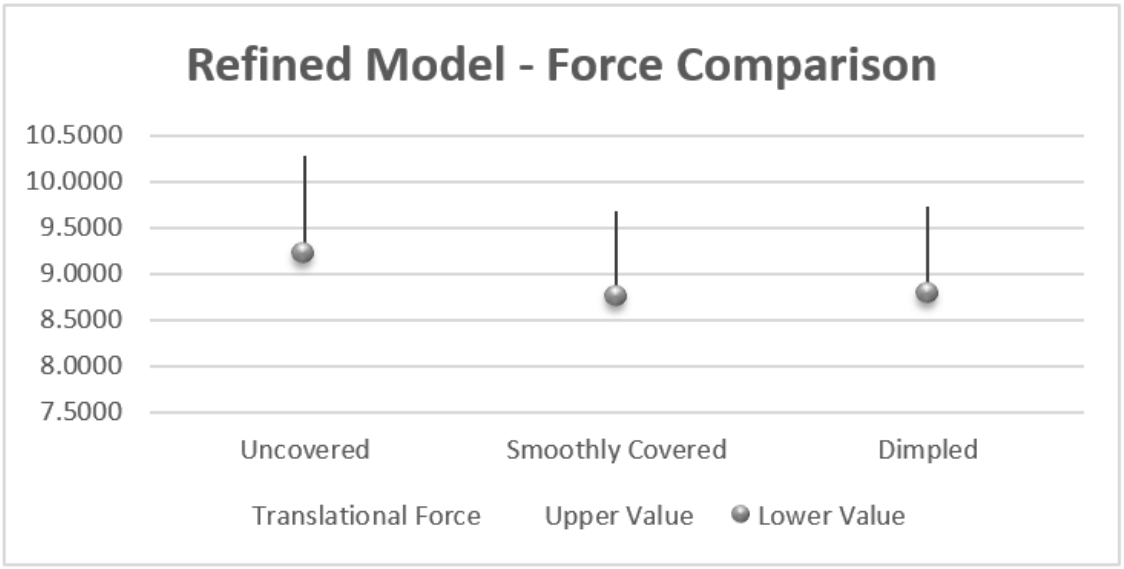

Figure 4-2: Refined result error comparison.

When analysing the rotational forces as seen in Figure 4-3, it can be seen that the rotational forces may be reduced sufficiently to realise an increase in aerodynamic efficiency as a result. Error values are small so that the dots in the illustration takes this into account.

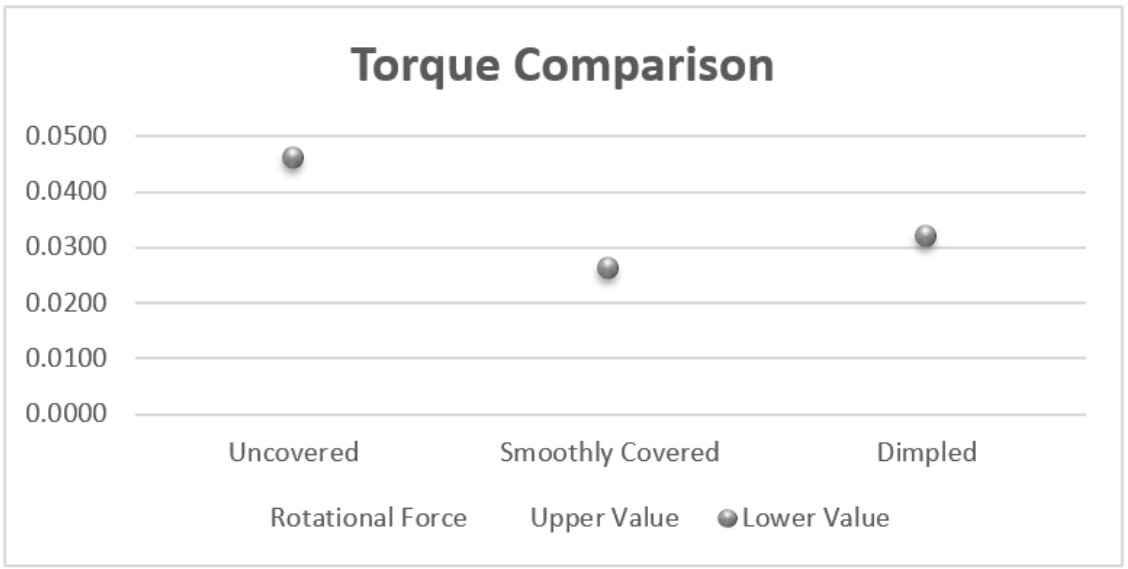

Figure 4-3: Refined result rotational force comparison.

4.2.1. Preliminary CFD models for wheel testing

In order to gain insight into whether the results correctly describe the wheel aerodynamics, an analysis of several quantities as applied to the tested fluid domain was performed.

Turbulence over the uncovered wheel is analysed in Figure 4-8 in the text to follow, which made use of vectors and a streamline to illustrate the airflow's turbulent viscosity ratio and vorticity respectively. When applying streamlines, the point of origin is kept consistent throughout so that the path it takes may give an idea of the airflow around the wheel, the sweeping of the air into the shroud, and the resulting turbulence, although these properties may be more accurately shown in the scalar plots of turbulence and vector plots shown later in this section.

Mesh Details

The mesh details that were used resulted in the volume mesh of the fluid domain used for the preliminary models. The coarse and fine mesh plots are shown in order to illustrate the accuracy of mesh and curvature matching performed by the software's automated meshing tool when assigned ranges of mesh values as discussed in Section 3.5.1.

Coarse Mesh

Figure 4-4 shows the lowest polyhedral mesh count used which resulted in the fluid domain capturing the wheel geometry with reasonable accuracy.

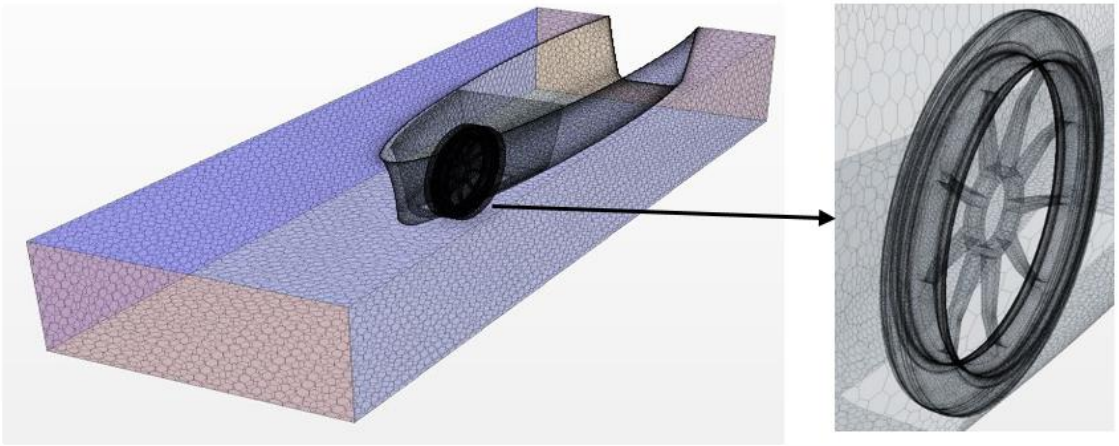

Figure 4-4: Coarse mesh on the uncovered wheel.

The mesh details needed refinement in order to capture finer details with foresight for the sizing of smaller dimples.

Fine Mesh

Figure 4-5 shows the highest mesh count used which resulted in the fluid domain capturing the wheel geometry with greater accuracy and allowed for capturing the fine dimple geometries used.

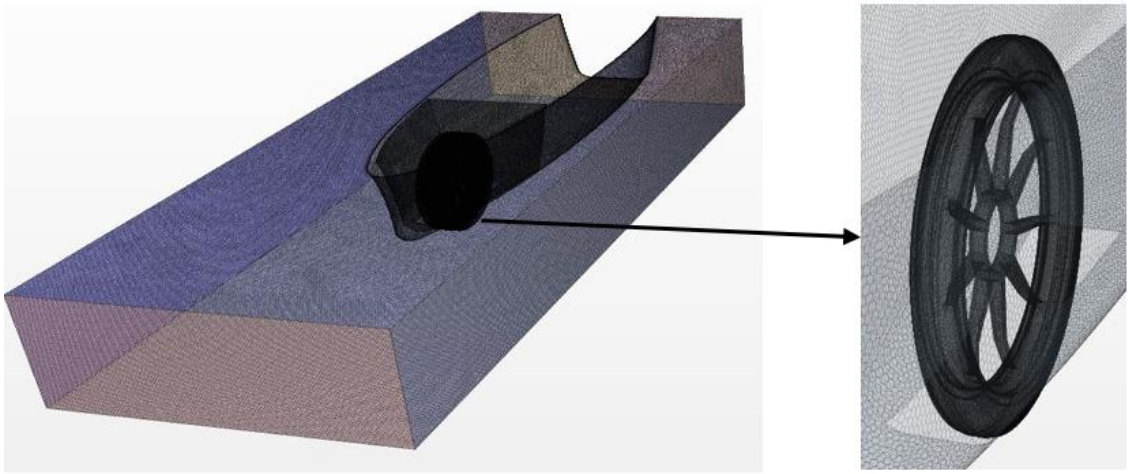

Figure 4-5: Fine mesh on the uncovered wheel.

In order to compare the meshes used, the cell quality may be analysed as shown in Figures 4-6 and 4-7. Figure 4-6 shows the coarse mesh used.

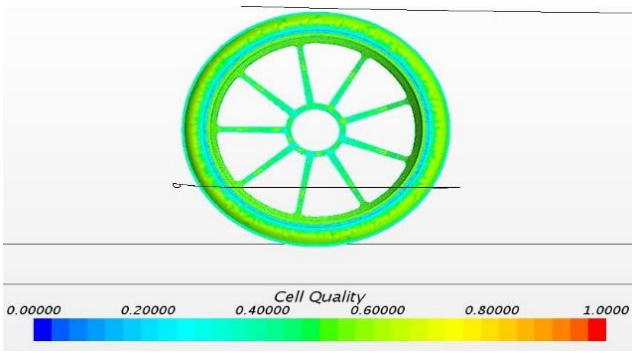

Figure 4-6: Coarse mesh cell quality.

Figure 4-7 shows the fine mesh used. The cell quality may be noted as being slightly higher.

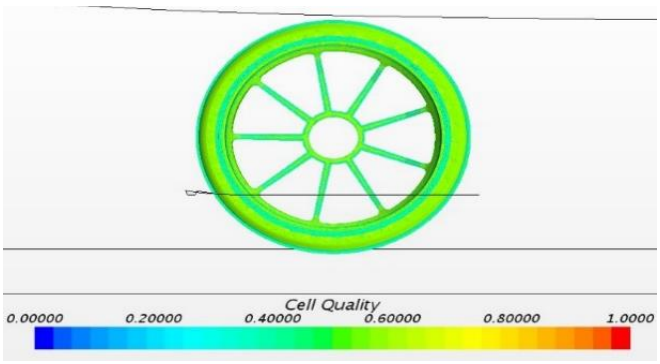

Figure 4-7: Fine mesh cell quality.

Figure 4-8 supports the assumption that the amount of turbulence in the region was high while there may be swirling occurring within the interior of the shroud. Quantities, as described in Section 2.2.8, were used to compare the wheel models. The overall turbulent viscosity ratio and vorticity were noted as higher than when the uncovered wheel is compared to smooth and dimpled cover designs shown in Figures 4-9 and 4-10.

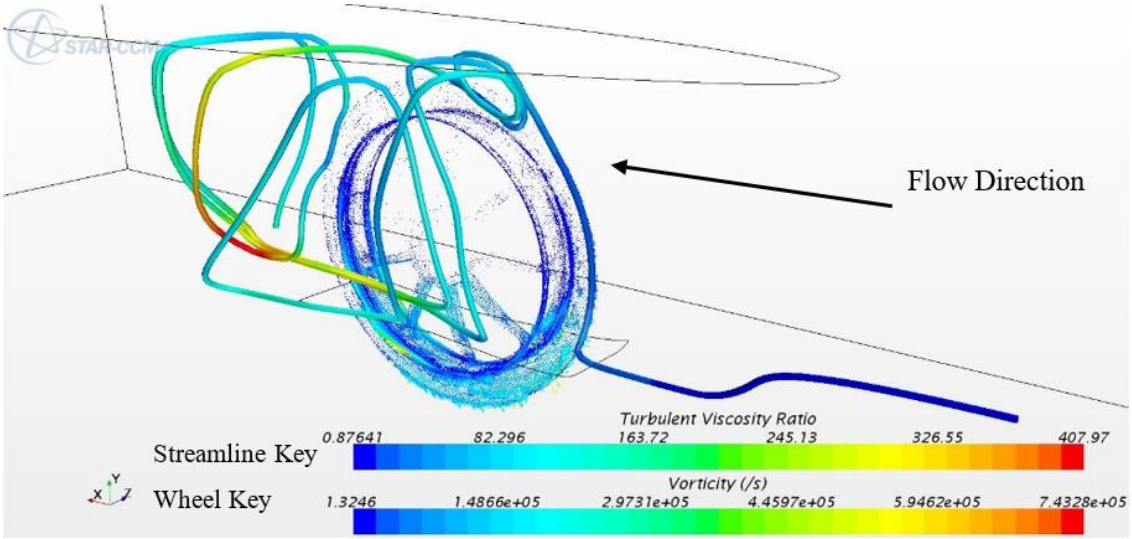

Figure 4-8: Streamlines on the uncovered wheel.

Through analysing the same quantities as applied to the wheel that has been covered with a smooth wheel cover, the resulting turbulence is shown in Figure 4-9.

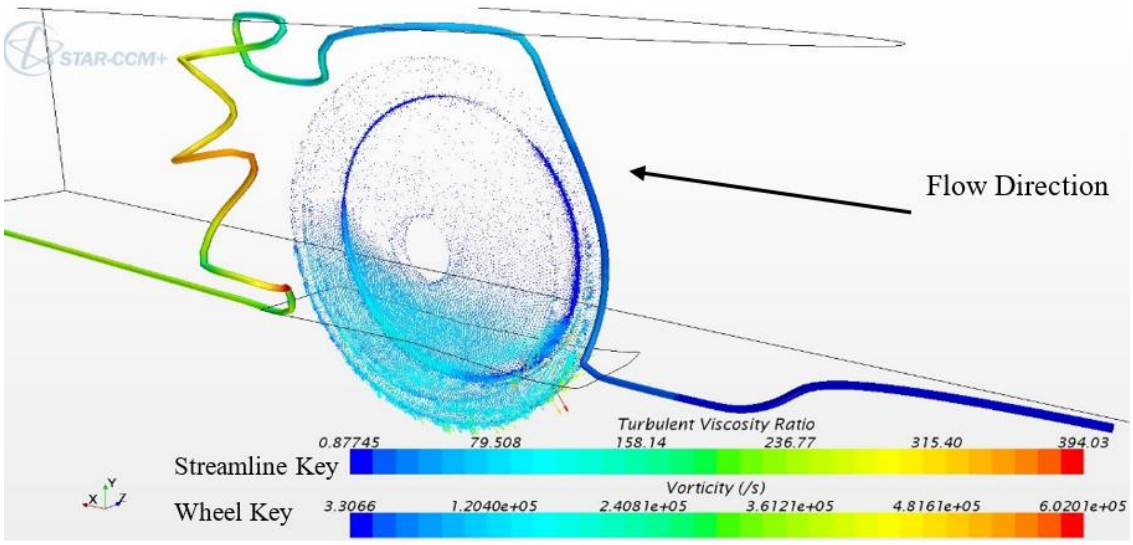

Figure 4-9: Streamlines on the smooth wheel (concept one).

It may be seen that the maximum turbulent viscosity ratio was lower than compared to the uncovered wheel although Figure 4-9 shows that there is slight swirling within the interior of the shroud.

Figure 4-10 shows the wheel with refined dimples applied to the wheel cover and the streamline as well as turbulent viscosity and vorticity values.

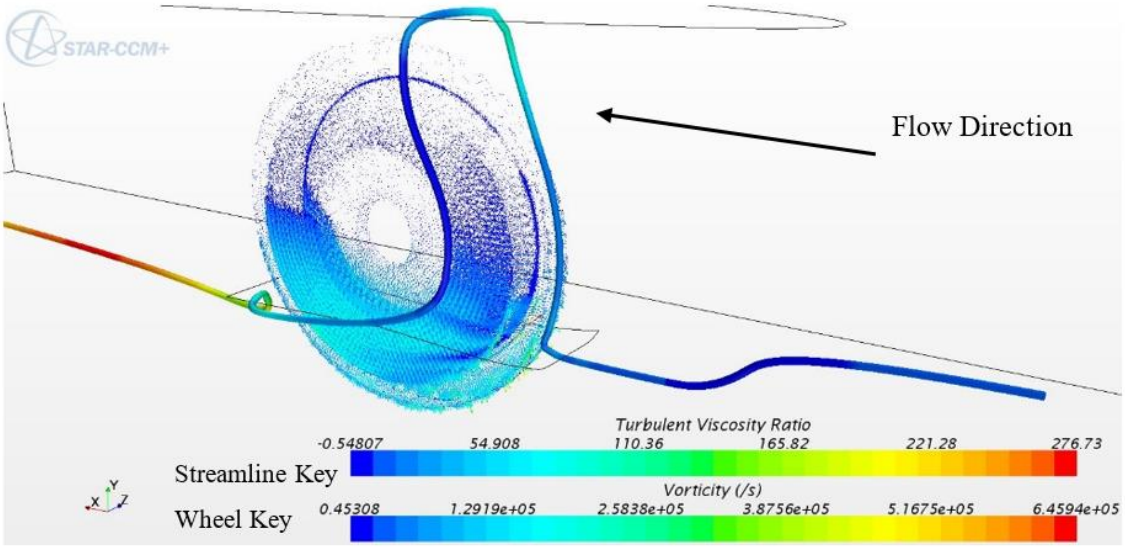

Figure 4-10: Streamlines on refined dimples applied to the smooth wheel (concept three).

It can be noted that the turbulent viscosity ratio was far lower but the vorticity slightly higher with dimples applied than when smooth wheel covers were applied. The dimpled wheel cover, however, showed potential by causing lower drag characteristics on the coarsely meshed due to the flow tripping principle using dimples as turbulators.

Dimples as applied here, show that they may cause slightly more turbulence which may result in less translational and/or rotational aerodynamic drag. The air is shown to have almost no swirling within the interior of the shroud allowing the air to escape more freely resulting in less drag. Streamlines do not show actual airflow for comparison, however, these analyses are purely observations and should not be taken as showing final comparisons. Figures 4.8 to 4.10 allow for potential certification that there may be an increase in aerodynamic efficiency to be gained from the application of wheel covers with/out dimples applied. Further analysis was thus justified. When referring to increased turbulence this shows reason to believe that separation may be occurring in similar regions which will be analysed when investigating wall shear stress applied to the wheels and covers in Figures 4-20 to 4-22. In order to further analyse the preliminary results, a turbulent kinetic energy plot was used to illustrate the turbulence caused beneath the shroud as well as within the shroud interior.

Turbulent kinetic energy plots encompassing the wheel spokes may give further insight into the amount of turbulence occurring under the shroud. The turbulence is assumed to be attributed to the wheel spokes colliding with the incident airflow.

This turbulence may be mitigated by the application of smooth or dimpled covers as will be analysed in further result plots. The turbulent kinetic energy applied to the uncovered wheel model is shown in Figure 4-11.

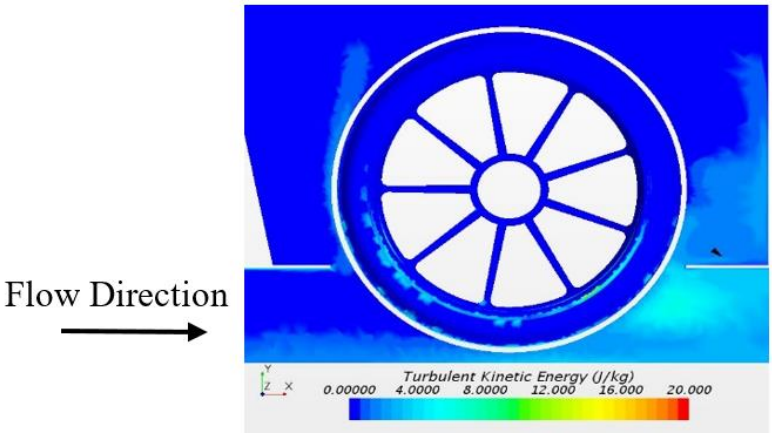

Figure 4-11: TKE on the uncovered wheel.

TKE applied to the smooth and dimpled wheel covers is shown in Figures 4-12 and 4-13.

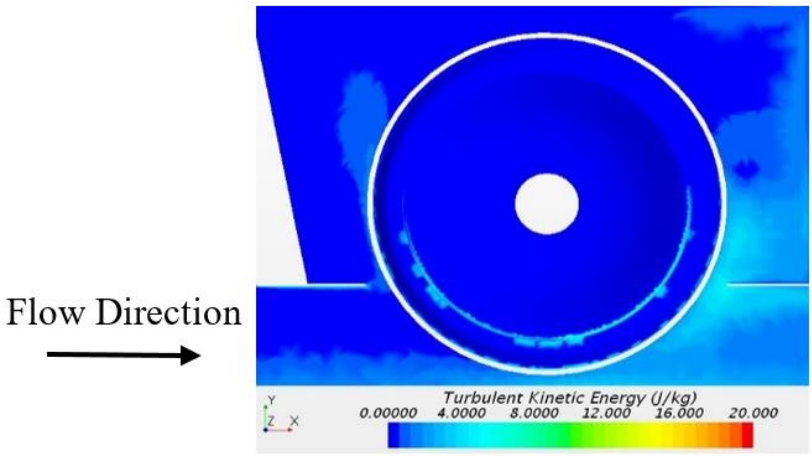

Figure 4-12: TKE on the smoothly covered wheel (concept one).

It may be noted that through the application of smooth wheel covers, the turbulence at the lower trailing edge of the wheel is reduced. These results would be verified by more accurate models.

Figure 4-13 illustrates the dimpled wheel cover model with turbulent kinetic energy scalar plot applied as discussed.

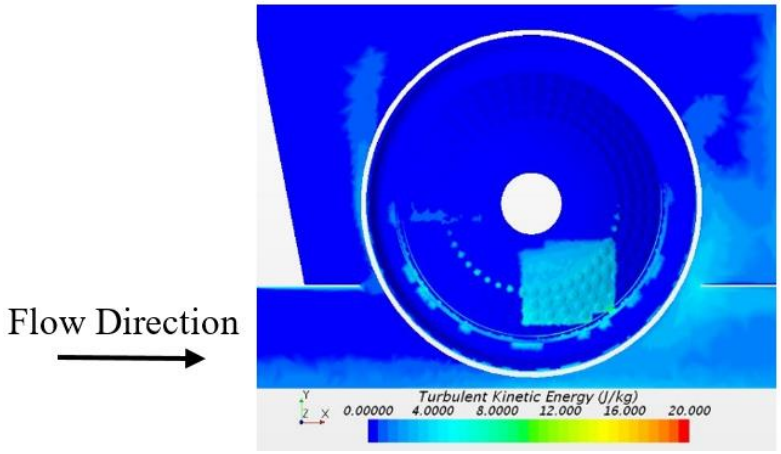

Figure 4-13: TKE on refined dimples applied to the smooth wheel (concept three).

As may be noted, the mesh applied to the dimpled covers may not have shown converged results; depicted by the rectangular region of outlier scalar values on the lower right of the wheel cover. The dimples captured to the lower left of the wheel show promise in increasing the turbulence as discussed and may potentially reduce a separation region and drag.

4.2.2. Refined CFD Models for Wheel Testing

Once use of the wheel covers was believed to be plausible, larger fluid domain models were constructed and run with finer mesh details, the results of which are illustrated here.

Turbulent kinetic energy illustrated

Figure 4-14 shows the TKE applied to the uncovered wheel. The plot shows higher turbulence levels in the vicinity of the spokes, as expected. The turbulence at the lower trailing edge of the wheel is also higher than the leading edge which shows an increase in turbulence over the wheel.

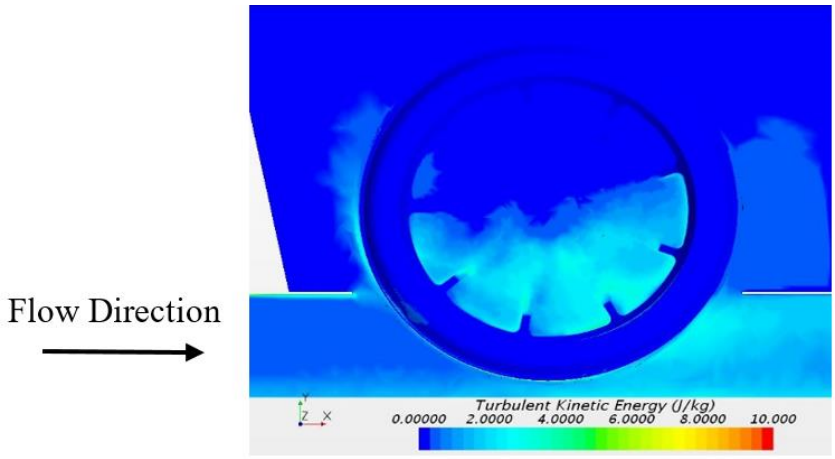

Figure 4-14: TKE on the uncovered wheel.

Figure 4-15 shows the TKE as applied to the covered wheel within the shroud. Turbulence levels were reduced at the lower trailing edge of the wheel compared to the uncovered wheel showing a reduction in turbulence over the wheel.

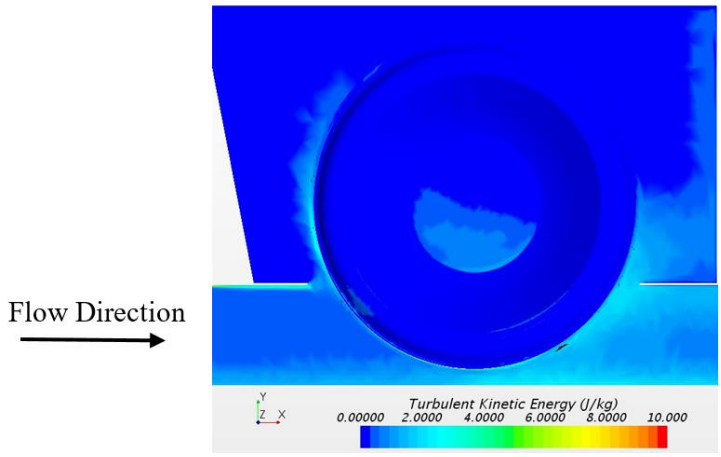

Figure 4-15: TKE on the smoothly covered wheel (concept one).

Figure 4-16 shows the TKE as applied to the covered wheel with dimples applied to the wheel cover.

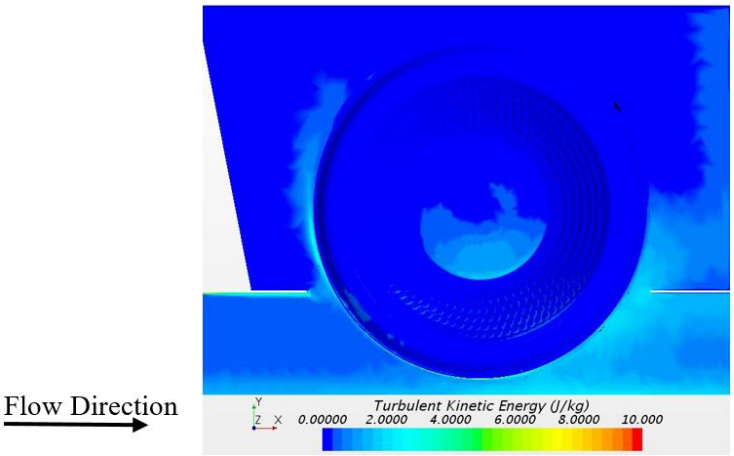

Figure 4-16: TKE on refined dimples applied to the smoothly covered wheel (concept three).

An increase in turbulence on the dimpled areas may be noted as opposed to the smoothly covered wheel.

Velocity illustrated

In order to gain further insight into the flow characteristics around the wheel, covered or uncovered, velocity scalar values in the vicinity of the wheel were plotted.

Figure 4-17 shows the velocity applied to a centrally positioned plane to show the flow characteristics around and on the wheel. The velocity line integral convolution plot shows how there is circulation within the interior of the shroud as well around the spokes of the wheel. This may affect the torque required to rotate the wheel as well as turbulence and hence translational drag.

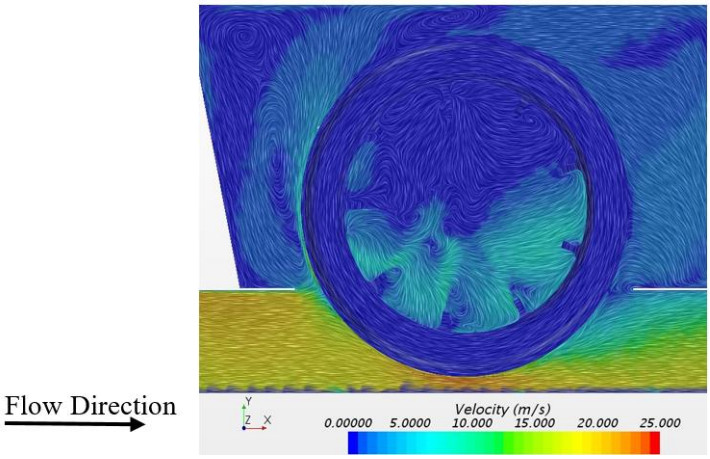

Figure 4-17: Velocity on the uncovered wheel.

For comparison to the smoothly covered wheel, Figure 4-18 illustrates the velocity line integral plot applied to the smoothly covered wheel.

The swirling within the interior of the shroud is still apparent compared to the uncovered wheel although it seems to be more uniform and reduced in the central portion of the wheel. With the swirling apparently reduced, the torque applied may also be reduced by the addition of smooth wheel covers. Turbulence may also be reduced resulting in reduced translational force applied to the wheel.

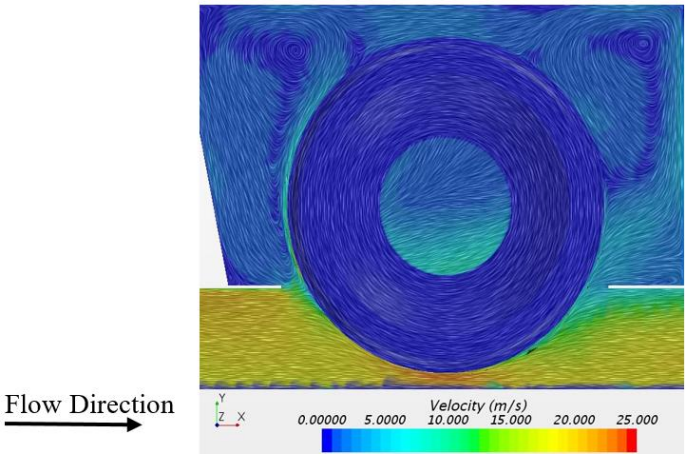

Figure 4-18: Velocity on the smoothly covered wheel (concept one).

In order to analyse the effectiveness of the dimpled cover, Figure 4-19 is shown to illustrate the line integral plot applied to the dimpled wheel cover.

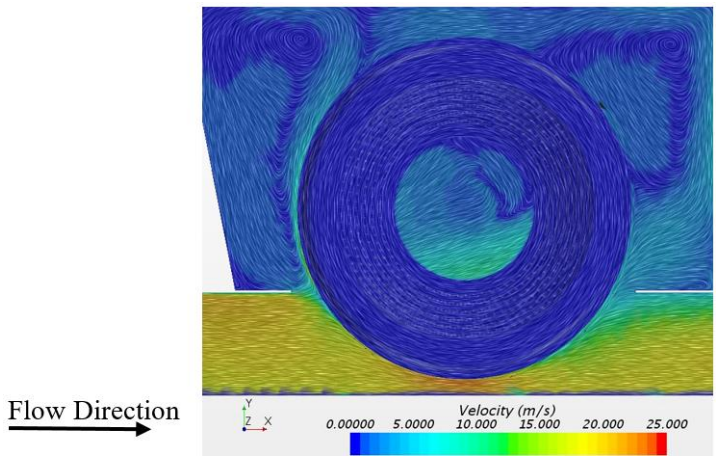

Figure 4-19: Velocity on refined dimples applied to the smooth wheel (concept three).

Swirling patterns are still apparent and similar to when analysing the smoothly covered wheel. The swirling is more apparent in the central part of the wheel compared to the smooth wheel cover. This could be because there may be slightly increased turbulence compared to the smooth wheel cover which may reduce separation or result in increased rotational and translational drag.

Wall shear stress illustrated

In order to investigate the effectiveness of the dimples with regard to increasing turbulence levels by analysing wall shear stress, Figures 4-20 to 4-22 are shown.

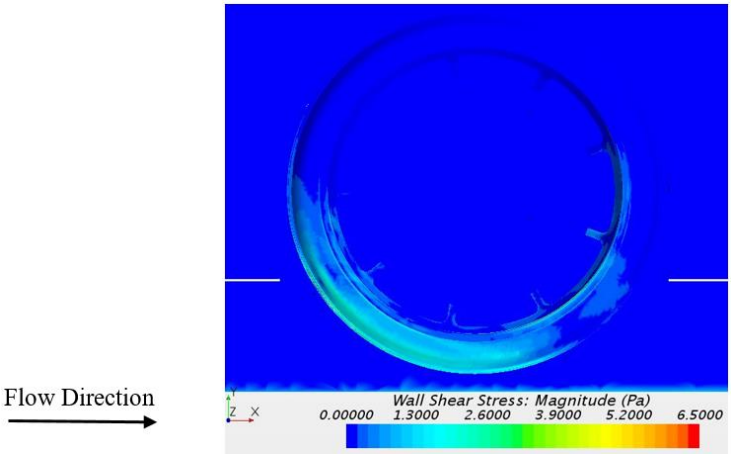

Figure 4-20: Wall shear stress on the uncovered wheel.

As may be noted from Figure 4-20, the wall shear stress is higher on the wheel surface than on the spokes and the interior. This shows detachment of airflow off the trailing edge of the wheel and within the interior of the vehicle.

Analysing the shear stress between the fluid and the smoothly covered wheel as shown in Figure 4-21, it may be noted that the shear stress is increased on the wheel cover which may show increased attachment of airflow to the wheel and cover.

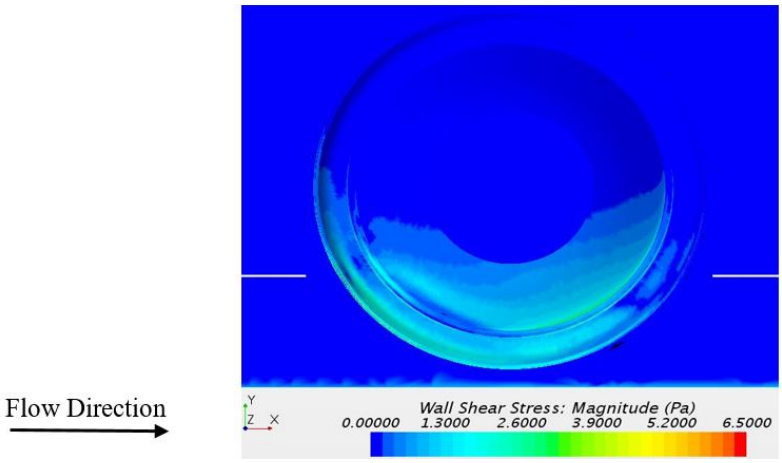

Figure 4-21: Wall shear stress on the smoothly covered wheel (concept one).

In order to analyse the effectiveness of the dimples as mentioned, Figure 4-22 shows similar flow characteristics regarding wall shear stress to that of the smoothly covered wheel. The shear stress shows decreased values in the centres of each of the dimples which may show separation. The analysis shows that smoothly covered wheels decrease the turbulence caused by the wheel spokes while dimpled covers do not show significant effects compared to the smoothly covered wheel.

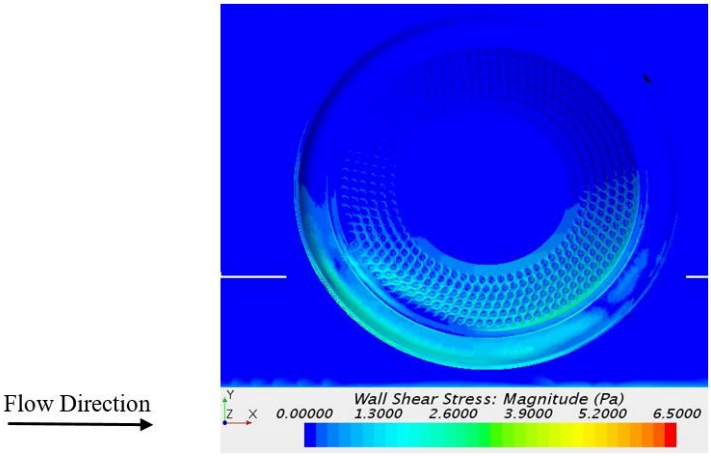

Figure 4-22: Wall shear stress on refined dimples applied to the smooth wheel (concept three).

Mesh Independence Illustrated

To compare results, common practice as mentioned in Section 2.2.7, is that the result value used for comparison, at a higher mesh count, should have a value within one percent of the higher mesh count result value.

The drag force on the uncovered wheel at different mesh counts is shown in Figure 4-23 to have a value that falls within the one percent range of the higher mesh count value.

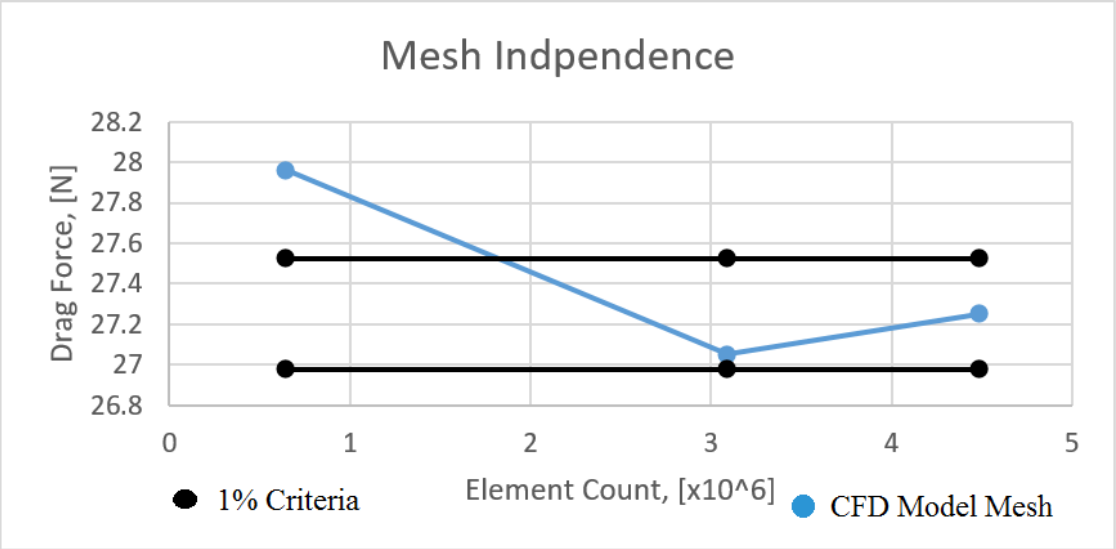

Figure 4-23: Mesh Independence shown for the uncovered wheel.

The mesh independence for the design iterations for wheel comparisons as well as canopy models showed similar trends. The canopy model mesh independence trends are discussed in more detail in Section 4.3.

4.3. Canopy Alteration Results

Canopy testing began with finding the most accurate mesh details through testing batches of CFD models with different mesh details according to the ranges shown in Section 3.5.2. Appendix A5 Tables A-9 to A-11 show the mesh details tested in order to find the most robust mesh to use for testing of the entire vehicle and topshell-canopy only CFD models. Each batch had objectives set and these objectives were investigated and the outcomes noted according to the convergence criteria required as discussed in the tables mentioned.

Convergence was established and thereafter the finest mesh details used so that time was saved in finding mesh independence for each model for every iteration of the design. Mesh independence was noted in these batches but not noted exclusively as the finest mesh was used for the comparison testing.

Comparison of the simulations conducted was therefore as accurate as possible taking into account the size of the fluid domain as well as the size of the resulting CFD model. Constraints placed on the project ensured that results had been conducted within a set time frame so that deadlines were met for manufacturing and implementation to the vehicle.

CFD testing has uncertainty in results and thus the tests conducted in part one and two were used for preliminary design feasibility analysis; thereafter testing involved a third part. Mesh independence may be seen when analysing the results tables mentioned in the three parts that testing were conducted as explained here:

Part one results are depicted in Appendix B1; Table B-1, B-2, B-3 and B-4, and involved testing whether the rotating wheels and rolling road physics affect the canopy aerodynamics. Vortex generator placement was determined after the transition and separation characteristics of the airflow were investigated. Scalar scenes were analysed using several flow definition quantities and thereafter the separation region characteristics suggested as discussed later.

Though there may be slight error involved in this method, the error was mitigated when outlier tests were done, such as placing the flow alteration devices in areas that are not linked to suggestions when consulting literature. This demonstrated methods used in literature, Section 2.3, as well as the author's methods of applying the proposed devices. The author's suggestions, as based on the literature used, resulted in an aerodynamic efficiency increase (drag reduction).

Part two results as depicted in Appendix B2; Table B-7, involved testing vortex generator effects on the entire car model which are explained in Section 3.3.3. These tests allowed for straight inflow as well as crosswind testing. Concept one was not tested as the literature in Section 2.3.5 suggested concepts two and three to show higher potential. Concept two resulted in a drag force rounded to 47 N with no crosswind applied, while not having vortex generators applied resulted in a drag force rounded to 38 N, an increase of approximately 9 N or approximately 23.7 percent. This allowed for only the testing of concept three due to resulting in a drag force of approximately 38 N when no crosswind was present. The drag reduction was noted as approximately zero. When a crosswind was applied, concept three resulted in a rounded 37 N as opposed to 38N with no vortex generators applied. Thus, concept three would be compared to not having vortex generators applied in the analysis, and further testing commenced.

Part three involved testing with strong and weak crosswinds applied at 10 and 20 kph, respectively, on the canopy and top shell only model. The results are captured in Appendix B2; Table B-8 and B-9. These results may be consulted for numerical comparisons to be made however, scalar plots to follow further analyse the vortex generator effectiveness and thus the one Newton drag reduction mentioned previously shows the potential drag reduction possible, or at the very least that the vortex generators showed promise in reducing aerodynamic drag.

The final mesh used on the canopy and top shell models is shown in Figure 4-24. Here it can be seen that the mesh used allows for accurate capturing of the small detailed vortex generator geometry as well as the detailed top-shell geometry. The wheel and shroud geometry were captured with similar detail as shown by the wheel models.

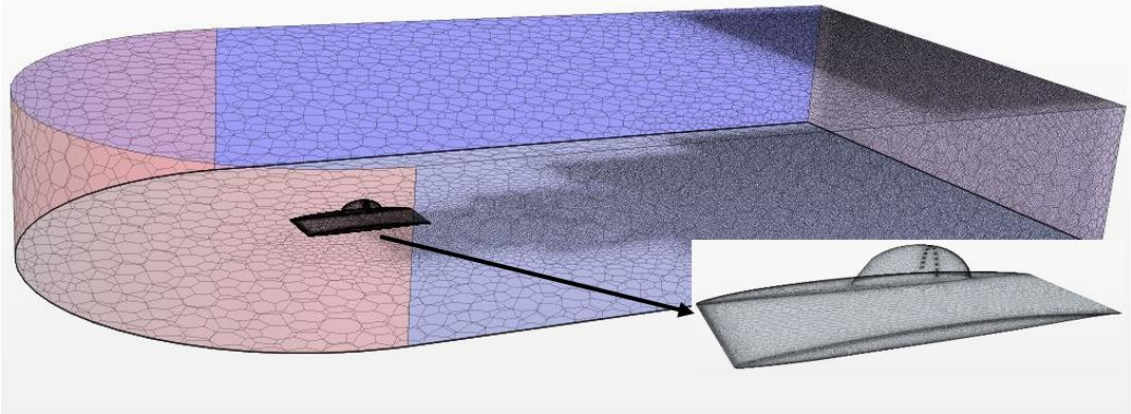

Figure 4-24: Canopy mesh – Top shell and canopy with VG's further forward.

The resulting mesh shown here indeed captures the canopy, top shell and vortex generator geometries with no cell quality errors to inhibit on the convergence of the solution.

4.3.1. Part One – Wheel Rotation and Rolling Road Effects on Canopy:

The results for the first part of the three testing methods are substantiated here by analysing airflow characteristics. The wheels were set to have zero rotational speed and were compared to having the relevant rotational speed applied while the floor was set as either stationary or a rolling road.

TKE illustrated

A top-view of the entire car with a simplified interior is shown with TKE applied in Figure 4-25. Wheel rotation and a rolling road were set for zero radians per second rotation.

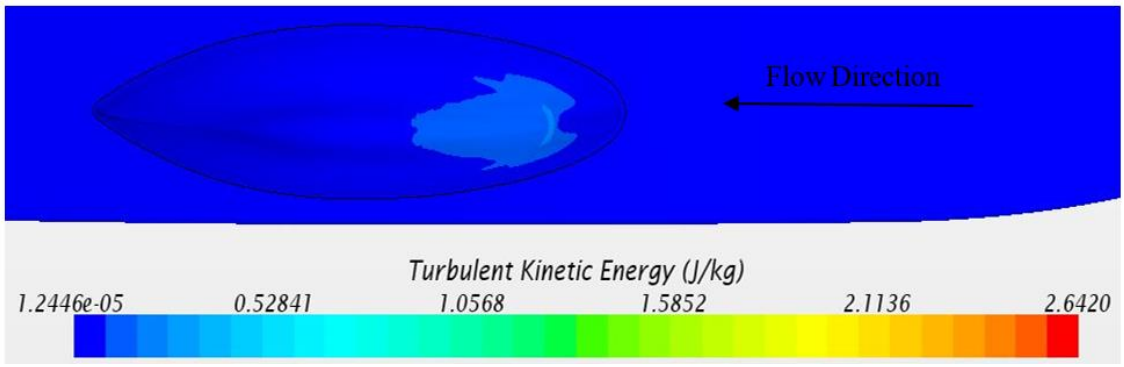

Figure 4-25: Canopy Model - Stationary wheels – TKE.

Comparing the above stationary model to having wheel rotation and rolling road effects set accordingly for 70 kph solar vehicle velocity, TKE applied is shown in Figure 4-26.

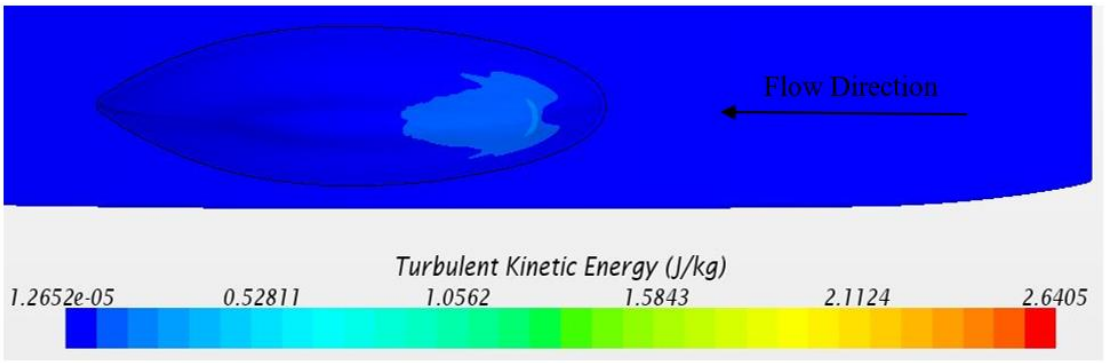

Figure 4-26: Canopy Model - Rotating wheels – TKE.

The turbulence is highest at the point of highest curvature and not affected by wheel rotation.

Pressure illustrated

A top-view of the entire car with a simplified interior is shown with pressure applied in Figure 4-27. Wheel rotation and rolling road effects were set accordingly for zero radians per second.

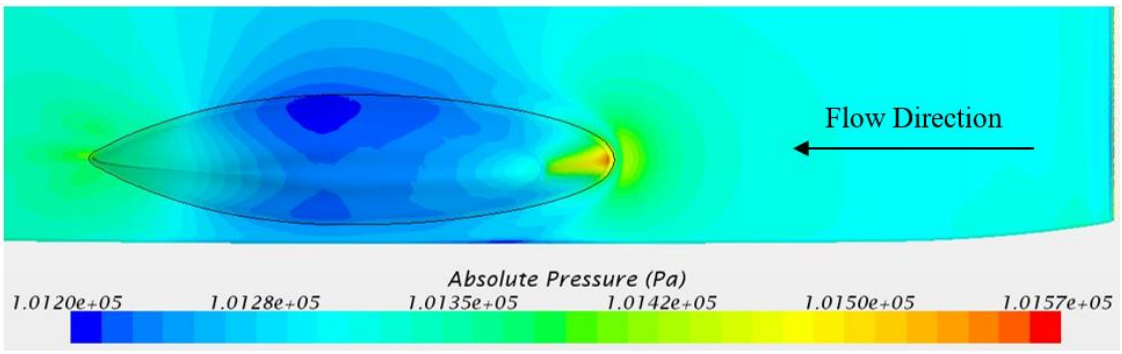

Figure 4-27: Stationary wheels – Pressure distribution.

Comparing the above to having wheel rotation and rolling road set accordingly for 70 kph solar vehicle velocity, the pressure applied is shown in Figure 4-28.

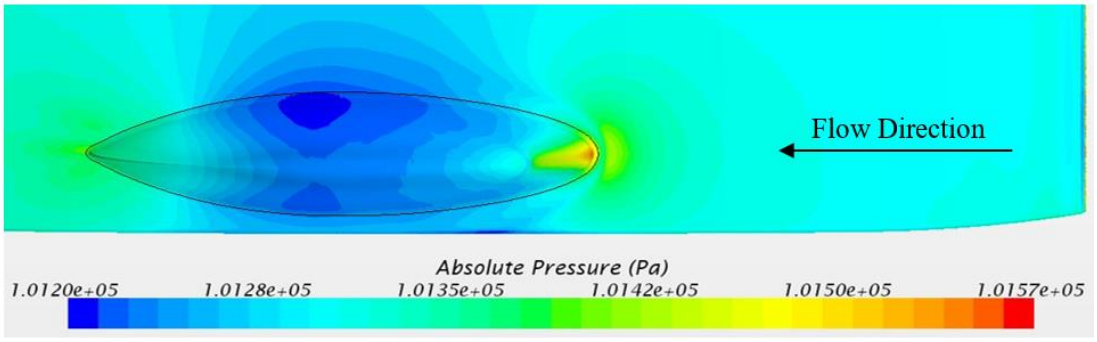

Figure 4-28: Rotating wheels – Pressure distribution.

The pressure patterns are near identical therefore wheel rotation does not have a significant effect on canopy aerodynamics.

Streamlines illustrated

The entire car with a simplified interior and wheel rotation set to zero radians per second with streamlines illustrated are shown in Figure 4-29. Streamlines indicate air flow over the car but this does not give a direct indication of the air flow characteristics.

Figure 4-29: Stationary wheels – Wall shear stress and streamlines.

Comparing the zero radians per second wheel rotation model to wheel rotation set accordingly for a 70 kph solar vehicle velocity, the wall shear stress is shown on the streamlines in Figure 4-30.

Figure 4-30: Rotating wheels – Wall shear stress and streamlines.

The wall shear stress as shown, may indicate to some extent that wall shear stress is nearly identical for both illustrations while being low as expected. From this point further, testing of only the canopy and top shell was permitted for further vortex generator design. Refinement of the design was performed in the analyses to follow with finer meshes as well as more rigorous and further analyses of the actual effects caused by the vortex generators.

Separation point illustrated

In order to place vortex generators, a fine mesh was used on the entire car model and thereafter the separation region estimated and used to place the vortex generators.

In Figure 4-31 the estimated separation region is shown using an iso-surface set to display a maximum value of 0.1 J/kg TKE. TVR is applied to the actual iso-surface to give an indication of the turbulence pattern on the iso-surface. Vortex generators were then placed at a smaller distance forward from the separation region, and 100 h from the leading edge as described in Section 2.3.5 while modifying the placement according to the split in the canopy needed for the opening thereof.

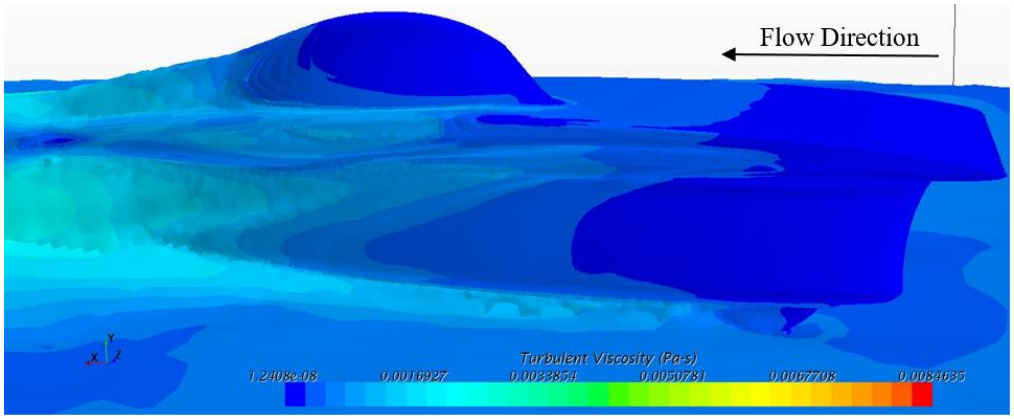

Figure 4-31: Canopy separation – TKE iso-surface with turbulent viscosity applied.

To get a quantitative estimate and visualisation of where exactly the air would separate, a perpendicular side view of the iso-surface was used as shown in Figure 4-32.

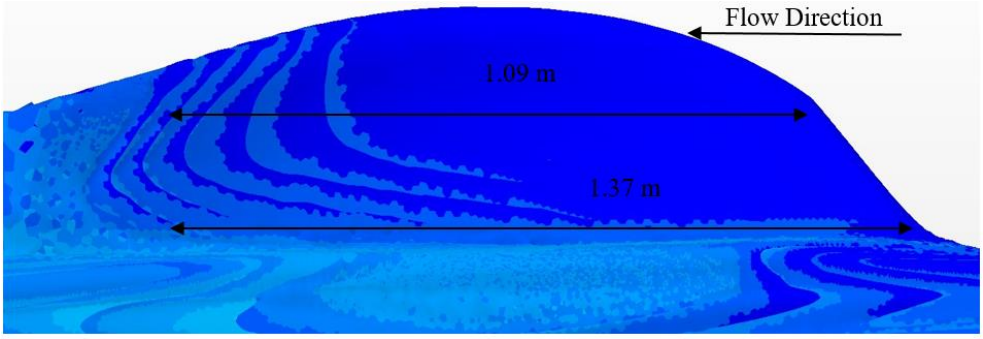

Figure 4-32: Canopy separation point – TKE Iso-surface with turbulent viscosity applied.

Here it may be noted that through a commonly used convention on depicting separation points in the CFD package, the placement of the vortex generators may prove correct. This was proven through testing and analysing the chosen placement areas as is shown in further testing and analysis.

4.3.2. Part Two – Vortex Generators on Entire Car Model:

The testing of the vortex generator placement on the canopy is shown on CFD models that account for the entire solar vehicle.

Wall shear stress illustrated

The wall shear stress applied indicates the attachment of airflow on the canopy as well as the effects of the vortex generators. In Figure 4-33 the wall shear stress is shown on the canopy without vortex generators applied.

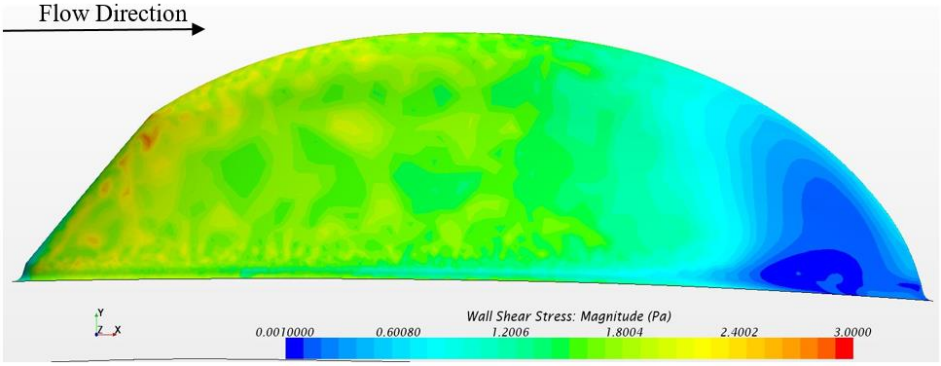

Figure 4-33: Wall shear stress on the canopy, no VG's.

Comparing Figure 4-33 to Figure 4-34 which has wall shear stress applied to concept two vortex generators placed on the canopy, we see that the vortex generators have a significant effect on increasing the turbulence of the airflow without delaying the separation zone. The placement of VGs in Figure 4-34 shows that while altering flow characteristics by increasing the turbulence, this does not aid in reducing drag as the separation region is not decreased in size.

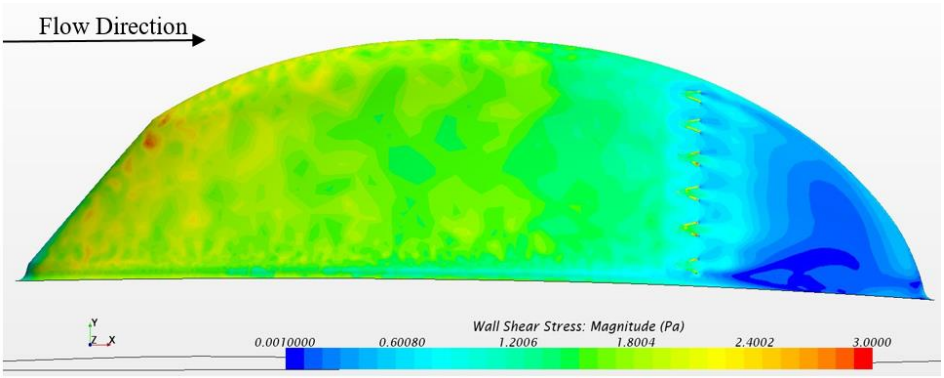

Figure 4-34: Wall shear stress on canopy: VG's further back (concept two).

If the wall shear stress is then applied to concept three as shown in Figure 4-35, we see that the separation region is somewhat delayed. Separation is shown to be delayed even though shear stresses near the vortex generators are higher than on a smooth canopy due to having slightly higher turbulence attributed to the vortex generators. The separation region seems to begin at the area of placement of the vortex generators in Figure 4-34 while in Figure 4-35 the separation region seems to begin a distance from the vortex generators. The actual distance from the leading edge to the separation points and the difference between this distance when comparing concept two and three is shown in Figures 4-40 and 4-41.

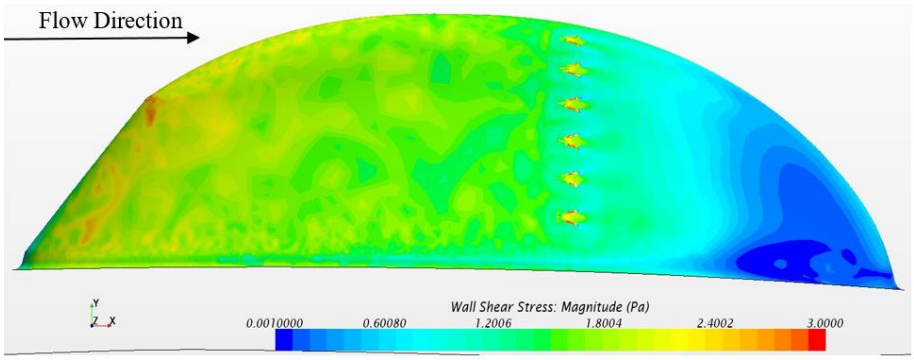

Figure 4-35: Wall shear stress on canopy, VG's further forward (concept three).

Here we see that there may be a potential gain in applying the vortex generators in this position to reduce the size and magnitude of the separation region and thus reduce drag as a result.

4.3.3. Part Three – Top shell and Canopy with Crosswinds:

Analysis of crosswind testing with vortex generators applied is shown to account for effectiveness in different race conditions. The CFD models incorporated only the canopy and top shell.

Turbulence intensity illustrated

The turbulence intensity from crosswinds over the smooth canopy with no vortex generators applied may be seen in Figure 4-36.

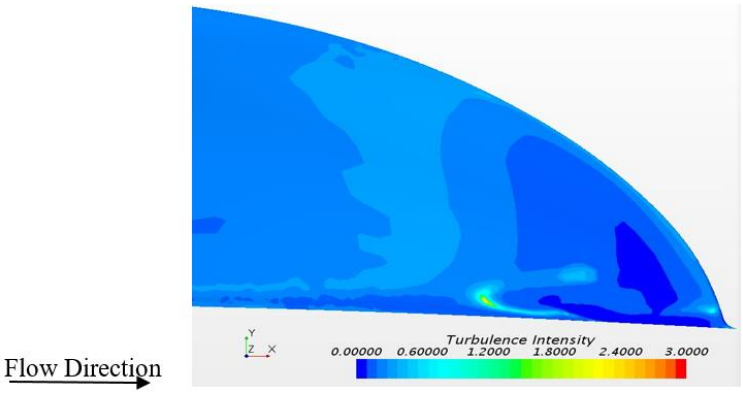

Figure 4-36: Turbulence due to crosswinds, no VG's.

Comparing the turbulence intensity illustrated in Figure 4-36 to the turbulence shown on concept three applied, with vortex generators placed further forward on the canopy, is shown in Figure 4-37. Concept two was not analysed here due to the potential gain being seemingly higher for concept three.

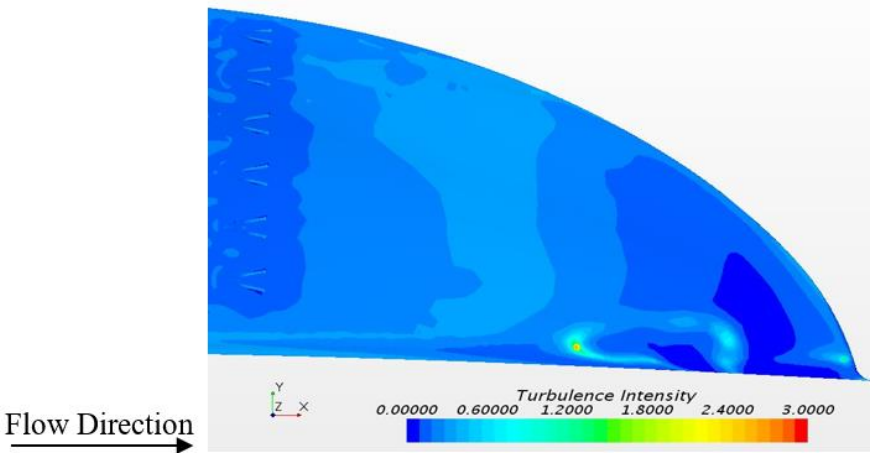

Figure 4-37: Turbulence due to crosswinds, VG's further forward (concept three).

The turbulence intensity is spread over the surface of concept three while the smooth canopy has turbulence concentrated near the trailing edge. The turbulence is seen to be increased on the ends of the vortex generators. Comparing the turbulence intensity characteristics of a smooth canopy to a canopy with the correctly placed vortex generators, an increase in turbulence and thus a reduction in the separation region is shown in Figures 4-36 and 4-37.

Skin friction illustrated

Figure 4-38 shows the characteristics when a skin friction plot is applied to the smooth canopy without vortex generators applied.

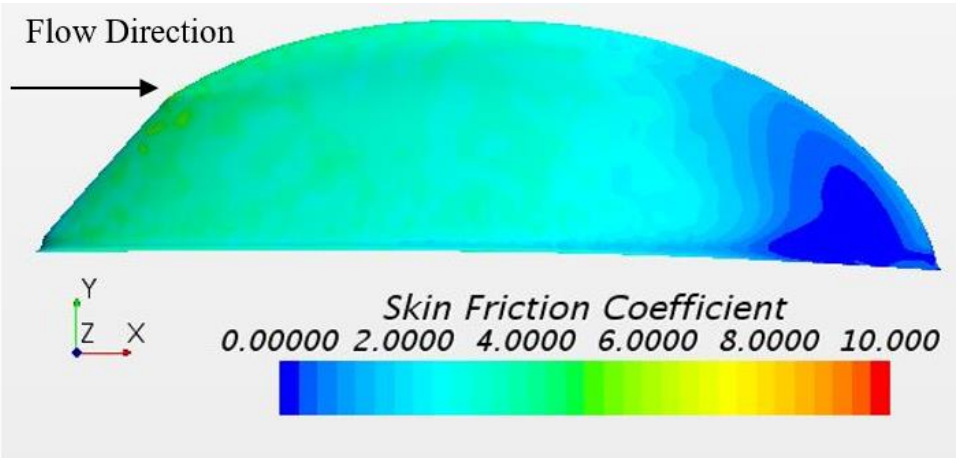

Figure 4-38: Skin friction, no VG's.

Comparing Figure 4-38 with the skin friction applied to the canopy without vortex generators to the canopy with vortex generators is shown in Figure 4-39.

The skin friction increases slightly in the vicinity of the VGs showing that the effects of increased turbulence increases skin friction.

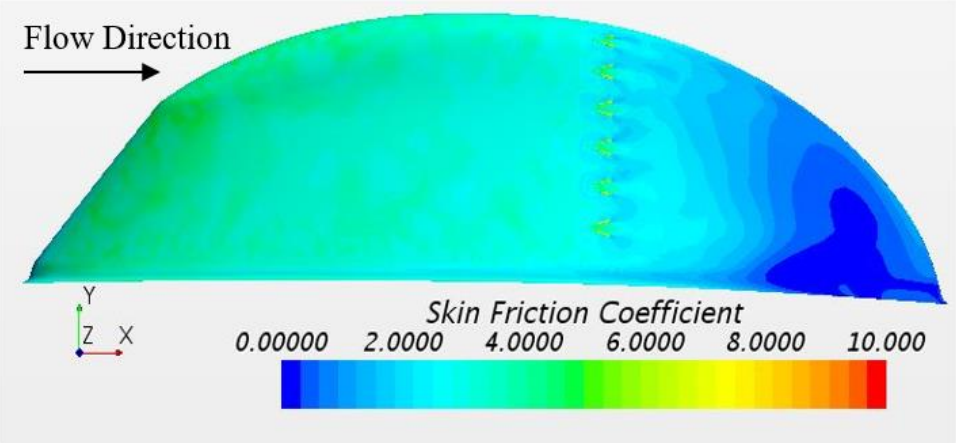

Figure 4-39: Skin friction, VG's further forward (concept three).

Overall drag is reduced though proving the concept of adding turbulence, resulting in increased skin friction, to delay separation.

Iso-surface illustrated

Figure 4-40 shows the separation estimate on the smooth canopy using an iso-surface of turbulent kinetic energy with a minimum of 0.1 J/kg setting as previously shown in Figures 4-31 and 4-32.

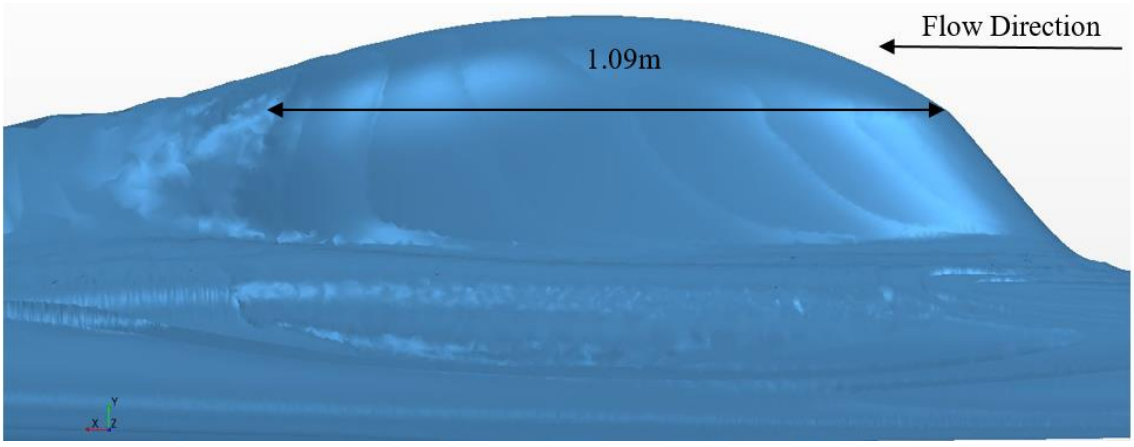

Figure 4-40: TKE iso-surface for separation analysis, no VG's.

It may be noted that the flow seems to have a laminar nature for the majority of the canopy surface but that when the curvature increases, the airflow begins to separate similar to the characteristics of bluff bodies.

Comparing the separation in Figure 4-40 with a distance to separation of 1.09m, to the canopy with concept three applied in Figure 4-41, where the distance to separation approximately 1.25m, it may be seen that the distance to separation appears to have reduced, reducing pressure drag. These distances are estimates and the actual drag reduction verified by analysing the induced translational drag.

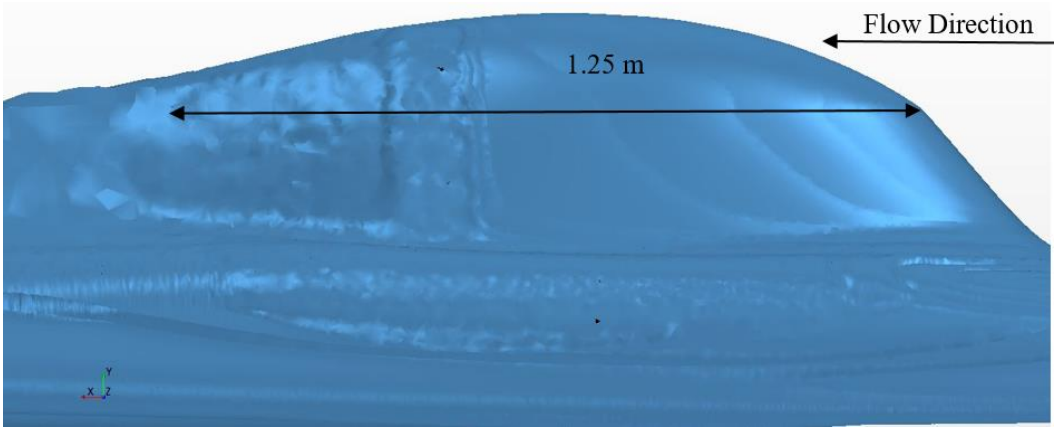

Figure 4-41: TKE iso-surface, VG's further forward (concept three).

As can be seen from the illustrations, the canopy with no vortex generators attached has an airflow laminar over most of the length of the canopy. The canopy with vortex generators applied, however, has slightly increased turbulence at and after the vortex generator placements. The separation point is further down the canopy as opposed to not having vortex generators on. This, in turn, decreases the overall pressure difference across the canopy and thus reduces the drag applied to the car. The VGs are more effective when crosswinds are present, which is needed as there will likely be crosswinds applied in real world conditions throughout a greater portion of the vehicle's lifespan.

Wall Y+ illustrated

Figure 4-42 shows a wall y+ scalar plot applied to the vehicle model with no vortex generators applied.

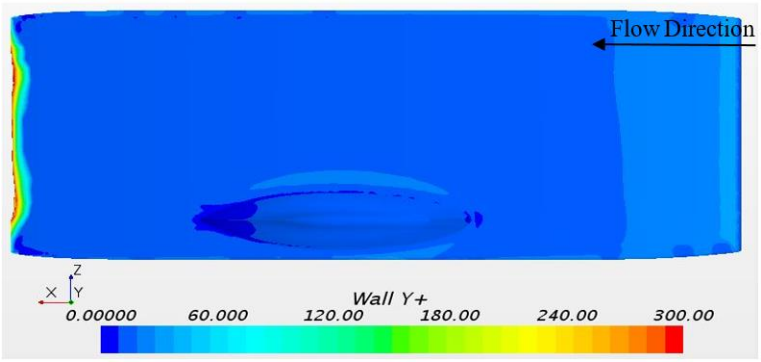

Figure 4-42: Wall Y+ for validation, no VG's.

In order to ensure acceptable results and conventions, a wall y+ plot is required with a wall y+ range from 0 to 300 due to the turbulent nature of the fluid flow applied by the vortex generators as well as wheels. Figure 4-43 shows the wall y+ on the car surface with vortex generators applied.

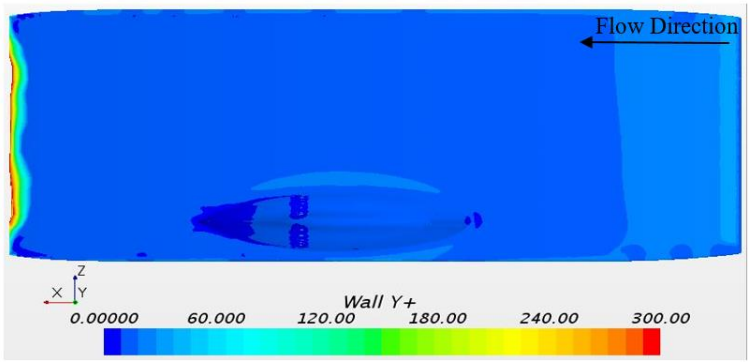

5

Figure 4-43: Wall Y+ for validation, VG's further forward (concept three).

When comparing Figure 4-42 to Figure 4-43. It may be noted that the wall y+ increased slightly over the vortex generators, which was expected. The range is shown to be true over the vehicle surface and thus the comparisons taken as acceptable for comparison purposes.

4.4. Manufacturing and Implementation

This section explains the manufacturing processes and materials used in the manufacturing of successful flow alteration devices. The associated drawings are found in Appendix C.

4.4.1. Wheel covers

The manufacture of the smooth covers was a simple task while the application to the wheels was slightly challenging since the covers were not allowed obstruct the suspension, braking, and steering systems, and needed to be easily removable. The covers were manufactured as simple flat discs of carbon fibre lay-up with the fibres oriented in 0-90 and 45-45 degree directions. In order to position the mounting holes accurately, large paper templates were printed and bonded onto the carbon discs. Holes were then drilled and simple sizing adjustments performed because of manufacturing tolerances in order for the covers to fit on the wheels seamlessly while not hindering the wheel, brake and steering assembly. The discs were then cut on a single line from the inner to the outer diameter to form cones, and glued on this line in a cone shape. The cone shape allowed for a more accurate and tighter fit to the wheel itself. When applying the wheel covers to the wheels, ease of removal was essential; considering that the mounting would be behind/within the shrouds, the mounting structure would have to be removed with relative ease. Quarter turn bolts were considered but deemed unusable because of the spatial constraints in tooling application for quick removal of the covers.

Cable ties were applied in a manner that would not significantly affect the airflow. The cable tie mounting areas were, as mentioned, covered by shrouds as the mounting holes were placed near the wheel axle while the outer edges of the covers were mounted with extremely strong VHB double-sided tape to achieve flush mounting. This was done so that the small area protruding beneath the shroud, which was the main area for the altering of the incident airflow, was covered in a manner which allowed effective airflow alteration to potentially reduce the overall aerodynamic drag. The cable ties held the inner cover onto the outer cover which was placed on the outer side of the wheel; the low curvature side is explained in Section 3.2.1. This allowed for easy removal of the wheel from the car. The assembly technique proved to hold for race conditions and did not fail. The manufacture of dimpled wheel covers would have been expensive with respect to monetary costs as well as time and was not justified because of the negligible aerodynamic efficiency effects compared to smooth wheel covers in CFD analysis. If one takes into account the slight error that usually occurs in simulations, the change in aerodynamic efficiency would not be guaranteed by using dimpled wheel covers, though further design optimisation and testing would aid in this observation. Testing of further iterations of dimple designs on wheel covers, may however not aid the design process because smooth covers have advantages regarding ease of manufacture and the resources required for dimpled covers are higher than for manufacturing smooth covers. The completed carbon fibre inner wheel cover is shown in Figure 4-45, and the wheel cover manufacturing details can be seen in Appendix C1. The inner and outer wheel covers were identical although the outer and inner diameters differed.

Figure 4-45: Inner wheel cover.

The implementation effectiveness of the wheel covers and their implementation in the solar vehicle is shown in Figure 4-46.

Figure 4-46: Wheel cover applied to solar vehicle – outer diameter of rim.

Figure 4-46 shows the smooth finish on the outer diameter of the rim where the wheel cover is held to the rim. The cable ties used are covered by the wheel shroud and thus do not affect the incident airflow as much as the outer diameter of the rim. Figure 4-46 also shows the space beneath the shroud where the wheel affects the airflow which caused the turbulence mentioned; this was mitigated by implementing the smooth wheel covers shown.

4.4.2. Vortex Generators

Preliminary designs of vortex generators were manufactured via 3-D printing using ABS plastic. Vortex generators were not applied to the vehicle itself and thus the actual implementation was not documented other than in CFD testing. The CAD model figures as presented in Section 3.3 and Appendix C2 show the accurate geometry of the vortex generators.

4.4.3. NACA Duct

The NACA duct was manufactured via 3-D printing using ABS plastic. Once the NACA duct was printed the surface finish was improved with fine sand paper. The NACA duct was then bonded, using a product called Crestabond, to a hole in the canopy base at the chosen location specified in Section 3.4.1 and illustrated in Figure 4-47. The drivers of the solar vehicle confirmed that the duct performed sufficiently well as ventilation and thus cooling occurred at all speeds that the solar vehicle encountered (Leverone, 2015), (Sinclair, 2015), (Singh, 2015), (Veale, 2015). The CAD representation of the duct is shown in Section 3.4 and Appendix C3. In comparison to other race vehicles, the placement and sizing of the NACA duct on the canopy showed similar trends.

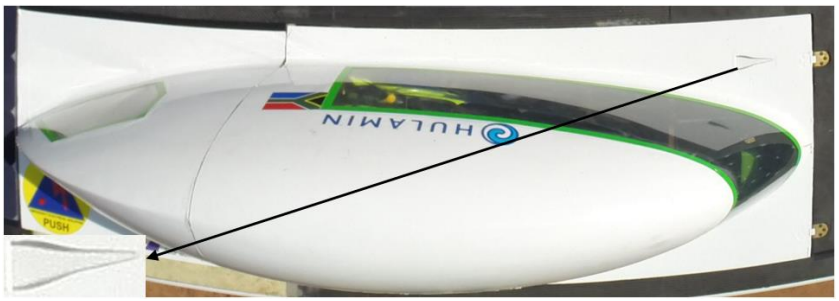

Figure 4-47: NACA duct applied to solar vehicle canopy.

CHAPTER FIVE: DISCUSSION

5.1. Overview

Optimising the aerodynamics of the solar vehicle was of vital importance since the aerodynamic losses are directly related to the vast majority of losses experienced in a solar vehicle race. It was proposed that the aerodynamics of a solar vehicle may be improved without modifying its bulk geometry. This was to be done by adding flow alteration devices which do not hinder the vehicle operation in any way while adhering to the regulations for the races and remaining within the bounds of the resources available to the project.

The potential use of trip wires, cowlings, vortex generators and dimpling was proposed, and the use of these devices was also limited by potential areas of application as well as design implementation and time constraints; streamlined areas such as the thin, cambered top shell would not allow for their application because the resulting aerodynamic drag reduction may be deduced from Section 2.3.5. The CFD results were to be verified by experimental testing, however, this was not possible due to lack of time as a result of restrictions and preparations for the WSC and SASC races.

Certain design strategies were shown via CFD to improve the aerodynamics of the solar vehicle but not all of them were tested due to time constraints and other practical concerns. The improvement of the aerodynamics via these devices proved to yield results comparable to similar ones found in the literature (see Sections 2.3, and 2.5 to 2.7). However, the solar vehicle is principally a streamlined body, while the literature covers for the most part bluff bodies. Areas such as the canopy and wheels are taken as bluff bodies because of the turbulence they cause and their curvature; in other words the application of principles derived for bluff bodies were applied to these parts of the solar vehicle. Streamlined areas of the vehicle were not considered as areas where optimisation would result in significant reduction in aerodynamic drag, and so design and application to these areas was not justified.

The use of dimples and vortex generators was considered due to the findings in Section 2.3, and the literature which investigates the application of dimples and vortex generators to shapes similar to the wheels and the canopy. To potentially increase the skin friction resulting in a reduction in the adverse pressure gradient, the flow alteration devices mentioned were iteratively designed and tested. Skin friction may be reduced by the use of smooth wheel covers, but increased by the dimpled wheel covers and vortex generators. The Zipp wheels bear a direct relation to solar vehicle wheels while the Garneau helmet and the application to aerofoils have a direct relation to the solar vehicle canopy (Cyclery, 2007), (Garneau, et al., 2009), (Hua, et al., 2007).

To find the most viable airflow alteration device, the literature was reviewed to provide insight into the properties of boundary layer airflow, and most importantly, how turbulent airflow is less susceptible to separation than laminar airflow. The concept of tripping airflow into a turbulent regime was consequently studied. This spurred a need to find devices that would trip airflow efficiently without causing net losses to occur, or to find devices that reroute the airflow onto the surface allowing the airflow to become re-attached. Vibrating the airflow at certain frequencies was also investigated encourage re-attachment, and to alter the near-wall boundary layer airflow by matching the natural frequency of the airflow, causing it to re-attach. These devices or techniques all aim to alter the near-wall boundary layer airflow while in turn having a positive effect on either reducing skin friction or more commonly reducing the size of the separation region and allowing a net reduction in aerodynamic drag. Causing turbulence at the correct position on the body in question allows for airflow to separate further down the body thereby increasing skin friction but reducing the net pressure difference between the leading and trailing edges of the body. This can result in a net reduction in aerodynamic drag as discussed. Many devices were analysed for effective usefulness on the solar vehicle and through the use of a selection matrix in Table 2-3, dimples and vortex generators were considered for application to the canopy and wheels. The effectiveness of such devices is directly dependent on the surface geometry on which they are applied.

Vortex generators might have been beneficially applied to other parts of the vehicle, but it was decided to focus on sections of the car with the most apparent optimisation potential. Wheel covers mitigate the turbulence caused by the wheel spokes and the vortex generators trip airflow to delay separation and hence reduce net aerodynamic drag. The solar vehicle was discretised to only capture relevant areas for CFD optimisation. This reduced computational time and the resources needed for acceptable comparisons to be made.

The review of previous applications of dimples and vortex generators provided insight into optimal dimple and vortex generator sizing. Firstly large dimples were designed and coarse meshes used to allow for testing in a reduced time frame so that the preliminary analysis of dimple application was analysed for potentially desirable airflow alteration characteristics. Thereafter fine dimples were designed for accurate testing of the sizing found through an analysis of the literature in Section 2.3.1. Vortex generators were designed based on literature for their application to aerofoils, as outlined in Section 2.3.5, since the solar vehicle aerodynamic shape was designed almost entirely utilising aerofoil forms. The designs needed to be tested and manufactured to be applied to the solar vehicle for the SASC and the WSC races which placed time and monetary constraints on the project

The major challenge was to test the airflow accurately enough so that the boundary layer flow and its alterations could be captured. To do this computationally, the predicted prism layer properties for each part of the vehicle were found by calculating the boundary layer properties as explained in Section 3.5. This was done using fundamental theory commonly used in fluid dynamics as described in Chapter 2, Section 2.2, which aided the CFD model definition for accurate testing to be conducted. The next major challenge was to allow for the capture of the CAD geometry in the fluid domain which required geometry simplification in most cases, such as the wheel cover testing model which tested the effectiveness of the wheel covers as described in Section 3.2.2.

An efficient way to find the best methods to improve the aerodynamics through the use of such devices, was to iteratively test and compare devices found in the literature, as proposed in Section 2.3. CFD modelling involved comparisons only, and these were run in sets with the same mesh sizes and types, physics details and boundary conditions applied. Mesh independence was reached by running the sets at different meshes for accurate comparisons and potentially reducing the need for experimental testing. In analysing the alteration devices through CFD testing, it was apparent that it is essential for mesh independence to be reached before the results could be accepted. Mesh independence was attained but may not have been investigated to the extent that large industrial projects might, where vastly larger computational resources are easily accessible. Thus two or three mesh iterations were performed until the trend showed with acceptable certainty that the models were mesh independent. This is shown, for example, in Section 4.2, Figure 4-23 for the wheel models. The canopy results were similar with regards to meshing techniques and mesh independence as shown in Sections 3.5.2 and 4.3, and mesh independence is deduced from the results shown in Appendix B. Mesh independence should ideally be shown for differing mesh sizes until mesh independence is clearly reached and show results which may be claimed as independent od the mesh sizing and element count in the mesh.

Testing the concepts involved the use of a virtual wind tunnel that was sized to allow for mitigation of the blockage effect commonly experienced in such testing methods. CFD results of the tested devices, namely the wheel covers and vortex generators, enabled the effects of these devices on the aerodynamics of the solar vehicle to be quantitatively assessed. Uncertainty and error were accounted for by analysing the results, and if the results differed by too small a margin, the aerodynamic effects were taken as indefinite error in CFD modelling may also have occurred as a result of the wheel testing fluid domain having not been made higher, or that the upper surface of the fluid domain did not have a similar shape to the lower side of the top shell as would be apparent when driving the solar vehicle.

This may have caused flow acceleration next to the shroud. The effects of this were taken into account by incorporating uncertainty in the result analysis plots and in the discussions conducted in Section 4.2. A larger fluid domain was also constructed for a refined wheel testing fluid domain so that the blockage effects were mitigated. This resulted in more accurate plots and values to be investigated and compared.

The flow split CFD model outlined in Section 3.5.3 may have been the best alternative CFD modelling methodology to be used for final validation of the flow alteration devices. This model would incorporate the wheel covers, canopy vortex generators and the NACA duct simultaneously. This was however not done because of insufficient time and computational resources. The methods involved in this type of testing were briefly investigated. In order for larger models to be tested, more powerful computers would have been essential to accurately and simultaneously capture internal geometry along with wheel rotation, NACA duct, vortex generator, and wheel cover implementation. With the available resources the accuracy, run-time, model sizing, mesh independence and error may have been compromised and the results analysis would have been hindered by a large amount of uncertainty.

5.1.1. Wheels – Covers

(Design described in Section 3.2 and testing and analysis described in Section 4.2)

Several wheel cover concepts, as described in Section 3.2.1, were designed while only four were effectively tested.

Wheel cover implementation overview

The solar vehicle fluid domain was discretised to capture only the wheel aerodynamics for this testing set. This incorporated the right front wheel and the accompanying shroud section as described in Section 3.2.2 and illustrated in Figures 3-5 to 3-7. The wheels were set to rotate at the speeds shown in Appendix A4 since the main testing speed was chosen initially at 70 kph for the anticipated average race speed as decided upon by the race strategists. The CFD models were set-up as shown in Section 3.2.2, Figures 3-8 and 3-9. The potential drag reduction to be achieved by reducing the turbulence caused by the wheel spokes was the main reason for applying wheel covers. If the wheel shrouds had covered the entire wheel surface, the aerodynamic drag reduction potential from spoke covers would have been assumed to be substantially smaller however approximately a quarter of the wheel protruded beneath the wheel shroud. Figures 4-4 to 4-7 show that the meshes used were fine and of acceptable quality to allow for the capture the geometry and fluid domain. Figure 4-4 and 4-5 show the actual meshes and the increased mesh number in the vicinity of the wheel as well as the entire fluid domain. Figures 4-6 and 4-7 illustrate the higher mesh quality when the finer mesh was applied.

While analysing the results in Section 4.2, it was noted that in testing the uncovered wheels, it was assumed that a large amount of turbulence and swirling may occur within the shroud principally because the wheels protrude through the holes beneath the shrouds. This was most likely due to the sweeping action of the wheel spokes. Based on this preliminary analysis, the implementation of smooth wheel covers was proposed to mitigate the turbulence caused by the spokes.

Detailed wheel cover implementation discussion

The use of convex covers which add frontal area to the wheels themselves was considered for further reducing drag. Convex outer covers were assumed to have potential aerodynamic drag reduction effects because only a small area of the wheels protrude beneath the underside of the shroud. The addition of convex wheel covers would possibly result in mitigation of turbulence as well as smoother airflow over the wheels. This was not tested because of spatial constraints in the shroud applied by mechanical systems as well as constraints for turning circle requirements; the convex covers would thus hinder the movement of the wheel in such a way as to touch the shrouds, not allowing for the turning requirements to be met.

The values analysed in Section 4.2, Table 4-1, with regards to translational and rotational forces show that there was a larger reduction in energy input to rotate the wheels and propel the vehicle forward by the addition of smooth covers. Uncertainty, simulation error and safety factors were incorporated into the drag and torque values. The application of dimpled wheel covers was merited since it potentially enabled a further reduction in aerodynamic drag by controlling the magnitude of the turbulence induced by the smoothly covered or uncovered wheels, seen in Figures 4-8 and 4-10. The nature of this turbulence could be controlled by the application of dimples to the wheel covers while also controlling the swirling and sweeping of air into the interior of the shroud. It was established that the turbulence and swirling effects were reduced within the shroud and around the wheel which was shown by a reduction in translational and rotational forces for both smooth and dimpled wheel covers applied. Smooth wheel covers reduced the net drag by a larger amount than dimpled wheel covers.

The preliminary results analysed in Figures 4-8 to 4-10 showed potential for aerodynamic drag reduction, and further testing of the wheel covers was justified because turbulence and swirling were reduced when analysing the streamline and TKE plots. Although adding dimples to the wheel covers may reduce drag the dimple design tested did not yield a gain in aerodynamic efficiency when compared to the smooth wheel covers, seen in Table 4-1. Dimpled wheels tripping airflow might with necessary accuracy reduce drag by delaying separation, but the application of such techniques can only be accomplished through further testing and optimisation of the applied devices.

Drag reduction potential via dimples was observed by higher vorticity and turbulence values being apparent which may have encouraged separation to occur at a later stage. Reduced turbulence resulted from covering the rotating wheel spokes because the spokes then did not come into contact with the incident airflow. To verify whether turbulence is indeed reduced when comparing uncovered wheels to covered wheels, turbulent kinetic energy values were analysed as shown in Figures 4-11 to 4-16. These plots incorporated preliminary testing methods as well as refined testing. The preliminary testing shows closely similar results to the refined testing methods in the analysis of the plots. The turbulent kinetic energy was lower when the wheels were smoothly covered or had dimples, compared to uncovered wheels.

Reduced swirling is apparent when comparing velocity plots as shown in Figures 4-17 to 4-19. Swirling was shown to be reduced for covered wheels compared to uncovered wheels while dimpled and smooth covers showed similar flow patterns. Refined testing showed that swirling and turbulence were only notably reduced by the addition of smooth wheel covers and not further reduced by the addition of dimpled wheel covers.

To gain insight into whether the airflow was indeed separating and after further analysis of the effectiveness of the wheel covers, Figures 4-20 to 4-22 show wall shear stress plots. These plots show that the wall shear stress on the wheel itself is of a similar nature whether for smooth or dimpled wheel covers, however, the stress in an analysis of uncovered wheels seems to be lower on the spoke ends and thus supports the assumption that the air was completely detached from the wheel spokes. This may imply that the smooth wheel covers allow better, more laminar attachment of airflow and thus reduction in overall drag.

Concepts one, two and three described in Section 3.2.1, being smooth, coarsely and finely dimpled, respectively, proved to reduce the drag caused by the wheel spokes effectively. Concepts four to seven involved deeper, shallower, convex and one-sided covers, respectively, and were not tested due to time and added complexity (added run-time due to wheel rotation and interior volume adding sharp edges and detail), with the size of the potential CFD models causing large delays.

The implementation of the smooth wheel covers to the solar vehicle wheels proved successful as they were applied and removed with ease while allowing for the unimpeded functioning of the mechanical systems near the wheel. Smooth wheel covers were applied to the wheels using VHB double sided tape for the outer edge attachment while cable ties were used near the wheel axle to hold the inner cover to the outer cover with the spokes between the covers.

5.1.2. Canopy – Vortex Generators

(Designs are shown in Section 3.3 and a result analysis is shown are shown in Section 4.3)

Three vortex generator concepts were envisioned as described in Section 3.3 although only two designs were modelled and tested.

Vortex generator implementation overview

The concepts involved used common, existing vortex generator geometries while the placement thereof comprised a critical design factor. When analysing the placement as a critical design factor, the geometry of the vortex generators was kept consistent and its placement was used to construct different conceptual designs. Concept one included no VG's, concepts two and three involved different placement of the vortex generators with respect to the separation point found through CFD testing.

The solar vehicle fluid domain was discretised to capture the rotating wheels and the entire car, while the final models incorporated only the canopy and top shell for comparison purposes. Section 3.3.2 describes the simplification of the CAD geometry in order for the fluid domain to allow for accurate analysis of the airflow characteristics used. In order to reduce error in results and simulations, the CFD models were constructed so that the canopy and relevant surroundings were captured by mesh structures and physics details specified as explained in Sections 3.5.2 and 3.5.4 so that the airflow characteristics may allow for accurate analysis. Meshing and physics details were assigned so that convergence criteria could be met. Post processing of scalar plots such as wall y+ as discussed in Section 4.3.3 was conducted to verify the accuracy of the CFD models. As envisioned, the vortex generators tripped the airflow and hence delayed separation, thus increasing skin friction but also beneficially increasing the distance between the leading edge of the canopy and the point of separation. The net effect was a reduction in aerodynamic drag.

Detailed vortex generator implementation discussion

When investigating the effects of rotating wheels on canopy aerodynamics as described in Section 4.3 and illustrated in Figures 4-25 to 4-30, it was found that the rotating wheels had no significant effect on the turbulent kinetic energy, pressure and streamlines of the canopy aerodynamics. These tests justified modelling of only the canopy and top shell to reduce the runtime of the simulations to analyse the aerodynamic effects of vortex generators.

To illustrate the idea of a separation pattern on the solar vehicle surface, a commonly used convention (De Wet, 2013) is to set the turbulent kinetic energy to a maximum value of 0,1 J/kg which allows for the display of an iso-surface with this limit applied, as shown in Figures 4-31 and 4-32. The iso-surface was used as a tool to visualise the airflow patterns over the vehicle surface. The TKE was plotted on the surface to show turbulence patterns on the car. When measuring the distance to the separation point from the canopy leading edge, origin reference points were chosen and kept consistent to compare the distance to a separation point on the smooth canopy surface to that of the canopy with vortex generators applied to it.

A wall shear stress distribution was used to visualise the point at which the shear stresses are reduced to near zero in order to delineate turbulence regimes as well as skin friction magnitudes on the body surface. The separation region is likely to begin at the point where wall shear stress is drastically reduced to a value near zero. The airflow may have separated as the flow is no longer attached to the surface but rather swirling which results in lower pressure as explained in Section 2.1.5 and shown in Figures 4-33 to 4-35. Separation may therefore increase as wall shear stress drastically reduces. It is noted that the wall shear stress increases at the region where vortex generators are applied and also closely downstream from the vortex generators, thereafter drastically decreasing at a certain distance from the vortex generators. The airflow then seems to separate and this may result in turbulence increasing the skin friction near the vortex generators. The airflow separates when the adverse pressure gradient reaches the necessary conditions for separation to occur as described in Section 2.1.5.

It can be seen in Figures 4-33 to 4-41 that the separation region was delayed when adding vortex generators to the canopy while turbulence was increased as a result of the near wall airflow tripping by the vortex generators. If the vortex generators are placed further forward on the canopy the drag is more substantially reduced than when placed further back since this placement allows for further distance to the separation region and thus a greater reduction in resulting drag forces. Section 2.3.5 outlines the application of vortex generators to several bodies while Section 2.3 outlines several methods for similar techniques; the results analysed in Section 4.3 show that the application of vortex generators indeed trips the airflow effectively, thereby reducing net drag on the system by delaying separation. The associated increase in skin friction has less influence than the reduction in pressure.

An analysis of the turbulence intensity distribution as applied to the canopy in Section 4.3 illustrated in Figures 4-36 and 4-37, shows that the plots may be somewhat misleading; with the vortex generators applied it shows apparently lower turbulence values.

This is not the case; if we compare the overall and peak turbulence values, it shows that the application of vortex generators increases overall near wall turbulence. If the skin friction over the canopy surface is analysed we see that there is increased skin friction when the vortex generators are further forward on the canopy. Similar trends are shown in Figures 4-34 and 4-35 to those in Figures 4-38 and 4-39.

Further analysis of the effectiveness of the vortex generators was conducted by only analysing result plots and values incorporating vortex generators applied nearer the canopy leading edge (concept three). This was compared to having no vortex generators since this application technique was found to be effective at reducing net drag. Vortex generators applied further away from the canopy leading edge were estimated to reduce drag when analysing Figures 4.34 and 4.35. Having vortex generators applied further back (concept two) was not included in the analysis because the prior analysis conducted in Section 4.3 showed that its effect was inferior to the concept incorporating them further forward.

When analysing separation as illustrated by an iso-surface set to display a maximum of 0,1 J/kg as seen in Figures 4-40 and 4-41, the turbulent kinetic energy on the smooth canopy and canopy with vortex generators applied nearer the leading edge (concept three), it shows that the distance to the separation region from the canopy leading edge has been increased and thus separation has been beneficially delayed. The separation region is delayed by approximately 0.16 metres as shown when comparing Figures 4-40 to 4-41. It may also be seen that the turbulence increases at the point where the vortex generators are applied. The increase in distance to the separation region directly affects the size and magnitude of the low-pressure region. As explained throughout Chapter 2, the reduction in the separation region and thus the low-pressure region size and magnitude, results in a reduced pressure difference between the leading and trailing edge of the canopy which reduces translation drag.

To ensure that the CFD models conducted were of acceptable accuracy, wall y+ plots incorporating the condition of having values less than 300 and more than zero were compared, as required by the k-Omega turbulence model discussed in Section 2.2.8. This was used as a convention due to turbulent flow normally having values ranging from 0 to 300 when accounting for the all y+ solver regimes chosen. Figures 4-42 and 4-43 show that the models were within the desired y+ range and thus the testing of the vortex generators was considered accurate for comparison purposes and for final trends to be established as discussed in Sections 4.3 and in this section. Wall y+ values were noted as higher on the vortex generators and thus the turbulence was shown to be higher in this region as well. The airflow speed was reduced near the trailing edge of the canopy, showing slower airflow and thus a likely separated region due to the reduced wall y+ values.

The results show that vortex generators can be applied to reduce the net aerodynamic drag and thus increases aerodynamic efficiency in a solar vehicle. They alter turbulence characteristics. The most efficient way to manufacture the vortex generators was to have them 3D-printed and bonded to the canopy's outer surface. These were however not applied to the canopy for the 2015 WSC due to incomplete CFD results at the time of the race.

5.1.3. NACA Duct

(Designed in Section 3.4 with results and analysis in Sections 4.3 and 4.4)

Separate driver ventilation was essential for the WSC and not the SASC due to changing the canopy shape for the WSC. This necessity was only discovered shortly before the WSC race and thus a ventilation device could not be optimised via CFD as time constraints were applied to the design process. The race rules stated that there had to be a method of ventilation incorporated into the vehicle design for driver comfort and endurance. The most aerodynamically efficient way to allow for this was to add a NACA duct. The duct was not to be designed as a flow alteration device to reduce drag but rather a device used to redirect air into the driver cockpit as per race the regulations.

A NACA duct is an efficient way of allowing transfer of airflow from one side of a body to the other, usually applied to automotive vehicles and aeroplanes. It was designed using the available literature discussed in Chapter 2, Section 2.3.10, which takes into account placement with regards to boundary layer characteristics. The design had to be completed in a short time and thus optimisation was not possible with regards to sizing and positioning. The analysis of a rectangular hole by CFD analysis was first performed since the addition of a hole is essentially a less efficient method of allowing air to pass from the exterior of the car to the interior as discussed in Section 2.3.10. The effect of the rectangular hole is shown in Figure 4-47. The negligible effects due to the addition of this hole were unexpected although the model should be further tested incorporating a finer mesh sizing with regards to surface meshing applied as well as the actual NACA duct having to be implemented into CFD model. Detailed testing was not done for an accurate comparison to be performed because the NACA duct was urgently needed for the WSC race. To conduct more accurate testing of the actual NACA duct through the use of CFD modelling, a flow split CFD model, as explained in Section 3.5.3, may be necessary. The complexity added to the design and testing process when developing the duct may not permit such methods.

The NACA duct was 3-D printed and successfully bonded to the canopy at the chosen location specified according to the methods outlined in Sections 2.3.10 and 3.4.1.

Experimental testing of the duct was performed during the pre-WSC solar car testing and it was concluded that it would allow for driver ventilation and would pass race regulations. The drivers of the solar vehicle for the WSC reported that the duct supplied ventilation to a sufficient degree (Leverone, 2015), (Singh, 2015), (Sinclair, 2015), (Veale, 2015).

CHAPTER SIX: CONCLUSION

This project aimed to enhance a solar vehicle's aerodynamics without altering its bulk geometry. The work yielded positive results with respect to the chosen and tested designs. Many airflow alteration techniques were investigated, namely dimples, trip wires, riblets, vortex generators, suction, blowing, FCSD and acoustic emissions. Smooth and dimpled wheel covers and canopy vortex generators were selected as the most viable potential improvements. Though most of the tested devices improved the solar vehicle aerodynamics, not all the devices proved to do so by amounts large enough to justify manufacture and application to the vehicle. Error in the models was reduced where possible while accuracy and validity of comparison was ensured throughout the design process. Comparison accuracy was ensured by having acceptable mesh independence throughout the CFD models, having identical mesh and physics details for each of the compared models, and by remaining aware of model accuracy and error. Each device was tested separately and each device's effectiveness investigated. Some of the designed devices were manufactured and implemented on the solar car for the SASC and WSC, thus design completion was performed accurately and timeously.

The devices chosen for design and testing were smooth wheel covers, dimpled wheel covers, vortex generators and a NACA duct. A feasibility analysis and optimised CFD methods are described in Chapter 3. The aerodynamics of the solar vehicle was improved via smooth wheel covers while dimpled covers were not implemented because the aerodynamic gain was to be smaller than the smooth. The smooth wheel covers reduced the vehicle's drag by reducing the translational and rotational forces. However, dimpled wheel covers showed positive results in reducing aerodynamic drag (translational and rotational) relative to having uncovered wheels.

The vortex generators were designed based on existing designs, but their placement was thoroughly studied and it was found that it was beneficial to position them in the forward most position tested. They proved to reduce the separation region in the wake of the canopy, thus reducing the net aerodynamic drag experienced by the solar vehicle effectively. The vortex generators increased the turbulence, shown by an increase in skin friction in the vicinity of the vortex generators therefore reducing the separation region size and magnitude. The net reduction in drag justifies the reasoning outlined in the literature, in Chapter 2, namely that tripping the airflow early can beneficially increase the distance to the separation region.

While achieving improved aerodynamics via two devices, an aerodynamic driver compartment air-inlet was designed without CFD optimisation of the design. It was instead designed according to the designs described in the literature based on previous applications.

The air inlet device was a NACA duct which was not fully optimised by CFD methods due to time constraints for the WSC, but experimental testing before and during the race showed that the duct served its purpose of providing ventilation to the driver cockpit. Whether the design was fully optimised with regards to size and placement is questionable; this would have to be verified through further investigation, probably using a flow-split model. Further investigation was not possible for timely results to be achieved before the WSC. The duct was manufactured in adherence to the race regulations and provided sufficient driver comfort.

To gain insight into the total aerodynamic efficiency improvement provided by the combined effects of the implemented devices, a CFD model incorporating the wheel covers, vortex generators and NACA duct is possible. To conduct a quantitative analysis of these effects, more powerful computing resources would be necessary for fully resolved, mesh independent and accurate results. Further optimisation of the dimpled wheel covers, vortex generators and NACA duct is possible through further design iterations and testing. Ideally the CFD results would be compared to experimental wind-tunnel testing. However this was not possible within the current project budget and time. Design objectives were met within the project constraints.

Optimisation of streamlined and bluff bodies is thus possible if the boundary layer airflow is altered to reduce net aerodynamic drag. This methodology may be applied to many areas of potential optimisation such as aircraft, vehicles, and aquatic devices. Improved aerodynamics may be achieved by adding flow control devices. The shape and size of these devices as well as their location may be optimised by intensive CFD modelling.

The degree of testing performed using CFD analysis was shown to be accurate for purposes of the project. The results resolved the necessary airflow characteristics required by the design objectives. Convergence criteria were adhered to and acceptable mesh independence was attained in all the CFD models. Techniques used for testing more complex geometry, mathematical principles to construct the testing techniques, uncertainty in analysing results, and error involved in CFD testing were investigated, and applied. This successfully allowed improvement of the solar vehicle aerodynamics.

REFERENCES

© CFturbo® Software & Engineering GmbH, n.d. *cfturbo.com.* [Online] Available at: http://en.cfturbo.com/fileadmin/content/manual_cfturbo2icem/global_prism_parameters.htm [Accessed 25 August 2016].

Ahmed, H. & Chacko, S., 2012. *Computational optimzation of vehicle aerodynamics.* Vienna, DAAAM International, pp. 313-318.

Aoki, K., Muto, K., Okanaga, H. & Nakayama, Y., 2009. Flucome. *AERODYNAMIC CHARACTERISTIC AND FLOW PATTERN ON*, pp. 1; 4-6; 8-10.

Bakker, A., 2006. *Boundary Layers and Separation.* s.l.:Fluent Inc.

Bez, D., 2012. *Hexa solar car.* Italy.

Butt, U. & Egbers, C., 2013. Aerodynamic Characteristics of Flow over Circular. *International Journal of Materials, Mechanics and Manufacturing,* Volume 1(No 2, May 2013), pp. 1-5.

Campenhou, O. v., Nesselrooij, M. v. & Veldhuis, L., 2016. *Flow visualization over drag reduction dimpled surfaces in turbulent boundary layers using Particle Image Velocimetry.* Delft, Delft University of Technology.

Carbonne, L., Winkler, N. & Efraimsson, G., 2016. Use of Full Coupling of Aerodynamics and Vehicle Dynamics for Numerical Simulation of the Crosswind Stability of Ground Vehicles. *SAE International Journal of Commercial Vehicles,* 125(2EJ), p. 12.

CD-Adapco, 2013. *STAR Koren Conference.* Seoul, CD-Adapco.

CD-Adapco, 2014. STAR-CCM+ Userguide. In: *Userguide.* s.l.:Cd-Adapco, pp. 3477-3481.

Celik, I. B., Ghia, U., Roache, P. J. & Freitas, C. J., n.d. *Procedure for Estimating and Reporting of Uncertainty Due to Discretization in CFD Applications,* Morgantown: West Virgina University.

CFD Online, 2011. *CFD Online.* [Online] Available at: http://www.cfd-online.com/Forums/fluent/90281-convergence.html [Accessed 2015].

Chklovski, T., 1985. *Wings with pointed tip wings at low Reynolds number,* Los Angeles: University of South California.

Cimbala, Y. C. J., 2014. *Fluid Mechanics, Fundamentals and Applications.* 3rd ed. New York: McGraw-Hill Companies, Inc.

Coppin, P., Ayotte, K. & Steggel, N., 2003. *Wind resource assessment in Australia - a planners guide,* Australia: CSIRO Wind Energy Research Unit.

Copyright Commonwealth of Australia 2016, Bureau of Meteorology , 2015. *Australian Government Bereau of Meteorology.* [Online] Available at: http://www.bom.gov.au/climate/mwr/ [Accessed 25 April 2015].

Cyclery, Z., 2007. *ZIPPS' wind-tunnel test* [Interview] (June 2007).

De Wet, C., 2013. *Computational Fluid Dynamics "Expert"* [Interview] (04 2013).

Dol, D. S. S., 2013. *Eighth Curtin University of Technology, Science and Engineering (Cutse) International Conference.* Sarawak, Curtin University.

Dumas, L., 2008. CFD-based Optimization for Automotive Aerodynamics. In: D. Thévenin, ed. *Optimization and Computational Fluid Dynamics.* Berlin: Springer Berlin Heidelberg, pp. 191-214.

Ekman, P., Gardhagen, R., Virdung, T. & Karlsson, M., 2016. Aerodynamics of an Unloaded Timber Truck - A CFD Investigation. *SAE International Journal of Commercial Vehicles,* 125(2EJ), p. 7.

Fletcher, T. et al., 2014. *Hydrodynamics of fossil fishes,* Durban, KwaZulu-Natal: The Royal Society.

Fox, R. W., McDonald, A. T. & Pritchard, P. J., 2012. *Fluid Mechanics, International Student version, 7th Edition.* 7th ed. Durban: Wiley.

Fox, R. W., Pritchard, P. J. & T.McDonald, A., 2012. Fundamental Concepts. In: *Introduction to Fluid Mechanics.* s.l.:John Wiley & Sons Inc., pp. 40 - 42.

Frick, C. W., Davis, W. F., Randall, L. M. & Mossman, E. A., 1945. *An experimental investigation of NACA submerged-duct entrances,* Mountain View: National advisory committee for aeronautics.

Garimella, R. V. & Shephard, M. S., 2000. Boundary layer mesh generation for viscous flow. 49: 193-218(International journal of numerical methods in engineering), p. 201.

Garneau, L., Gingrs, D. & Hamel, D., 2009. *Cyclist Helmet.* Canada, Quebec, Patent No. USD595903 S1.

Gença, M. S., Kaynakb, Ü. & Yapici, H., 2011. Performance of transition model for predicting low Re aerofoil flows. *Performance of transition model for predicting low Re aerofoil flows,* pp. 1-4; 8-18.

Groth, C. P. T., 2014. *http://arrow.utias.utoronto.ca*. [Online] Available at: http://arrow.utias.utoronto.ca/~groth/aer1310/Lecture_Notes/1_Intro_Turbulent_Flows.pdf

Hall, C. F., 1948. *An experimental investigation of NACA submerged inlets at high subsonic speeds 1: Inlets forward of the wing leading edge,* Mountain View: National Advisory Committee for Aeronautics.

Hilbert, B. F., 2011. *Drag Reduction on Aerodynamic Shapes with Ground Effect,* New York: Clarkson University.

Hosder, S. et al., 2003. *Remarks on CFD simulations uncertainties,* Blacksburg: Virginia Polytechnic Institute & State University.

Hua, S. et al., 2007. *Numerical study of passive and active flow separation control,* Fort Worth: University of Texas, Arlington.

Incopera, F. P., DeWitt, D. P., Bergman, T. L. & Lavine, A. S., 2007. *Fundamentals of Heat and Mass Transfer 6th Edition.* 6th ed. Hoboken: John Wiley & Sons, Inc.

Kuzman, D., 2016. *Introduction to Computational Fluid Dynamics,* Dortmund: University of Dortmund.

Lawrence, C., Moosa, F., Nkosi, S. & Moodley, T., 2013. *Design of a solar powered vehicle,* Durban: University of KwaZulu-Natal.

LEAP Australia, 2012. *Tips & Tricks: Convergence and Mesh Independence Study*. [Online] Available at: http://www.computationalfluiddynamics.com.au/convergence-and-mesh-independent-study/
[Accessed 15 March 2014].

Leverone, F., 2015. *Miss* [Interview] (November 2015).

Lin, J. C., 2002. Review of research on low-profile vortex generators to control boundary-layer separation. *Review of research on low-profile vortex generators to control boundary-layer separation*, pp. 29-31/417-419; 7/395.

Liu, Y., Pekkan, K., Jones, S. C. & Yodanathan, A. P., 2004. The Effects of Different Mesh generation methods on computational fluid dynamic analysis and power loss assessment in total cavopulmanary connection. *Journal of Biomechanical Engineering,* Volume 126, p. 598.

Lombardi, G., 2009. *Use of the CFD for the Aerodynamic Optimization of the Car Shape : Problems and Application.* Munich, EASC, pp. 1-12.

Martin, N. J. & Holzhauser, C. A., 1948. *An experimental investigation at large scale of several configurations of naca submerged air intake,* Mountain View: National Advisory Committee for Aeronautics.

McDonough, J. M., 2007. *Lectures in Computational Fluid Dynamics of Incompressible Flow.* Lexington: University of Kentucky.

Memon, S. A., 2012. *CFD Online.* [Online] Available at: http://www.cfd-online.com/Forums/ansys-meshing/82122-mesh-quality-criteria-icem.html

Moritz, E. F. & Haake, S., 2006. *The Engineering of Sport.* Volume 1 ed. New York: Springer Science + Bussiness Media, LLC.

Mossman, E. A., 1949. *Comparison of two submerged inlets at subsonic and transonic speeds,* Mountain View: National Advisory Committee for Aeronautics.

Nalanagula, S. & Varadharajan, G., 2016. Aerodynamic Drag Reductions Methodology for the Commercial Vehicles using Computational Fluid Dynamics. *SAE International Journal of Commercial Vehicles*, 125(2EJ), p. 8.

NASA, 1945. *NACA central Cranfield.* [Online] Available at: http://naca.central.cranfield.ac.uk/reports/1945/naca-acr-5i20.pdf [Accessed 29 May 2015].

Nieto, F., Zasso, A., Rocchi, D. & Hernandez, S., 2008. *CFD Verification of Aerodynamic Devices Performance for The Messina Straight Bridge,* A Coruna, Spain: University of A Corunaa.

Othmer, C., 2014. Adjoint methods for car aerodynamics. *Journal of Mathematics in Industry,* 4(6), pp. 1-23.

Owen, B., 1991. *Craftsmans Corner.* [Online] Available at: http://wiki.velocityoba.com/images/d/d6/NACA_Article_SA_12-01.pdf [Accessed 29 May 2015].

Patil, C. N., 2012. Aerodynamic Study and drag coefficient optimization of passenger vehicle. *International Journal of Engineering Research & Technology (IJERT),* 1(7), pp. 1-9.

Pignier, N. J., O'Reilly, C. J. & Boij, S., 2015. Aeroacoustic analysis of a NACA Duct. *EuroNoise,* 31 May - 3 June(May - June 2015).

Pointwise, Inc., 2012. *Another Fine Mesh.* [Online] Available at: http://blog.pointwise.com/2012/07/05/accuracy-convergence-and-mesh-quality/ [Accessed 2015 March 12].

Raymer, D. P., 2012. *Aircraft Design: A Conceptual Approach.* 5th Edition ed. Blacksburg: American Institute of Aeronautics and Astronautics, Inc..

Richings, M., 2014. *Mr* [Interview] (June 2014).

Roberts, D., 1998-2012. *Geometric Sequences and Series.* [Online] Available at: http://www.regentsprep.org/Regents/math/algtrig/ATP2/GeoSeq.htm

Salaverry, P. C., 2012. *Method of reducing drag on the outer surface of a vehicle.* s.l. Patent No. US8141936 B2.

Sareen, A., Deters, R. W., Henry, S. P. & Seligx, M. S., 2011. Drag Reduction Using Riblet Film Applied to Airfoils. *Drag Reduction Using Riblet Film Applied to Airfoils,* pp. 1-19.

Sauran, 2013. *Sauran.net.* [Online] Available at: Sauran.net [Accessed 17 March 2014].

Šavli, M., 2012. *Turbulence kinetic energy - TKE.* [Online] Available at: http://mafija.fmf.uni-lj.siseminarfiles2011_2012MaticSavli_2.pdf

Sayma, A., 2009. *Computational Fluid Dynamics.* s.l.:Ventus Publishing APS.

Shapro, A. H., 1969. *Film Notes for Vorticity.* Cambridge: Massachusetts Institute of Technology.

Sinclair, P., 2015. *Mr* [Interview] (November 2015).

Singh, S., 2015. *Mr* [Interview] (November 2015).

Sinha, S. K. & Ravande, S. V., 2006. *Drag Reduction of Natural Laminar Flow Airfoils with an angle of attack.* San Francisco, The American Institute of Aeronautics and Astronautics, pp. 1-17.

Skopinski, J., 2010. *AERO-SERVICE.* Warsaw: Aero-service Jacek Skopinski.

Slater, J. W., 2008. Examining iterative convergence. *NPARC Alliance CFD verification and validation website*, 17 July.

Smith, F. T. & Brown, S. N., 1986. *Boundary layer separation.* London, Springer Verlag, International union of theoretical and applied mechanics.

Sodja, J., 2007. *Turbulence models in CFD.* Ljubljana: University of Ljubljana.

Srivastav, D., 2012. 2012 International Conference on Fluid Dynamics and Thermodynamics Technologies (FDTT 2012). *Flow Control over Airfoils using Different Shaped Dimples*, pp. 1-6.

Tay, C. M., 2011. *Determining the effect of dimples on drag in a turbulent channel flow.* Orlando, American Institute of Aeronautics and Astronautics.

Team, L. C., 2015. © *2016 Computational Fluid Dynamics (CFD) Blog.* [Online] Available at: http://www.computationalfluiddynamics.com.au/tips-tricks-turbulence-part-4-reviewing-how-well-you-have-resolved-the-boundary-layer/
[Accessed 20 December 2015].

Thomson, K. & Schuize, T., 2009. Delivering fuel and emmisions savings for the 777. *Boeing periodical*, March, pp. 5-7.

Vale, C. & Ringrow, H., 2011. *A300/A310 Family optimized air-vent inlet NACA Duct,* Toulouse: Bruno Piquet.

Veale, K., 2015. *Miss* [Interview] (November 2015).

Veldhuis, L. & Vervoort, E., 2009. *Drag Effect of a dented Surface in a Turbulent Flow.* San Antonio, American Institute of Aeronautics and Astronautics.

Versteeg, H. & Malalasekera, W., 1995. *An Introduction to Computational Fluid Dynamics: The Finite Volume Method.* 2nd ed. London: Longman Group Limited.

Viswanath, P. R., 2002. Aircraft viscous drag reduction using riblets. *Progress in Aerospace Sciences,* 38(9), pp. 571-600.

Whitehouse, B., 2012. *NACA Submerged Duct Construction.* [Online] Available at: http://webcache.googleusercontent.com/search?q=cache:j_m09YpiQNsJ:www.cas-cozy.nl/building/images/engineer/naca/NACA%2520Duct%2520Design.doc+&cd=3&hl=en&ct=clnk&gl=za
[Accessed 29 May 2015].

Wong, S. F. & Dol, S. S., 2016. Simulation study on vehicle drag reduction by surface dimples. *International Journal of Mechanical, Industrial, Mechatronic and Manufacturing Engineering,* 10(3), pp. 538-542.

Yang, S., 2013. *Boundary Layer and Separation Control on Wings at Low Reynolds Numbers,* Los Angeles: University of Southern California.

Zumerchik, J., 2008. *Newton on the Tee, A Good Walk Through the Science of Golf.* April 2008 ed. New York: Simon & Shuster Paperbacks.

APPENDIX A

Appendix A1 – Dimple Dimensions

Table A-1: Dimple measurements.

Literature Reviewed	Hexa Solar Car Project (High and low curvature)	Zipp Wheels (low curvature)	Zipp wheels (low curvature)	Garneau Helmet (High curvature)	Garneau Helmet (High curvature)
Dimple, [mm]	2.35	5.60	9.20	5.20	11.37
Length, [mm]	192	653	653	376	376
Dimple Diameter /length: Z, [-]	0.0123	0.0086	0.0141	0.0138	0.0302
% Z	1.23	0.86	1.41	1.38	3.02
Range, [mm]	0,86 - 3				
Mean, [mm]	1,58				
Mode – Low curvature - % Z, [-]	1,34	Low curvature	Flat bottomed		
Mode – High curvatuure - % Z, [-]	1,3 - 3	High curvatuure	Rounded		
Tyre Diameter, [mm]	514				
Dimple Diameter, 2mm dimple spacing, [mm]	Minimum	Maximum	Mean		
Dimple sizing, [mm] – Low curvature	4	7	5.5		
Dimple sizing, [mm] – Hight curvature	7	15	11		

Table A-2: Dimple spacing.

Dimple Spacing	Constants		
Diameter of outer wheel cover, [mm]	404		
Circumference of outer wheel cover, [mm]	1269		
No. of dimples, 2 mm spacing (360 degrees)	169		
Inner surface - dimple diameter, [mm]	11		
Outer surface - dimple diameter, [mm]	5,5		
Outer Cover, 2mm spacing	**Circumference**	**No. Dimples**	**PCD**
Largest Diameter PCD	1275	159	203
One PCD towards axle from above PCD	1228	154	196
One PCD towards axle from above PCD	1172	146	187
One PCD towards axle from above PCD	1125	141	179
One PCD towards axle from above PCD	1078	135	172
One PCD towards axle from above PCD	1030	129	164
One PCD towards axle from above PCD	983	123	157
One PCD towards axle from above PCD	936	117	149
One PCD towards axle from above PCD	889	111	142
One PCD towards axle from above PCD	842	105	134
One PCD towards axle from above PCD	795	99	127
Inner Cover, 2mm spacing	**Circumference**	**No. Dimples**	**PCD**
Largest Diameter PCD	1194	92	190
One PCD towards axle from above PCD	1131	87	180
One PCD towards axle from above PCD	1068	82	170
One PCD towards axle from above PCD	1005	77	160
One PCD towards axle from above PCD	942	72	150
One PCD towards axle from above PCD	880	68	140
One PCD towards axle from above PCD	817	63	130

Appendix A2 – NACA Duct

Table A-3: Optimal duct parameters.

Parameters	Optimal	Range	Notes
Vehicle Speed [m/s]	19.44	70 - 130	
Duct Velocity, [m/s]	13.61	0.5 - 1.5	Duct velocity = 70 % of flow speed
Width/Height of entrance, [mm]	4,0	3 - 5	
Duct Floor Slope, [Degrees]	5,0	5 - 7	Dependent on length available, choose length and check angle is in range

Table A-4: Optimal duct dimensions.

Refer to Figure 2-22 and Table 2-1 for reference when analysing Tables A-4 and A-5.

X/L	Y/(W/2)	x (L=30mm)	Y (W=120mm)	W (W/L optimal set at 4)
0,00	0,50	0,00	35,00	140
0,10	0,50	3,50	34,79	
0,20	0,46	7,00	31,99	
0,30	0,36	10,50	25,34	
0,40	0,31	14,00	21,49	
0,50	0,23	17,50	16,31	
0,60	0,20	21,00	13,65	
0,70	0,16	24,50	10,99	
0,80	0,12	28,00	8,26	
0,90	0,08	31,50	5,60	
1,00	0,04	35,00	2,94	

Table A-5: Optimal duct dimensions continued.

Aerofoil Length, L.E Radius = 2.3876 mm, [mm], (Sta.)	Y-Upper, [mm]	Y-Lower, [mm]	Side-View & Top view Sta. Points	Duct Length, L=11.312, (X/L), [mm]	Side View Height, (y/w), [mm]
0.000	0.197	0.2	0	0.000	2.000
0.125	0.087	0.33	1	1.130	1.990
0.250	0.056	0.38	2	2.260	1.830
0.375	0.056	0.41	3	3.390	1.450
0.500	0.021	0.44	4	4.520	1.230
0.625	0.012	0.46	5	5.660	0.930
0.750	0.006	0.48	6	6.790	0.780
0.875	0.002	*	7	7.920	0.630
1.000	0.000	*	8	9.050	0.470
			9	10.180	0.320
			10	11.312	0.170
Scaled – 10 mm entrance height					
0	1.77	1.77		0,00	18,00
1.25	0.78	2.93		10,18	17,89
2.5	0.5	3.38		20,36	16,45
3.75	0.32	3.71		30,54	13,03
5	0.19	3.96		40,72	11,05
6.25	0.11	4.16		50,90	8,39
7.5	0.05	4.33		61,08	7,02
8.75	0.002	*		71,27	5,65
10	0	*		81,45	4,25
*** - As per Table 2-1.**				91,63	2,88
				101,81	1,51
				113.120	1.700

Appendix A3 – Meshing

Sample Calculations for mesh specifications

Prism layer specifications:

As per equation 2-5 to equation 2-12; the boundary/prism layer characteristics for the Top shell are calculated as follows:

Constants (obtained from CD-Adapco user guide and verified in the textbooks used):

- Speed (Ux3.6): 70 kp/h
- Kinematic Viscosity (υ): 1.56659 x 10^{-5} N.s.
- Reference Length (x): 4.45 m
- Density of air (ρ): 1.18415 kg/m^3

Top shell prism layer specifications:

$$Re = \frac{Ux}{\upsilon} = \frac{\frac{70}{3.6} \times 4.45}{1.56659 \times 10^{-5}} = 1{,}650{,}788$$

Skin Friction Coefficient:

$$C_f = \frac{2 \times 0.036}{Re^{0.2}} = \frac{2 \times 0.036}{1650787.82^{0.2}} = 0.0041$$

Wall shear stress:

$$\tau_w = C_f \times \rho \times \frac{U^2}{2} = 0.00410955 \times 1.18415 \times \frac{\frac{40}{3.6}^2}{2} = 11.93\ Pa$$

u^* (Dimensionless term):

$$u^* = \sqrt{\frac{\tau_w}{\rho}} = \sqrt{\frac{11.9224923}{1.18415}} = 3.17$$

y^+(Dimensionless term):

$$y^+ = \frac{u^* \times y}{\upsilon} \overset{y^+=1}{\Longrightarrow} 1 = \frac{3.17 \times y}{1.57 \times 10^{-5}}$$

First prism layer "mid-cell" height (Assume y+ = 1 as desired):

$$=> y = \frac{\upsilon}{u^*} = 4.94 \times 10^{-6} m$$

First prism layer cell height converted to millimetres = 2y x 1000:

$$2y = 2 \times 4.94 \times 10^{-6} \times 1000 = 0.0049\,mm$$

Boundary layer thickness calculation:

$$\delta = \frac{0.382 \times x}{Re^{\frac{1}{5}}} = \frac{0.382 \times 4.45}{1650787.82^{\frac{1}{5}}} \times 1000 = 76.20\,mm$$

The first prism layer thickness was taken into account by using geometric progression to allow for the stretching factor to be calculated.

$$r = \sqrt[n-1]{\frac{\delta}{2y}} = \sqrt[26-1]{\frac{76.2 \times 10^{-3}}{2 \times (4.9371 \times 10^{-6})}} = 1.44$$

The above calculation shows how the number of prism layers was chosen to satisfy the criteria below:

$$1.3 \leq r \leq 1.5$$

Where r = 1.44

Table A-6: Detailed mesh specifications.

Top shell – Mesh iteration number for each velocity value	1	2	3	4	5
Speed, [kph]	3.00E+01	5.00E+01	7.00E+01	9.00E+01	1.10E+02
Dynamic Viscosity, [Pa-s]	1.86E+00	1.86E+00	1.86E+00	1.86E+00	1.86E+00
Density of air, [kg/m]	1.18E+05	1.18E+05	1.18E+05	1.18E+05	1.18E+05
Kinematic Viscosity, [N.s]	1.57E+00	1.57E+00	1.57E+00	1.57E+00	1.57E+00
Reference Length, [m]	4.45E+00	4.45E+00	4.45E+00	4.45E+00	4.45E+00
Reynolds Number	2.37E+09	3.95E+09	5.52E+09	7.10E+09	8.68E+09
Skin Friction Coefficient	3.82E-03	3.45E-03	3.23E-03	3.07E-03	2.95E-03
Wall Shear, [Pa]	2.04E+09	5.11E+09	9.36E+09	1.47E+09	2.11E+09
u*	1.31E+09	2.08E+09	2.81E+09	3.53E+09	4.22E+09
First layer mid cell height, [m]	1.19E+00	7.54E-01	5.57E-01	4.44E-01	3.71E-01
First layer mid cell height, [mm]	1.19E-02	7.54E-03	5.57E-03	4.44E-03	3.71E-03
First layer cell height, [mm]	2.39E-02	1.51E-02	1.11E-02	8.89E-03	7.42E-03
Canopy – Mesh iteration number for each velocity value	1	2	3	4	5
Speed, [kph]	3.00E+01	5.00E+01	7.00E+01	9.00E+01	1.10E+02
Dynamic Viscosity, [Pa-s]	1.86E+00	1.86E+00	1.86E+00	1.86E+00	1.86E+00
Density of air, [kg/m]	1.18E+05	1.18E+05	1.18E+05	1.18E+05	1.18E+05
Kinematic Viscosity, [N.s]	1.57E+00	1.57E+00	1.57E+00	1.57E+00	1.57E+00
Reference Length, [m]	1.33E+00	1.33E+00	1.33E+00	1.33E+00	1.33E+00
Reynolds Number	7.07E+08	1.18E+09	1.65E+09	2.12E+09	2.59E+09
Skin Friction Coefficient	4.87E-03	4.40E-03	4.11E-03	3.91E-03	3.75E-03
Wall Shear, [Pa]	2.59E+09	6.51E+09	1.19E+09	1.87E+09	2.69E+08
u*	1.48E+09	2.34E+09	3.17E+09	3.98E+09	4.77E+09
First layer mid cell height, [m]	1.06E+00	6.68E-02	4.94E-01	3.94E-01	3.29E-01
First layer mid cell height, [mm]	1.06E-02	6.68E-03	4.94E-03	3.94E-03	3.29E-03
First layer cell height, [mm]	2.12E-02	1.34E-02	9.87E-03	7.88E-03	6.57E-03

Shrouds – Mesh iteration number for each velocity value	**1**	**2**	**3**	**4**	**5**
Speed, [kph]	3.00E+01	5.00E+01	7.00E+01	9.00E+01	1.10E+02
Dynamic Viscosity, [Pa-s]	1.86E+00	1.86E+00	1.86E+00	1.86E+00	1.86E+00
Density of air, [kg/m]	1.18E+05	1.18E+05	1.18E+05	1.18E+05	1.18E+05
Kinematic Viscosity, [N.s]	1.57E+00	1.57E+00	1.57E+00	1.57E+00	1.57E+00
Reference Length, [m]	3.45E+03	3.45E+03	3.45E+03	3.45E+03	3.45E+03
Reynolds Number	1.84E+09	3.06E+09	4.28E+09	5.51E+09	6.73E+09
Skin Friction Coefficient	4.02E-03	3.63E-03	3.40E-03	3.23E-03	3.10E-03
Wall Shear, [Pa]	2.14E+09	5.38E+09	9.85E+09	1.55E+09	2.22E+09
u*	1.35E+09	2.13E+09	2.88E+09	3.62E+09	4.33E+09
First layer mid cell height, [m]	1.16E+00	7.35E-01	5.43E-01	4.33E-01	3.62E-01
First layer mid cell height, [mm]	1.16E-02	7.35E-03	5.43E-03	4.33E-03	3.62E-03
First layer cell height, [mm]	2.30E-02	1.50E-02	1.10E-02	9.00E-03	7.00E-03
Floor – Mesh iteration number for each velocity value	**1**	**2**	3	**4**	**5**
Speed, [kph]	3.00E+01	5.00E+01	7.00E+01	9.00E+01	1.10E+02
Dynamic Viscosity, [Pa-s]	1.86E+00	1.86E+00	1.86E+00	1.86E+00	1.86E+00
Density of air, [kg/m]	1.18E+05	1.18E+05	1.18E+05	1.18E+05	1.18E+05
Kinematic Viscosity, [N.s]	1.57E+00	1.57E+00	1.57E+00	1.57E+00	1.57E+00
Reference Length, [m]	1.35E+01	1.35E+01	1.35E+01	1.35E+01	1.35E+01
Reynolds Number	7.15E+09	1.19E+07	1.67E+07	2.15E+07	2.62E+07
Skin Friction Coefficient	3.06E-03	2.77E-03	2.59E-03	2.46E-03	2.36E-03
Wall Shear, [Pa]	1.63E+09	4.10E+09	7.51E+09	1.18E+09	1.69E+09
u*	1.17E+09	1.86E+09	2.52E+08	3.16E+09	3.78E+09
First layer mid cell height, [m]	1.33E+00	8.42E-01	6.22E-01	4.96E-01	4.14E-01
First layer mid cell height, [mm]	1.33E-02	8.42E-03	6.22E-03	4.96E-03	4.14E-03
First layer cell height, [mm]	2.70E-02	1.70E-02	1.20E-02	1.00E-02	8.00E-03

Table A-7: Boundary & prism layer specifications.

Top shell	**No. Prism Layers - 24**
Speed [KPH]	Boundary Layer Thickness [mm]
30	90,28
65	77,34
75	75,16
85	73,30
110	69,62
Speed [kph]	Stretching Factor [-]
30	1,43
65	1,46
75	1,46
85	1,48
110	1,49
Canopy	No. Prism Layers - 22
Speed [kph]	Boundary Layer Thickness [mm]
30	40,47
65	34,67
75	33,69
85	32,86
110	31,21
Speed [kph]	Stretching Factor [-]
30	1,43
65	1,47
75	1,48
85	1,48
110	1,50
Shroud	No. Prism Layers - 23
Speed [kph]	Boundary Layer Thickness [mm]
30	73,68
65	63,12
75	61,34
85	59,83
110	56,82
Speed [kph]	Stretching Factor [-]
30	1,44
65	1,48
75	1,49
85	1,49
110	1,50

Floor	No. Prism Layers - 26
Speed [kph]	Boundary Layer Thickness [mm]
30	218,71
65	187,37
Speed [kph]	Boundary Layer Thickness [mm]
75	182,09
85	177,17
110	168,66
Speed [kph]	Stretching Factor [-]
30	1,43
65	1,47
75	1,47
85	1,48
110	1,49

Appendix A4 – Wheel rotation physics details

Sample calculations used for the following in table A-8.

Firstly, angular velocity is found:

$$\omega = \frac{30/3.6}{\frac{0{,}514}{2}} = 32\ rad/s$$

Thereafter, angular velocity in revolutions per minute:

$$N = \frac{60 \times 32}{2\pi} = 310\ RPM$$

Table A-8: Wheel rotational speeds.

Speed [kph]	Speed [m/s]	[rad/s]	[rpm]
30	8	32	310
50	14	54	516
65	18	70	671
70	19	76	722
75	21	81	774
80	22	86	826
85	24	92	877
90	25	97	929
110	31	119	1135

Appendix A5 – Batch run simulations

Table A-9: Simulation batches 1 & 2 – Mesh resolution study.

Batch 1 - Canopy	**Mesh Details & Prism Layer Details: L = Layers; S = Stretching**	**Convergence**	**Notes/Conclusion**
Half Car	Overall setting: 10 L; 20 mm; 1.4 S	Converged, Unstable	Use 0 face quality setting; no auto surface repair; half global setting; region specific setting for prisms
Half Car	Overall setting: 10 L; 20 mm; 1.4 S; No automatic surface repair	Converged, Unstable	Use 0 face quality setting, no auto surface repair, half global setting, use specific setting for prisms
Half Car	Overall setting: 10 L; 20 mm; 1.4 S; Using automatic surface repair	Diverged	Use half global prism
Half Car	Overall setting: 10 L; 20 mm; 1.4 S; Wake refinement and boundary changed; No automatic surface repair	Converged, Unstable	Don't use auto surface repair and set minimum surface quality to zero
Half Car	Overall setting: 10 L; 20 mm; 1.4 S; No automatic surface repair; Wake refinement and boundary changed to 600 mm mesh	Converged, Unstable	Finer wake refinement improves results even if outer boundary is coarse
Batch 2 - Canopy Mesh independence	Mesh Details & Prism Layer Details: L = Layers; S = Stretching	Result	Conclusion
Solid model - Canopy, Wheels, Top shell	Overall setting: 10 L; 20 mm; 1.4 S; Batch 1 region specific surface mesh/4	Stable Residuals - Not converged	Simplify geometry
Solid model - Canopy, Wheels, Top shell	Overall setting: 10 L; 20 mm; 1.4 S; Batch 1 region specific surface mesh/2	Stable Residuals - Not converged	Simplify geometry

Table A-10: Simulation batch 3 – Mesh resolution study.

Batch 3 - Geometry & Mesh Simplification

Simulation/Model Number	Simulation Name & Mesh	Comparison simulation	Result	Conclusion
1	Solid model - Canopy, Wheels, Top shell - Batch 1 - Surface mesh upper limit/2	5	Converged to within 10e-4; Residuals low and stable	Use rounded or sharp trailing edge models
2	Model 1 - finer lower limit surface mesh	3	Converged to within 10e-4; Residuals low and stable	Use rounded or sharp trailing edge models
3	Model 2 - squared shroud and top shell trailing edge	2	Converged to within 10e-4; Residuals low and relatively stable	Use rounded or sharp trailing edge models
4	Model 3 - No region specific prism layer mesh	1,2,3,5	Bad Residuals and unstable	Use region specific calculated prism mesh
5	Model 2 - Mesh with coarser surface mesh	1	Converged to within 10e-4; Residuals low and stable	Use rounded and sharp trailing edge models

Table A-11: Simulation batch 4 – Further mesh resolution study.

Batch 4	Mesh Details	Result	Conclusion
Entire car	Batch 3 model-Prism mesh from batch 1-3; fine surface mesh	Converge, Unstable	Use 0 face quality setting; disable automatic surface repair; Use global prism layer from Batch 1 - 3; specific setting for prisms
Entire car	Batch 3 model-Prism mesh from batch 1-3; fine surface mesh	Converge, Unstable	Use 0 face quality setting; disable automatic surface repair; half global setting; specific setting for prisms
Entire car	Batch 3 model-Prism mesh from batch 1-3; fine surface mesh	Diverge	Use global prism layer from Batch 1 - 3
Entire car	Batch 3 model-Prism mesh from batch 1-3 x 2; fine surface mesh	Converge, Unstable	Enable automatic surface repair; set min quality to zero
Entire car	Batch 3 model-Prism mesh from batch 1-3 x 2; fine surface mesh	Converge, Unstable	Finer wake refinement improves results even if outer boundary is coarse

Appendix A6 - Crosswind Details

Table A-12: Crosswind statistics – SASC.

Pretoria

Statistical Quantity		***Speed [m/s]***	
Mean	96,69	Mean	2,44
Standard Error	6,70	Standard Error	0,07
Median	61,06	Median	2,27
Mode	335,90	Mode	1,85
Standard Deviation	91,68	Standard Deviation	0,91
Sample Variance	8404,33	Sample Variance	0,84
Skewness	1,54	Skewness	0,42
Range	358,50	Range	4,36
Minimum	0,00	Minimum	0,49
Maximum	358,50	Maximum	4,86
Sum	18080,73	Sum	457,10
Count	187,00	Count	187,00
Confidence (95.0%)	13,23	Confidence (95.0%)	0,13
Cape Town			
Statistical Quantity		*Speed [m/s]*	
Mean	173,63	Mean	2,22
Standard Error	4,14	Standard Error	0,04
Median	183,10	Median	1,97
Mode	0,00	Mode	1,48
Standard Deviation	111,03	Standard Deviation	1,17
Sample Variance	12327,56	Sample Variance	1,38
Skewness	-0,02	Skewness	1,32
Range	359,90	Range	8,62
Minimum	0,00	Minimum	0,21
Maximum	359,90	Maximum	8,83
Sum	124839,34	Sum	1593,12
Count	719,00	Count	719,00
Confidence (95.0%)	8,13	Confidence (95.0%)	0,09

Bloemfontein

Statistical Quantity		*Speed [m/s]*	
Mean	184,62	Mean	2,95
Standard Error	10,18	Standard Error	0,07
Median	213,90	Median	2,87
Mode	345,40	Mode	2,61
Standard Deviation	129,16	Standard Deviation	0,83
Sample Variance	16682,61	Sample Variance	0,69
Skewness	-0,12	Skewness	0,46
Range	358,76	Range	3,76
Minimum	0,44	Minimum	1,35
Maximum	359,20	Maximum	5,11
Sum	29724,61	Sum	474,30
Count	161,00	Count	161,00
Confidence (95.0%)	20,10	Confidence (95.0%)	0,13
GRAAF RENIET			
Statistical Quantity		*Speed [m/s]*	
Mean	157,10	Mean	3,83
Standard Error	4,97	Standard Error	0,12
Median	144,45	Median	3,68
Mode	0,00	Mode	0,00
Standard Deviation	54,44	Standard Deviation	1,34
Sample Variance	2963,39	Sample Variance	1,79
Skewness	1,21	Skewness	0,35
Range	343,60	Range	8,36
Minimum	0,00	Minimum	0,00
Maximum	343,60	Maximum	8,36
Sum	18851,78	Sum	459,55
Count	120,00	Count	120,00
Confidence (95.0%)	9,84	Confidence (95.0%)	0,24

APPENDIX B

Appendix B1 – Wheel testing

Table B-1: Wheel cover testing results - Part 1.

Iteration 1 - Dimples 1

Coarse Mesh - Element Count	**Description**	**Drag Force, [X direction, [N]]**	**Drag Force [Y direction, [N]]**
5,62E+06	1. Spoked	27,38	-33,80
3,52E+06	2. Smooth	26,25	-34,32
2,11E+06	3. Dimpled	26,30	-34,31
Coarse Mesh/Geometry Simplification - Element Count	**Description**	**Drag Force [X direction, [N]]**	**Drag Force [Y direction, [N]]**
3,09E+06	1. Spoked	27,05	-33,83
1,15E+06	2. Smooth	26,29	-34,34
6,31E+05	3. Dimpled	26,21	-30,48
Finer Mesh - Element Count	**Description**	**Drag Force [X direction, [N]]**	**Drag Force [Y direction, [N]]**
6,48E+05	1. Spoked	27,96	-32,81
4,02E+05	2. Smooth	27,20	-33,58
3,25E+05	3. Dimpled	26,71	-31,26
Finest Mesh - Element Count	**Description**	**Drag Force [X direction, [N]]**	**Drag Force [Y direction, [N]]**
4,84E+06	1. Spoked	27,33	-33,79
2,05E+06	2. Smooth	26,44	-34,36
1,11E+06	3. Dimpled	26,41	-34,00

Iteration 2 - Researched Dimples

Coarse Mesh - Element Count	**Description**	**Drag Force [X direction, [N]]**	**Drag Force [Y direction, [N]]**
3,09E+06	1. Spoked	27,05	-33,83
1,15E+06	2. Smooth	26,29	-34,34
6,31E+05	3. Dimpled	26,21	-30,48
2,66E+06	4. Refined Dimples	26,24	-34,25
Finer Mesh - Element Count	**Description**	**Drag Force [X direction, [N]]**	**Drag Force [Y direction, [N]]**
6,48E+05	1. Spoked	27,96	-32,81
4,02E+05	2. Smooth	27,20	-33,58
3,25E+05	3. Dimpled	26,71	-31,26
1,20E+06	4. Refined Dimples	27,16	-33,48
Finest Mesh - Element Count	**Description**	**Drag Force [X direction, [N]]**	**Drag Force [Y direction, [N]]**
4,49E+06	1. Spoked	27,25	-33,77
1,94E+06	2. Smooth	26,44	-34,35
1,76E+06	3. Dimpled	26,47	-34,32
4,17E+06	4. Refined Dimples	26,40	-34,26

Table B-2: Wheel cover testing results - Part 1.1.

Iteration 1 - Dimples

Coarse Mesh - Element Count	Description	Drag Coefficient, [X-direction]	Result - [X]	Result - [Y]
5,62E+06	Spoked	0,55	[+]-improvement	[-]-improvement
3,52E+06	Smooth	0,53	1,14	0,52
2,11E+06	Dimpled	0,53	1,08	0,51
Coarse Mesh/Geometry Simplification - Element Count	Description	Drag Coefficient, [X-direction]	Result - [x]	Result - [y]
3,09E+06	Spoked	0,54	-	-
1,15E+06	Smooth	0,54	0,76	0,51
6,31E+05	Dimpled	0,53	0,84	-3,35
Finer Mesh - Element Count	Description	Drag Coefficient, [X-direction]	Result - [x]	Result - [y]
6,48E+05	Spoked	0,56	-	-
4,02E+05	Smooth	0,55	0,76	0,77
3,25E+05	Dimpled	0,54	1,25	-1,56
Finest Mesh - Element Count	Description	Drag Coefficient [X direction]	Result - [x]	Result - [y]
4,84E+06	Spoked	0,55	-	-
2,05E+06	Smooth	0,53	0,90	0,57
1,11E+06	Dimpled	0,53	0,92	0,21
Iteration 2 - Refined Dimples				
Coarse Mesh - Element Count	Description	Drag Coefficient [X direction]	Result - [x]	Result - [y]
3,09E+06	Smooth	0,54	-	-
1,15E+06	Dimpled	0,54	0,76	0,51
Coarse Mesh - Element Count	Description	Drag Coefficient [X direction]	Result - [x]	Result - [y]
6,31E+05	Smooth	0,53	0,84	-3,35
2,66E+06	Dimpled	0,53	0,05	0,42

Finer Mesh - Element Count	**Description**	**Drag Coefficient [X direction]**	**Result - [x]**	**Result - [y]**
6,48E+05	Spoked	0,56	-	-
4,02E+05	Smooth	0,55	0,76	0,77
3,25E+05	Dimpled	0,54	1,25	-1,56
1,20E+06	Refined Dimples	0,55	0,04	0,67
Finest Mesh - Element Count	Description	Drag Coefficient [X direction]	Result - [x]	Result - [y]
4,49E+06	Spoked	0,55	-	-
1,94E+06	Smooth	0,53	0,81	0,58
1,76E+06	Dimpled	0,53	0,78	0,55
4,17E+06	Refined Dimples	0,53	0,05	0,49

Table B-3: Wheel cover testing results - Part 1.2.

Iteration 1 - Dimples				
Coarse Mesh - Element Count	Description	Result - [X-coefficient]	Improvement - [%] - Based on x - direction drag coefficient	Improvement - [%] - Based on x - direction drag coefficient
5,62E+06	Spoked	[+]-improvement		
3,52E+06	Smooth	0,02	-0,01	4,23
2,11E+06	Dimpled	0,02	-0,01	4,03
Coarse Mesh/Geometry Simplification - Element Count	Description	Result - [x-coefficient]		
3,09E+06	Spoked	-		
1,15E+06	Smooth	0,00	-0,01	0,00
6,31E+05	Dimpled	0,02	0,04	3,09
Finer Mesh - Element Count	Description	Result - [x-coefficient]		
6,48E+05	Spoked	-		
4,02E+05	Smooth	0,02	-0,01	2,70
3,25E+05	Dimpled	0,03	0,02	4,48
Finest Mesh - Element Count	Description	Result - [x-coefficient]		
4,84E+06	Spoked	-		
2,05E+06	Smooth	0,02	-0,01	3,28
1,11E+06	Dimpled	0,02	0,00	3,37
Finest Mesh - Element Count	Description	Result - [x-coefficient]		
4,84E+06	Spoked	-		
2,05E+06	Smooth	0,02	-0,01	3,28
1,11E+06	Dimpled	0,02	0,00	3,37
Iteration 2 - Refined Dimples				
Coarse Mesh - Element Count	Description	Result - [x-coefficient]		
3,09E+06	Spoked	-		
1,15E+06	Smooth	0,00	-0,01	0,00
6,31E+05	Dimpled	0,02	0,04	3,09
2,66E+06	Refined Dimples	0,02	0,00	2,99

Finer Mesh - Element Count	**Description**	**Result - [x-coefficient]**		
6,48E+05	Spoked	-		
4,02E+05	Smooth	0,02	-0,01	2,70
3,25E+05	Dimpled	0,03	0,02	4,48
1,20E+06	Refined Dimples	0,02	-0,01	2,86
Finest Mesh - Element Count	Description	Result - [x-coefficient]		
4,49E+06	Spoked	-		
1,94E+06	Smooth	0,02	-0,01	2,96
1,76E+06	Dimpled	0,02	-0,01	2,87
4,17E+06	Refined Dimples	0,02	-0,01	3,13

Table B-4: Wheel cover testing results - Part 1.3.

Iteration 1 - Dimples 1

Coarse Mesh - Element Count	Description	Conclusion
5,62E+06	Spoked	Geometry simplification needed
3,52E+06	Smooth	Smooth and dimpled covers allow for reduction in forward drag but increase upward drag
2,11E+06	Dimpled	Aerodynamic drag improvement vs weight added rolling resistance must be verified for gross improvement
Coarse Mesh/Geometry Simplification - Element Count	Description	Conclusion
3,09E+06	Spoked	Simplification allowed for more accurate and stable results
1,15E+06	Smooth	Smooth and dimpled covers allow for reduction in forward drag but increase upward drag
6,31E+05	Dimpled	Aerodynamic drag improvement vs weight added rolling must be verified for gross improvement
Finer Mesh - Element Count	Description	Conclusion
6,48E+05	Spoked	Smooth and dimpled covers allow for reduction in forward drag but increase upward drag
4,02E+05	Smooth	Aerodynamic drag improvement vs weight added rolling resistance must be verified for gross improvement
3,25E+05	Dimpled	Mesh Independence needed
Finest Mesh - Element Count	Description	Conclusion
4,84E+06	Smooth	Smooth and dimpled covers allow for reduction in forward drag but increase upward drag
2,05E+06	Dimpled	Need to check if aerodynamic drag improvement vs weight added rolling resistance
Finest Mesh - Element Count	Description	Conclusion
1,11E+06	Spoked	Mesh Independence needed
4,84E+06	Smooth	Smooth and dimpled covers allow for reduction in forward drag but increase upward drag
2,05E+06	Dimpled	Need to check if aerodynamic drag improvement vs weight added rolling resistance
1,11E+06	Refined Dimples	Mesh Independence needed

Iteration 2 - Refined Dimples		
Coarse Mesh - Element Count	Description	Conclusion
3,09E+06	Spoked	Dimples don’t substantially improve aerodynamics over smooth covers
1,15E+06	Smooth	Mesh Independence reached for within 1 percentile criteria
6,31E+05	Dimpled	Upward drag increased by negligible value
2,66E+06	Refined Dimples	
Finer Mesh - Element Count	Description	Conclusion
6,48E+05	Spoked	Dimples don’t substantially improve aerodynamics over smooth covers
4,02E+05	Smooth	Mesh Independence reached for within 1 percentile criteria
3,25E+05	Dimpled	Upward drag increased by negligible value
1,20E+06	Refined Dimples	
Finest Mesh - Element Count	Description	Conclusion
4,49E+06	Spoked	Dimples don’t substantially improve aerodynamics over smooth covers
1,94E+06	Smooth	Mesh Independence reached for within 1 percentile criteria
1,76E+06	Dimpled	Upward drag increased by negligible value
4,17E+06	Refined Dimples	

Appendix B2 – Canopy testing

Table B-5: Canopy testing results - Part 1: No vortex generators.

Coarse Mesh – Element Count - 70kph	Wheel Rotation	Force [X - direction, [N]]	Force [Y - direction, [N]]	Force Coefficient [X -direction]
5,87E+06	No	38,30	3,61	0,16179
5,87E+06	Yes	38,27	3,61	0,16168
Force on Canopy alone	No	3,14	32,86	-
Canopy Effects?	No	3,14	32,81	-

Table B-6: Canopy testing results - Part 1.1.

Coarse Mesh – Element Count – 70kph	Result - [X]	Result - [Y]	Result - [X-coefficient]	Conclusion
5,87E+06	0,00	0,00	0,0000	
5,87E+06	0,03	0,00	-0,0001	Rotating wheels affects aerodynamics
Canopy Effects?				Effects on canopy are negligible

Table B-7: Canopy testing results - Part 2.

Full Car Model

Finest Mesh Testing at different speeds	Vortex Generators	Force [X - direction, 20kph cross [N]]	Result - [x]	Conclusion
65kmph straight	No	29,03		
65kmph straight	Yes - Further Forward	28,94	0,09	
Finest Mesh Testing at different speeds	**Vortex Generators**	**Force [X - direction, 20kph crosswind [N]]**	**Result - [x]**	**Conclusion**
75kph straight	No	38,29		
75kph straight	Yes - Further back	46,96	-8,67	Don't use vortex generators further back
75kph Crosswind	No	37,82		
75kph straight	Yes - Further Forward	38,29	0,00	Potential for vortex generators further forward
75kph Crosswind	Yes - Further Forward	36,88	0,94	Potential for vortex generators further forward

Table B-8: Canopy testing results - Part 3.

Canopy and top shell only

Finest Mesh Testing at different speeds	**Vortex Generators**	**Force [X - direction, 10kph cross [N]]**	**Force [X - direction, 20kph cross [N]]**
65kmph Crosswind	No	16,6	17,3
65kmph Crosswind	Yes - Further Forward	16,5	16,7
Finest Mesh Testing at different speeds	**Vortex Generators**	**Force [X - direction, 10kph crosswind, [N]]**	**Force [X - direction, 20kph crosswind, [N]]**
75kph Crosswind	No	20,96	21,80
75kph Crosswind	Yes - Further Forward	21,74	21,67
Finest Mesh Testing at different speeds	**Vortex Generators**	**Force [X - direction, 10kph crosswind, [N]]**	**Force [X - direction, 20kph crosswind, [N]]**
85kph Crosswind	No	27,2	27,32
85kph Crosswind	Yes - Further Forward	26,8	27,03

Table B-9: Canopy testing results - Part 3.1.

Canopy and top shell only

Finest Mesh Testing at different speeds	**Result - [X] - Weak crosswind**	**Result - [X] - Strong crosswind**	**Conclusion**
65kmph Crosswind	-	-	
65kmph Crosswind	0,10	0.56	Weak crosswind - more efficient
			Strong crosswind - More Efficient
75kph Crosswind	-	-	Weak crosswind - less efficient
75kph Crosswind	-0,78	0,13	Strong crosswind - more efficient
85kph Crosswind	-	-	Weak crosswind - more efficient
85kph Crosswind	0,44	0,29	Strong crosswind - more efficient

Table B-10: Canopy testing results - Part 4.

Hollow car model - Medium density mesh - 70kph	Force [X direction, [N]]	Force Coefficient [X direction]	Result - [X]	Result - [X-coefficient]	Result
1,65E+07	30,74	0,14720			
1,65E+07 – Canopy Hole Testing	30,86	0,14770	-0,12	0,0005	Hole may increases drag

APPENDIX C

Appendix C1 - Wheel covers

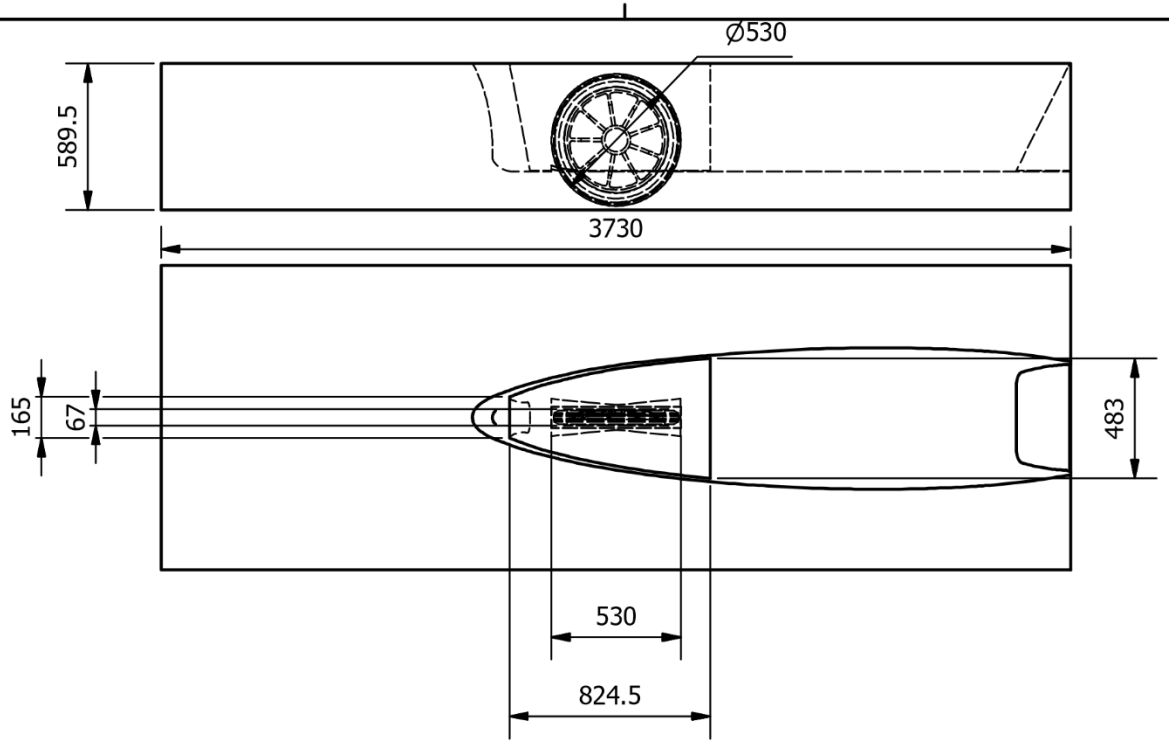

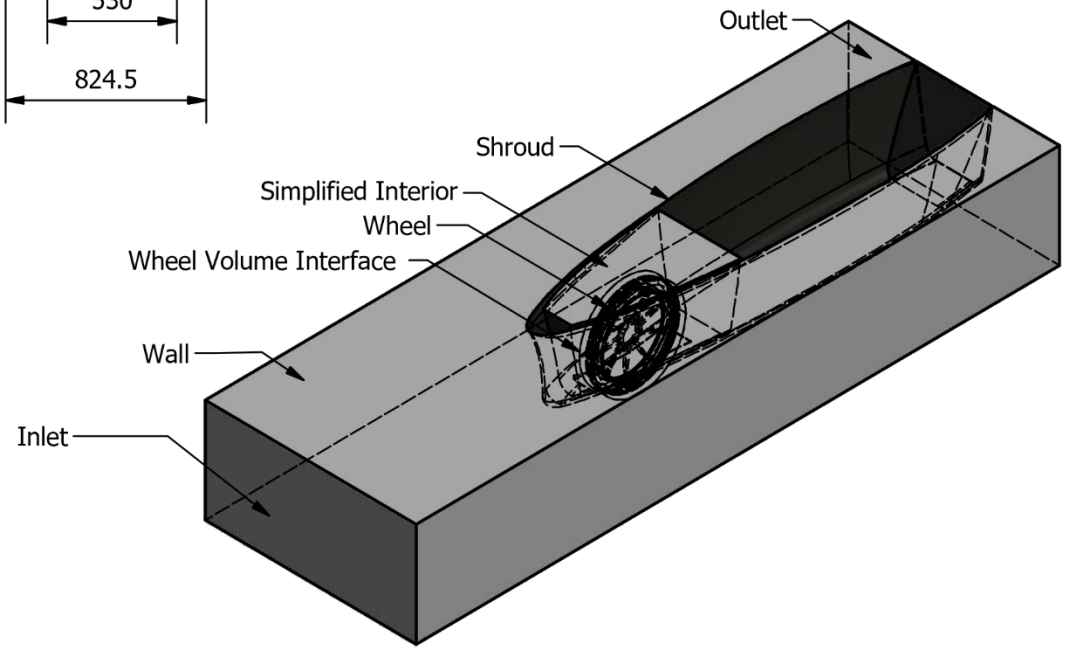

145

UNLESS OTHERWISE STATED GENERAL TOLERANCES: ±0.05 mm
ANGLES: ±0.1 °

SCHOOL OF ENGINEERING MECHANICAL ENGINEERING	MAT.:		No. REQ.:	SCALE: 1:30 UNITS: mm	PROJECT: Solar Car
		DATE	CHECKED	STUDENT NAME: C. Lawrence	NO.: 1
	PROJECT SUPERVISOR			STUDENT No.: 210528785	TITLE: Wheel Cover fluid Domain
	WORKSHOP TECHNICIAN			E-MAIL: chrisjonlawrence@gmail.com	
	TECHNICAL OFFICER			TEL. NO.: 0813228346	

A-A (1: 4)

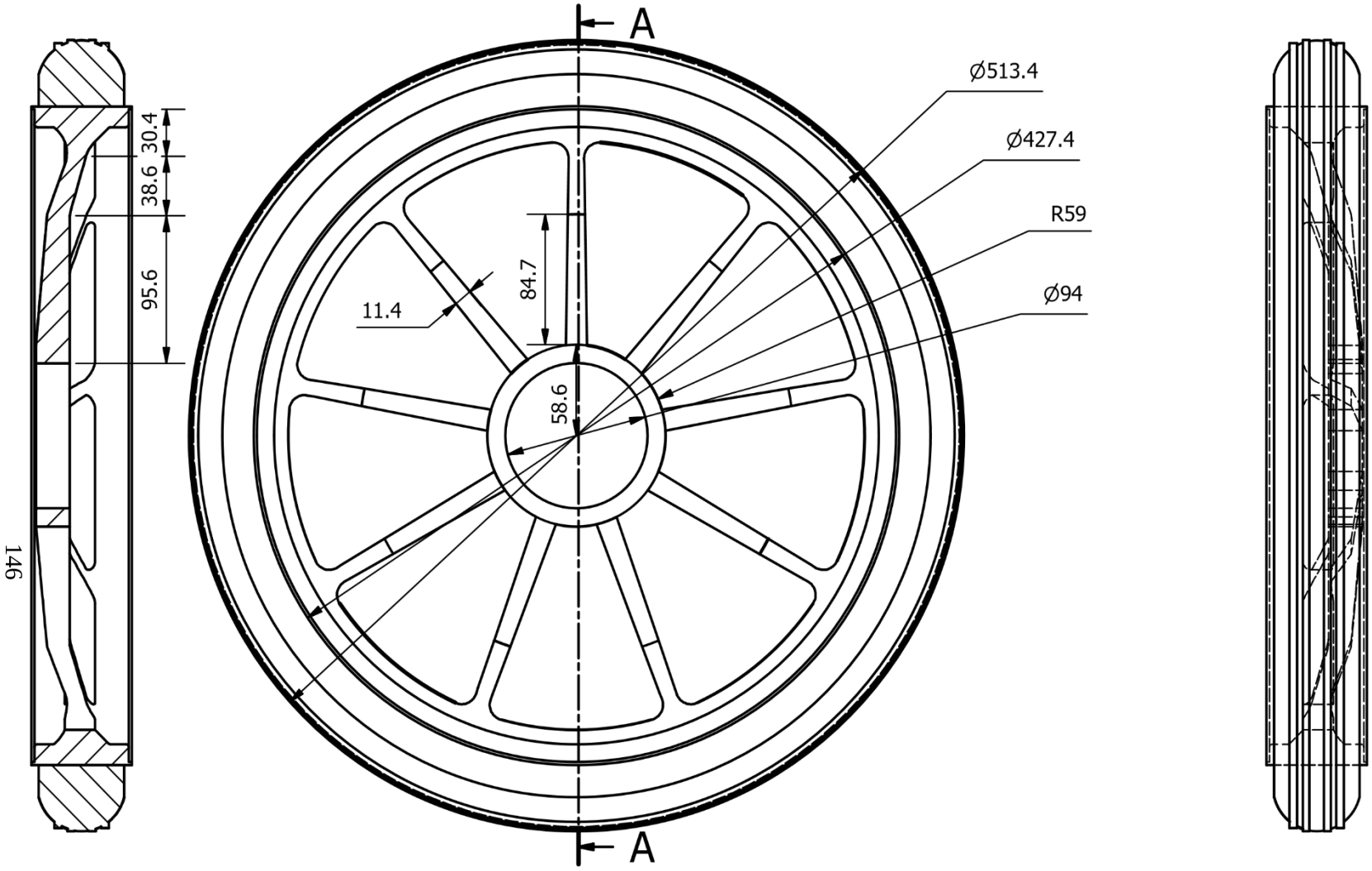

UNLESS OTHERWISE STATED GENERAL TOLERANCES: ±0.05 mm
ANGLES: ±0.1 °

UNIVERSITY OF KWAZULU-NATAL SCHOOL OF ENGINEERING MECHANICAL ENGINEERING	MAT.: Aluminium and rubber		No. REQ.:	SCALE: 1:4	UNITS: mm
		DATE	CHECKED	STUDENT NAME: C. Lawrence	
	PROJECT SUPERVISOR			STUDENT No.: 210518785	
	WORKSHOP TECHNICIAN			E-MAIL: chrisjonlawrence@gmail.com	
	TECHNICAL OFFICER			TEL. NO.: 0813228346	

PROJECT: Solar Car

NO.: 2

TITLE: Mitsuba rim and tyre simplified

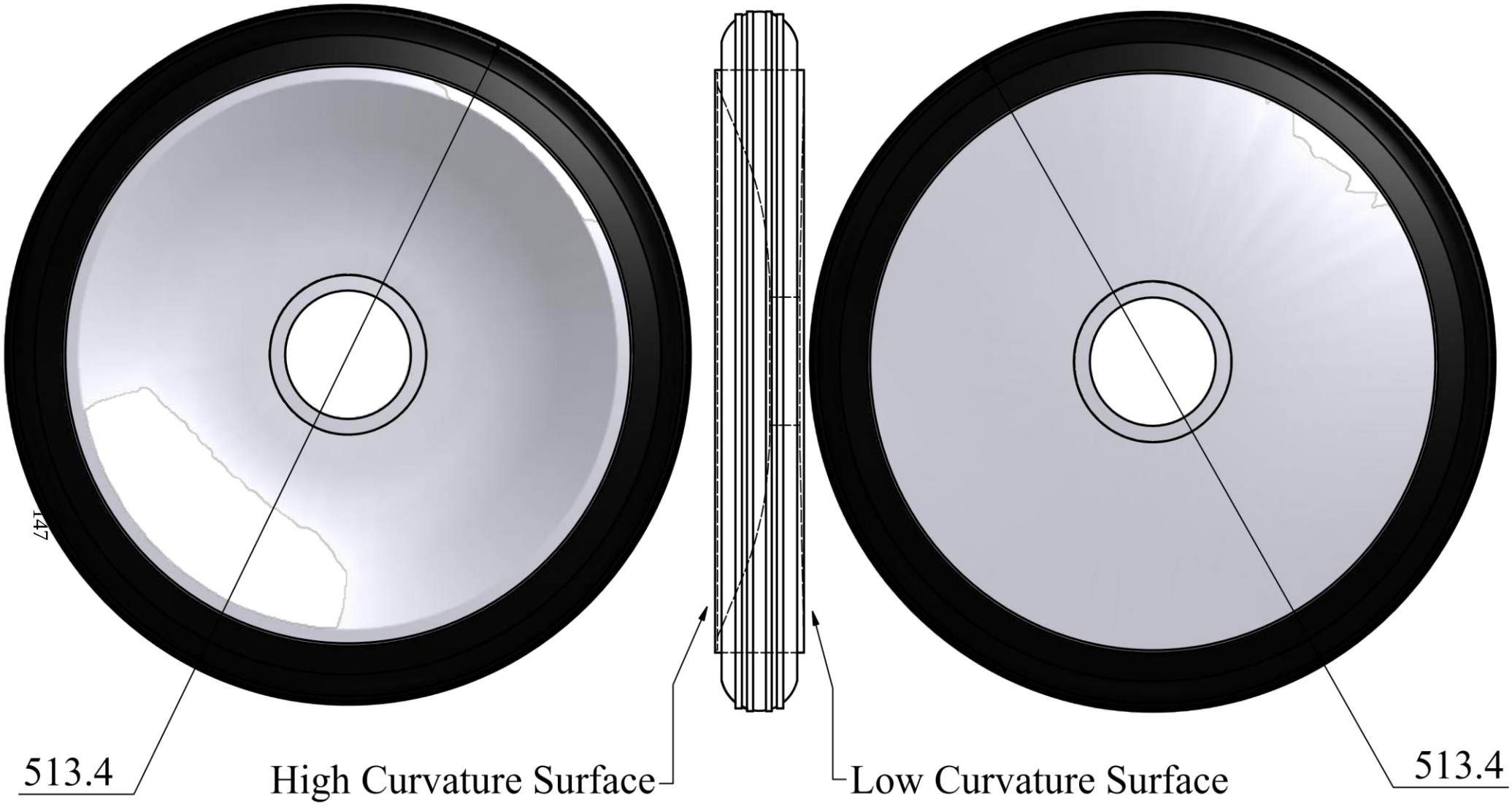

UNLESS OTHERWISE STATED GENERAL TOLERANCES: ±0.05 mm
ANGLES: ±0.1 °

UNIVERSITY OF KWAZULU-NATAL SCHOOL OF ENGINEERING MECHANICAL ENGINEERING	MAT.: Acrylic or Carbon Fibre		No. REQ.:	SCALE: 0.25 :1 UNITS: mm	PROJECT: Solar Car
		DATE	CHECKED	STUDENT NAME: C. Lawrence	NO.: 3
	PROJECT SUPERVISOR			STUDENT No.: 210528785	TITLE: Wheel Cover - Smooth
	WORKSHOP TECHNICIAN			E-MAIL: chrisjonlawrence@gmail.com	
	TECHNICAL OFFICER			TEL. NO.: 0813228346	

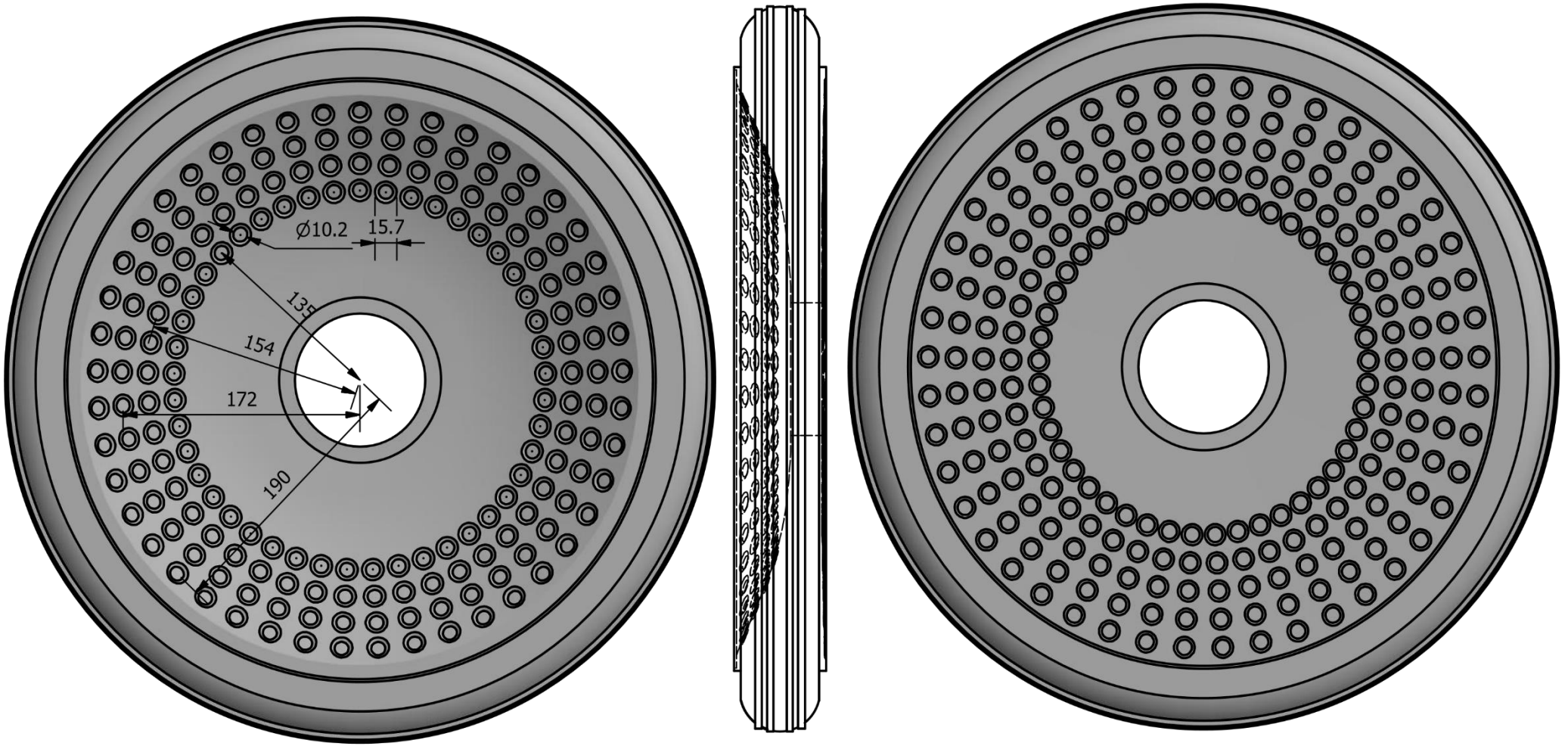

UNLESS OTHERWISE STATED GENERAL TOLERANCES: ±0.05 mm
ANGLES: ±0.1 °

UNIVERSITY OF KWAZULU-NATAL

SCHOOL OF ENGINEERING

MECHANICAL ENGINEERING

MAT.: Acrylic or Carbon Fibre		No. REQ.:	SCALE: 1:4	UNITS: mm
	DATE	CHECKED	STUDENT NAME: C. Lawrence	
PROJECT SUPERVISOR			STUDENT No.: 210518785	
WORKSHOP TECHNICIAN			E-MAIL: chrisjonlawrence@gmail.com	
TECHNICAL OFFICER			TEL. NO.: 0813228346	

PROJECT: Solar Car

NO.: 4

TITLE: Wheel Cover - Coarse Dimples

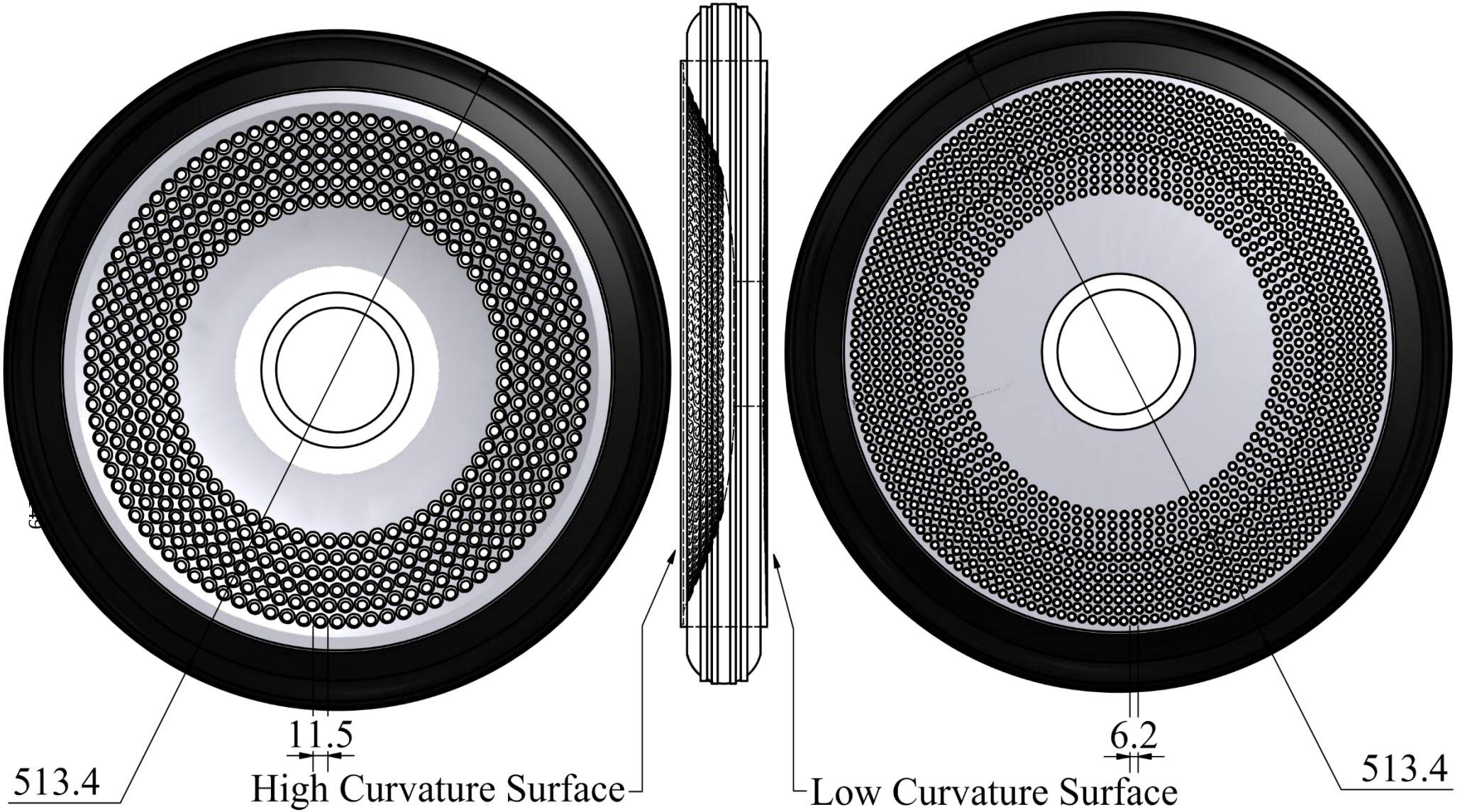

UNLESS OTHERWISE STATED GENERAL TOLERANCES: ±0.05 mm
ANGLES: ±0.1 °

UNIVERSITY OF KWAZULU-NATAL

SCHOOL OF ENGINEERING

MECHANICAL ENGINEERING

MAT.: Acrylic or Carbon Fibre		No. REQ.:	SCALE: 1:4	UNITS: mm
	DATE	CHECKED	STUDENT NAME: C. Lawrecne	
PROJECT SUPERVISOR			STUDENT No.:	
WORKSHOP TECHNICIAN			E-MAIL: chrisjonlawrence@gmail.com	
TECHNICAL OFFICER			TEL. NO.: 0813228346	

PROJECT: Solar Car

NO.: 5

TITLE: Wheel Covers

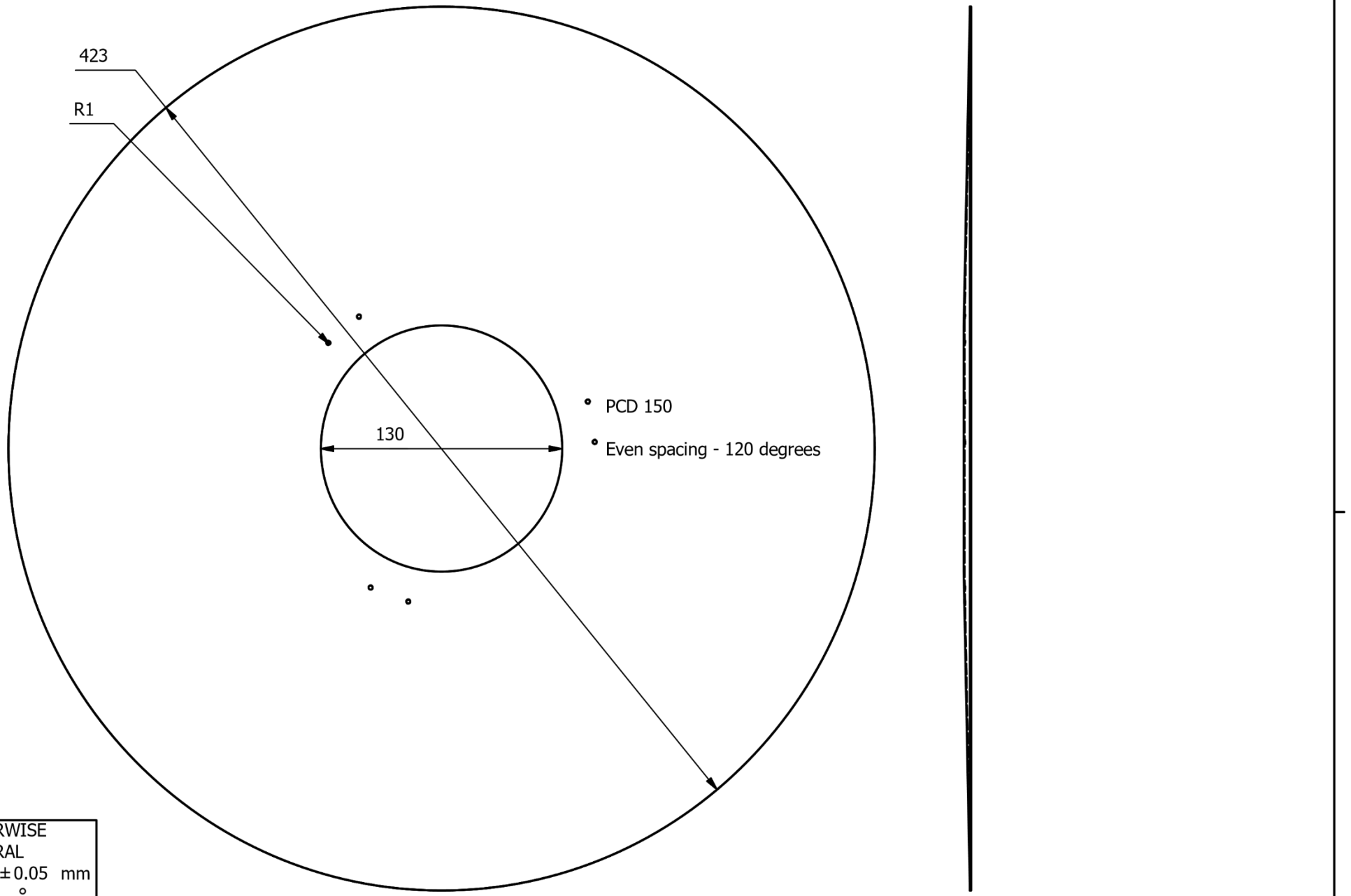

UNLESS OTHERWISE STATED GENERAL TOLERANCES: ±0.05 mm
ANGLES: ±0.1 °

UNIVERSITY OF KWAZULU-NATAL

SCHOOL OF ENGINEERING

MECHANICAL ENGINEERING

MAT.: Acrylic or Carbon Fibre		No. REQ.: 1	SCALE: 1:3	UNITS: mm
	DATE	CHECKED	STUDENT NAME: C. Lawrence	
PROJECT SUPERVISOR			STUDENT No.: 210528785	
WORKSHOP TECHNICIAN			E-MAIL: chrisjonlawrence@gmail.com	
TECHNICAL OFFICER			TEL. NO.: 0813228346	

PROJECT: Solar Car

NO.: 6

TITLE: Front Wheel Cover Outer

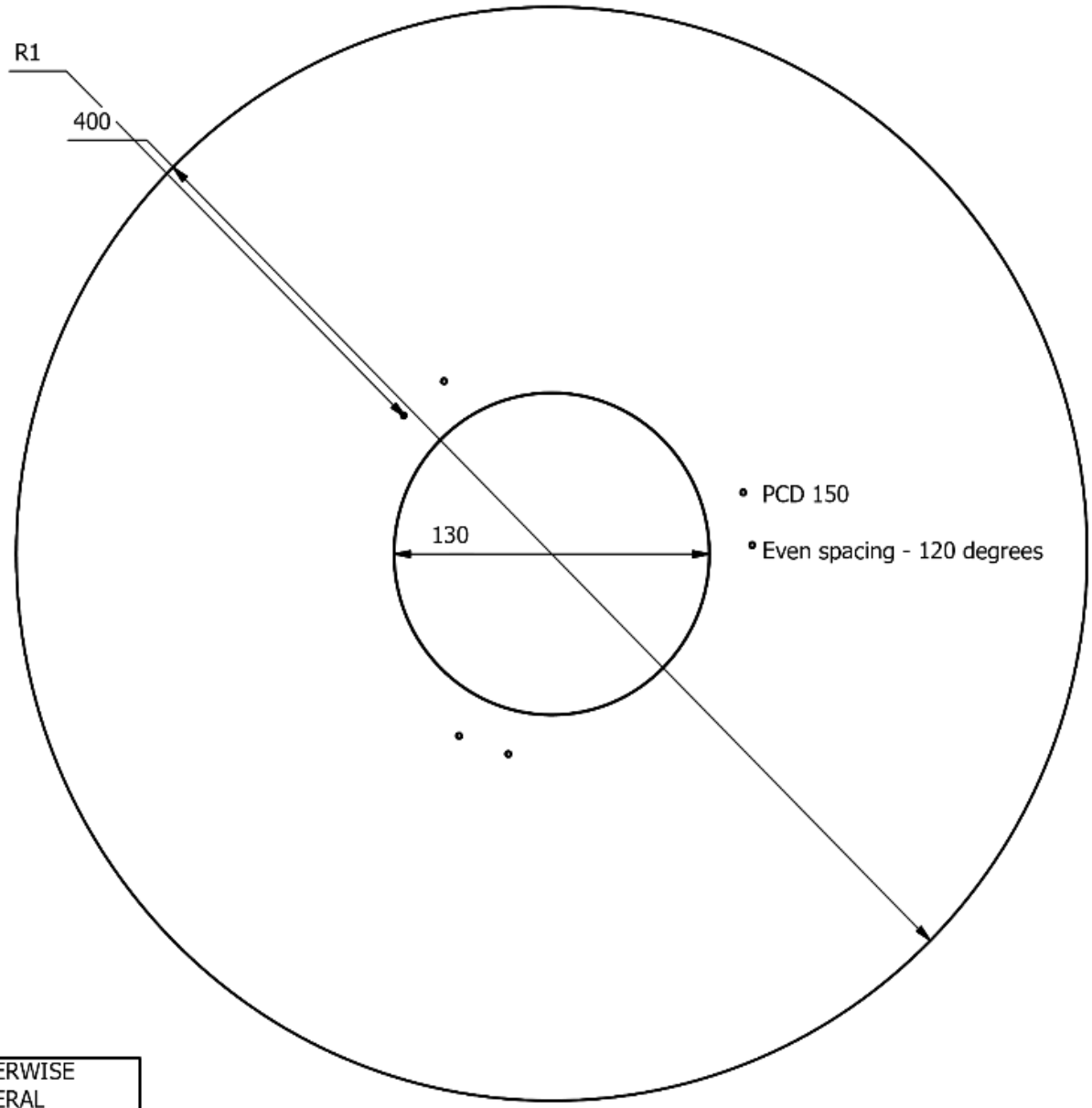

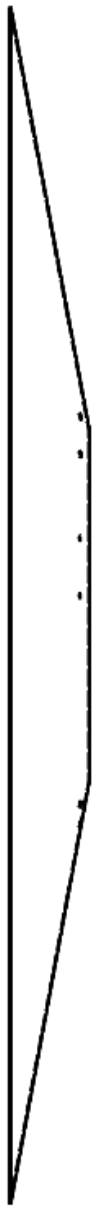

151

UNLESS OTHERWISE STATED GENERAL TOLERANCES: ±0.05 mm
ANGLES: ±0.1 °

UNIVERSITY OF KWAZULU-NATAL

SCHOOL OF ENGINEERING

MECHANICAL ENGINEERING

MAT.: Acrylic or Carbon Fibre		No. REQ.: 1	SCALE: 1:3	UNITS: mm	PROJECT: Solar Car
	DATE	CHECKED	STUDENT NAME: C. Lawrence		NO.: 7
PROJECT SUPERVISOR			STUDENT No.: 210528785		TITLE: Front Wheel Cover - Inner
WORKSHOP TECHNICIAN			E-MAIL: chrisjonlawrence@gmail.com		
TECHNICAL OFFICER			TEL. NO.: 0813228346		

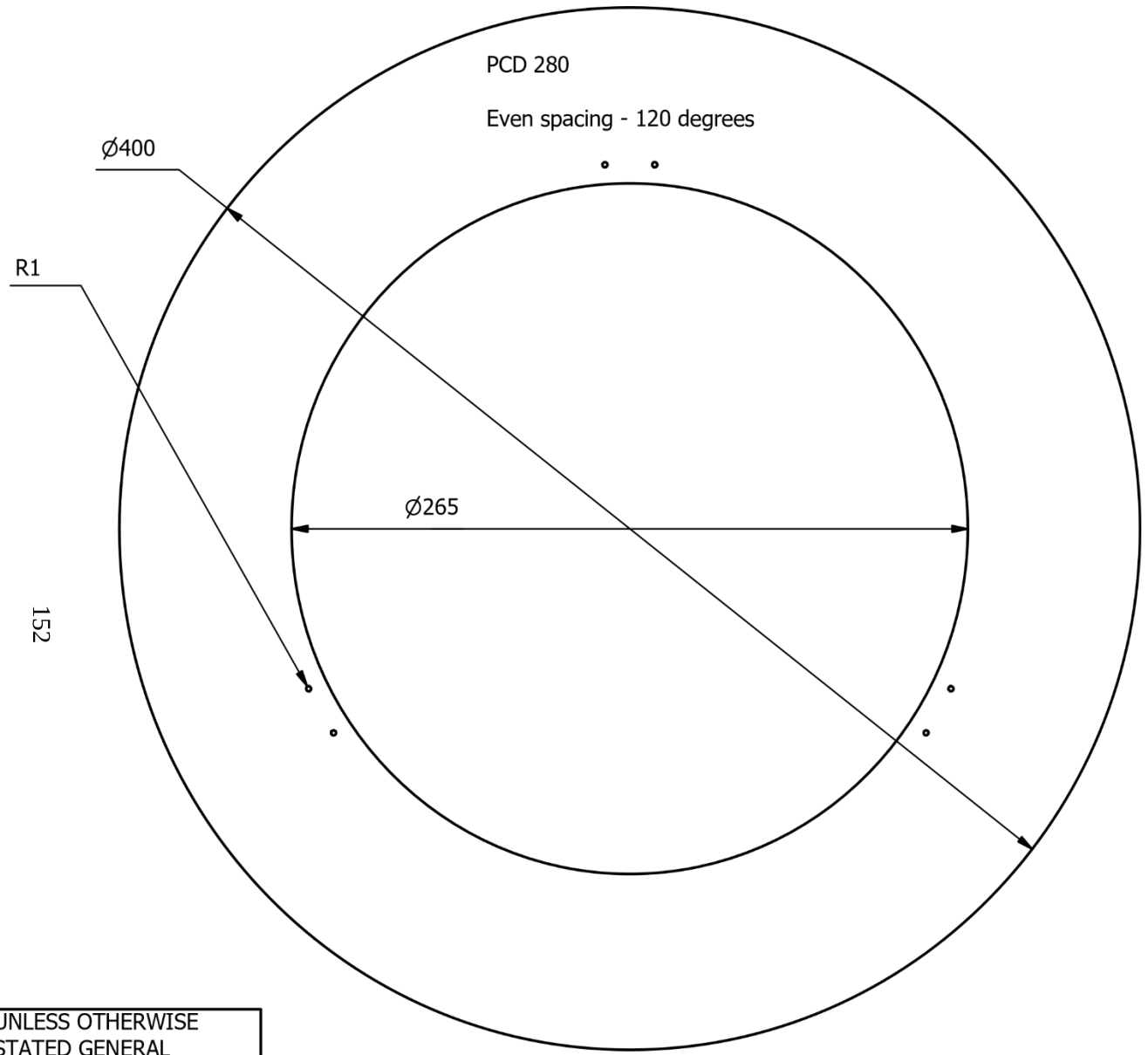

UNLESS OTHERWISE STATED GENERAL TOLERANCES: ±0.05 mm
ANGLES: ±0.1 °

UNIVERSITY OF KWAZULU-NATAL

SCHOOL OF ENGINEERING

MECHANICAL ENGINEERING

MAT.: Acrylic or Carbon Fibre		No. REQ.: 1	SCALE: 1:3	UNITS: mm
	DATE	CHECKED	STUDENT NAME: C. Lawrence	
PROJECT SUPERVISOR			STUDENT No.: 210528785	
WORKSHOP TECHNICIAN			E-MAIL: chrisjonlawrence@gmail.com	
TECHNICAL OFFICER			TEL. NO.: 0813228346	

PROJECT: Solar Car

NO.: 8

TITLE: Front Wheel Cover - Inner

Appendix C2 - Vortex generators

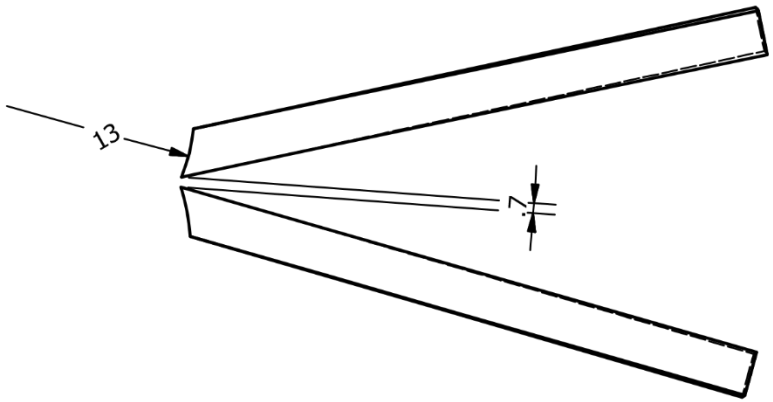

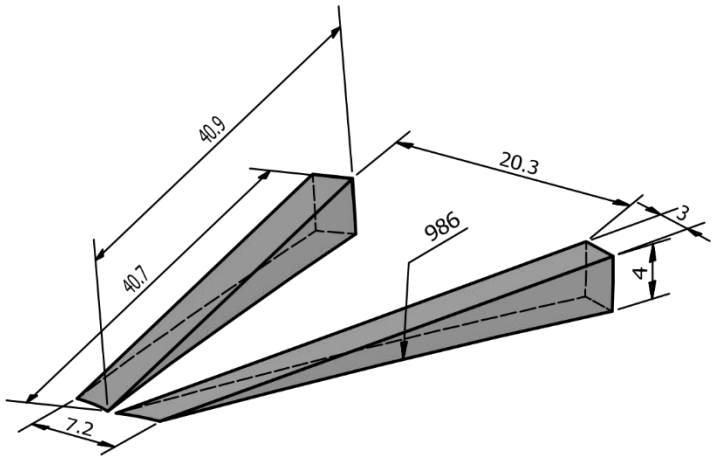

154

UNLESS OTHERWISE STATED GENERAL TOLERANCES: ±0.05 mm
ANGLES: ±0.1 °

UNIVERSITY OF KWAZULU-NATAL SCHOOL OF ENGINEERING MECHANICAL ENGINEERING	MAT.: ABS Plastic - 3D Printed		No. REQ.:	SCALE: 2 :1 UNITS: mm	PROJECT: Solar Car
		DATE	CHECKED	STUDENT NAME: C. Lawrence	
	PROJECT SUPERVISOR			STUDENT No.: 210518785	
	WORKSHOP TECHNICIAN			E-MAIL: chrisjonlawrence@gmail.com	TITLE: Vortex generator
	TECHNICAL OFFICER			TEL. NO.: 0813228346	

NO.: 9

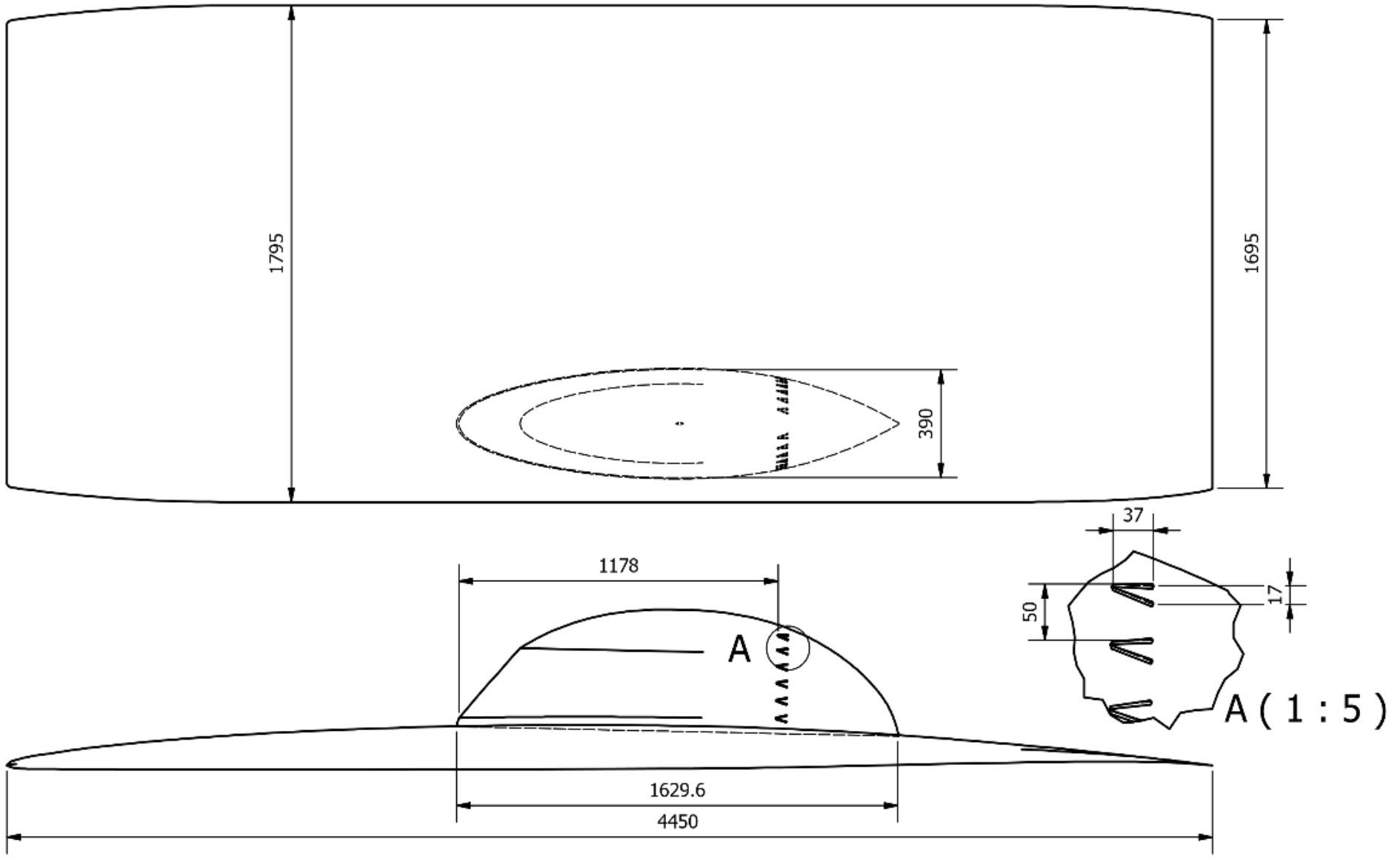

UNLESS OTHERWISE STATED GENERAL TOLERANCES: ±0.05 mm
ANGLES: ±0.1 °

UNIVERSITY OF KWAZULU-NATAL

SCHOOL OF ENGINEERING

MECHANICAL ENGINEERING

MAT.: ABS Plastic - 3-D Printed		No. REQ.:	SCALE: 1:20	UNITS: mm
	DATE	CHECKED	STUDENT NAME: C. Lawrence	
PROJECT SUPERVISOR			STUDENT No.: 210518785	
WORKSHOP TECHNICIAN			E-MAIL: chrisjonlawrence@gmail.com	
TECHNICAL OFFICER			TEL. NO.: 0813228346	

PROJECT: Solar Car

NO.: 10

TITLE: Vortex Generator - Concept Two

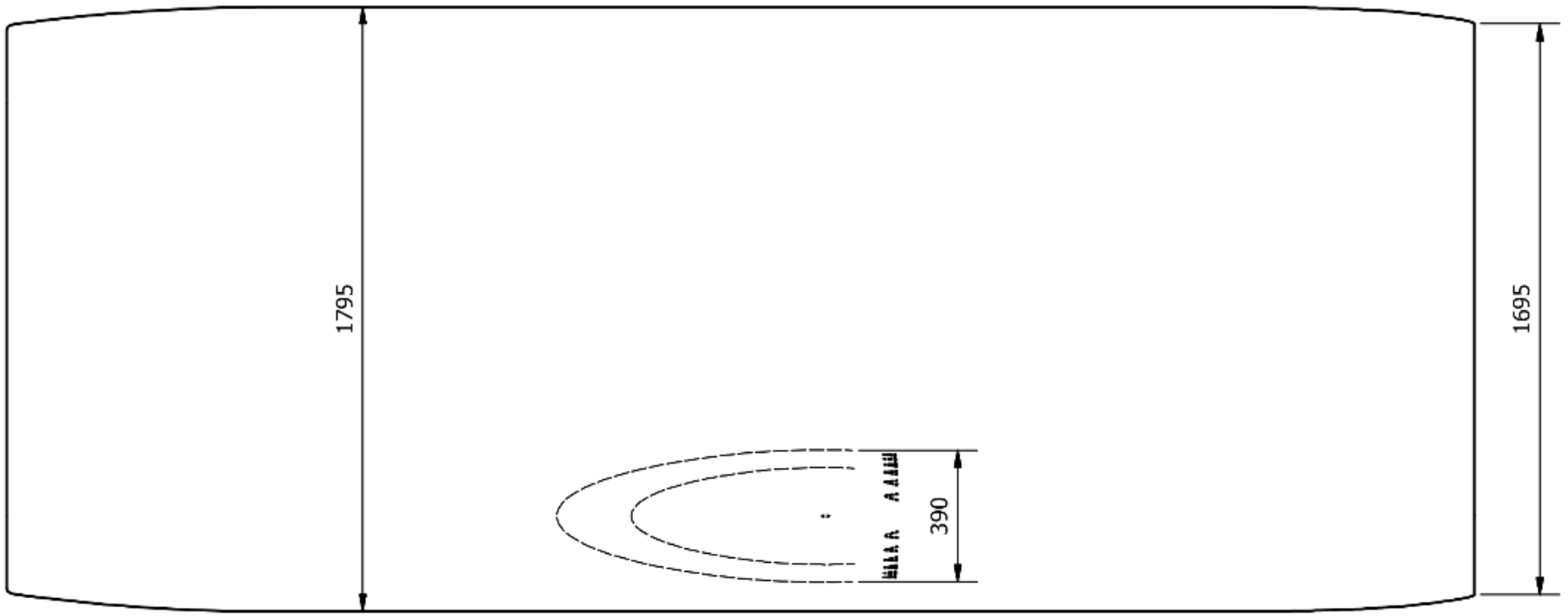

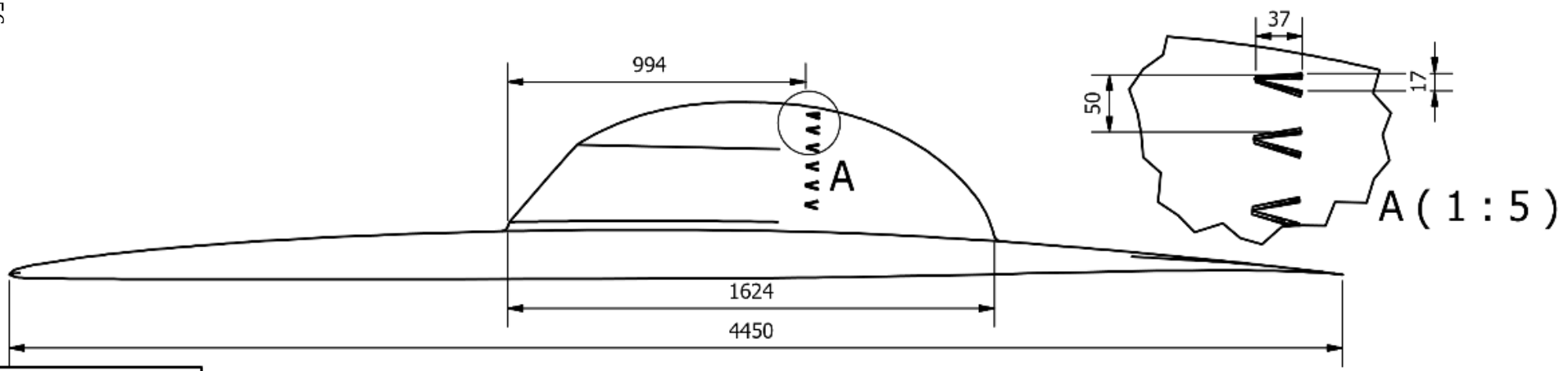

UNLESS OTHERWISE STATED GENERAL TOLERANCES: ±0.05 mm
ANGLES: ±0.1 °

UNIVERSITY OF KWAZULU-NATAL

SCHOOL OF ENGINEERING

MECHANICAL ENGINEERING

MAT.: ABS Plastic - 3-D Printed		No. REQ.:	SCALE: 1:20	UNITS: mm
	DATE	CHECKED	STUDENT NAME: C. Lawrence	
PROJECT SUPERVISOR			STUDENT No.: 210528785	
WORKSHOP TECHNICIAN			E-MAIL: chrisjonlawrence@gmail.com	
TECHNICAL OFFICER			TEL. NO.: 0813228346	

PROJECT: Solar Car

NO.: 11

TITLE: Vortex Generator - Concept Three

Appendix C3 – NACA Duct

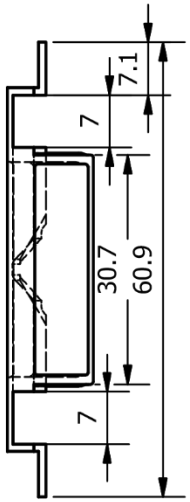

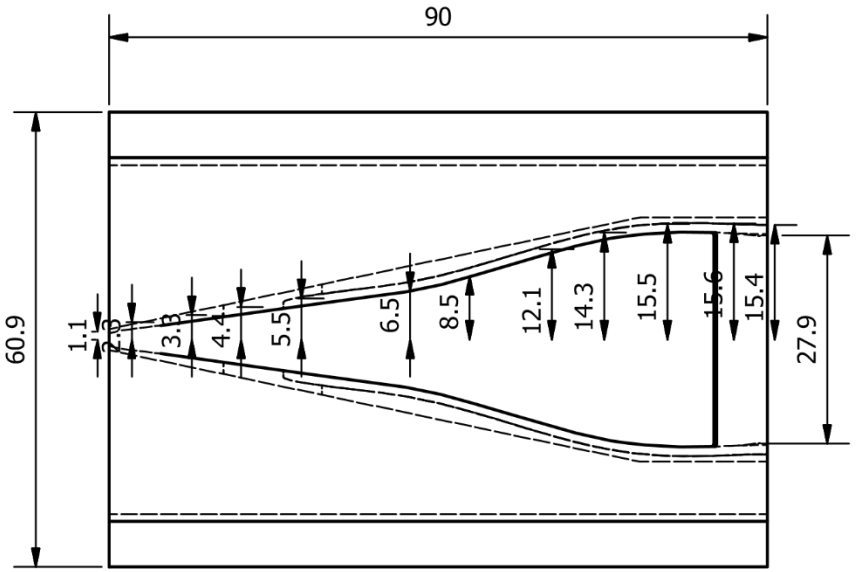

158

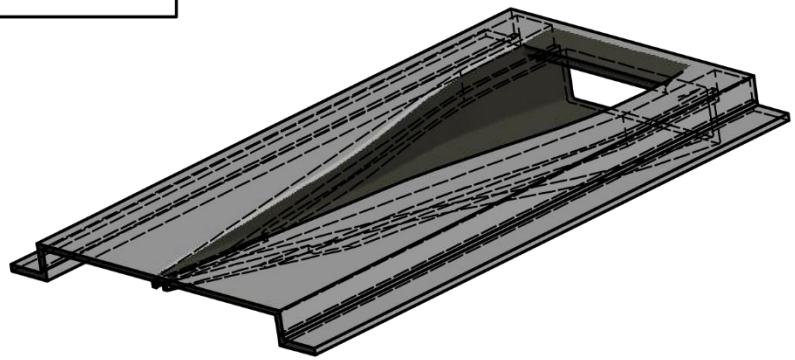

UNLESS OTHERWISE STATED GENERAL TOLERANCES: ±0.05 mm
ANGLES: ±0.1 °

SCHOOL OF ENGINEERING MECHANICAL ENGINEERING	MAT.: ABS Plastic - 3-D printed		No. REQ.:	SCALE: 1:1	UNITS: mm
		DATE	CHECKED	STUDENT NAME: C. Lawrence	
	PROJECT SUPERVISOR			STUDENT No.: 210518785	
	WORKSHOP TECHNICIAN			E-MAIL: chrisjonlawrence@gmail.com	
	TECHNICAL OFFICER			TEL. NO.: 0813228346	

PROJECT: Solar Car

NO.: 12

TITLE: NACA Duct